12-2-2020

Impacts of Irrigated Agriculture on the Near Surface and Planetary Boundary Layer Atmosphere: Results from the Great Plains Irrigation Experiment (GRAINEX)

Emilee Lachenmeier
University of Nebraska-Lincoln, emilee.lachenmeier@huskers.unl.edu

IMPACTS OF IRRIGATED AGRICULTURE ON THE NEAR SURFACE AND PLANETARY BOUNDARY LAYER ATMOSPHERE: RESULTS FROM THE GREAT PLAINS IRRIGATION EXPERIMENT (GRAINEX)

by

Emilee J. Lachenmeier

A THESIS

Presented to the Faculty of

The Graduate College at the University of Nebraska

In Partial Fulfillment of Requirements

For the Degree of Master of Science

Major: Natural Resource Sciences

Under the Supervision of Professor Rezaul Mahmood

Lincoln, Nebraska

November, 2020

IMPACTS OF IRRIGATED AGRICULTURE ON THE NEAR SURFACE AND PLANETARY BOUNDARY LAYER ATMOSPHERE: RESULTS FROM THE GREAT PLAINS IRRIGATION EXPERIMENT (GRAINEX)

Emilee Jo Lachenmeier, M.S.

University of Nebraska, 2020

Advisors: Rezaul Mahmood and Trenton Franz

Modification of natural prairie grasslands into irrigated and rainfed agriculture in the Great Plains produced significant impacts on regional weather and climate including temperatures, precipitation, energy fluxes, and the planetary boundary layer (PBL) atmosphere. The Great Plains Irrigation Experiment (GRAINEX) during the 2018 growing season collected data over irrigated and non-irrigated crop fields to further understand these impacts.

The data were collected during two intensive observation periods (IOPs) in early June (IOP 1: 30 May – 13 June of 2018) and late July (IOP 2: 16 July – 30 July of 2018). The data analyzed include latent (LE) and sensible (H) heat fluxes, air temperature, dew point temperature, specific humidity, equivalent temperature (moist enthalpy) which were assessed using ground based sensors, PBL and lower tropospheric development which was assessed using radiosonde data. In addition, near surface soil moisture data were used to model root zone soil moisture utilizing Wang et al. (2017) Exponential Filter Model.

Results show increased partitioning of energy into latent heat compared to sensible heat over irrigated areas. It is particularly noticeable during IOP 2 when, on average LE was about ~15 W m^{-2} higher than H. At the same time, average maximum air temperature decreased by ~2.75 °C from IOP 1 to IOP 2. Implementation of the Wang et. al (2017) Exponential Filter Model indicated periods of notable drying and wetting throughout the site profiles reflective of an increase in water use by plants and rain or irrigation events. Radiosonde data suggest reduced PBL heights at all launch sites from IOP 1 to IOP 2 with larger changes over irrigated areas (up to ~812 meters). Compared to IOP 1, lifting condensation level (LCL) heights were also lower during IOP 2 over irrigated areas. In addition, six one-day case studies were completed to further understand land-atmosphere (L-A) interactions in the context of irrigated and non-irrigated land uses. They further corroborate IOP-wide results.

ACKNOWLEDGMENTS

Throughout the writing of this master's thesis, I have received the help of many individuals who are greatly deserving of recognition for their support and assistance.

First, I would like to thank my thesis advisor, Dr. Rezaul Mahmood, for providing me with the resources and connections necessary to navigate the large data sets and complex analyses involved in this project. His guidance and support allowed for my successful completion of this degree. His ability to adapt to advising remotely amidst the restrictions of a pandemic were invaluably helpful in maneuvering through a very difficult academic obstacle.

Second, I would like to thank my co-advisor, Dr. Trenton Franz and committee member, Dr. Michael Hayes. Their support, contributions and feedback throughout the research and writing processes have been greatly appreciated. Their dedication to assisting in my academic success was an encouraging push that propelled me through the completion of my degree.

Third, I would like to thank several individuals who offered assistance to me at different times throughout my master's program: Eric Rappin, Aaron Kaulfus, Linda Cully, Steve Oncley, Roger Pielke Sr. for answering my questions and addressing any issues I had pertaining to the GRAINEX data set and methods of calculating variables for my final analysis; Patty Swanson and Terri Easton, for keeping me on track with deadlines and answering any questions I had pertaining to the requirements of my degree; and Judson Buescher and Matt Wilson for offering their help as I learned Python programming in order to analyze and plot the GRAINEX data.

Fourth, I would like to thank a number of agencies most importantly the National Science Foundation (Grant AGS-1853390) for funding my research. I would also like to thank the School of Natural Resources and the High Plains Regional Climate Center for their support and encouragement to share my research and academic successes with colleagues.

Fifth, I would like to express my immense gratitude to my friends and family, without who I would never have been able to achieve this dream. The love and support from my mom and dad; Deb and Albert, my sister; Samantha, my boyfriend; Ryan and all my other friends and family were a daily reminder of how blessed and fortunate I am. My parents and sister have always been there to lend a sympathetic ear when I was stressed or overwhelmed, and Ryan was always able to provide happy distractions at the moments I needed them most. My friends and family have always recognized my academic successes and have been the biggest cheerleaders in my life, for which, I could never thank them enough.

Emilee Jo Lachenmeier

TABLE OF CONTENTS

LIST OF FIGURES

LIST OF TABLES

APPENDIX

FIGURES:

TABLES:

CHAPTER 1

INTRODUCTION

According to the Intergovernmental Panel on Climate Change Special Report (2019), observed average global land surface temperatures during the 2006-2015 decade were 1.53 °C higher than the 1850-1900 period. This global temperature increase and changes in precipitation patterns have notably caused shifts in growing seasons as well as fluctuations in the surface hydrologic cycle and expected crop yields (IPCC, 2019; Hatfield and Prueger, 2015; Linderholm, 2006). This is just one of many examples of how dramatically the global climate has changed within the past century. The reason for these changes has been linked to anthropogenic activities. The most common attribution of climate change is the emission of carbon dioxide (CO_2) into the atmosphere through the operations of industries, agriculture, and other socio-economic activities (Solomon et al., 2008; Pielke et al., 2007; Gullison et al., 2007). There are other human caused impacts pertaining to climate change that have received less attention including the alteration of prairie and range land into agricultural land, over grazing of natural rangeland and deforestation.

A significant amount of research regarding land use and climate interactions and impacts associated with deforestation have been conducted over the last several decades (Shukla et al., 1990; Zang and Henderson-Sellers, 1996; Zeng et al., 1996). Deforestation has been linked to a net warming in the tropics and net cooling in the mid-latitudes as well as changes in surface albedo. Regardless of high global

deforestation rates, more recently, forest growth, afforestation and reforestation have observed positive trends (Nagendra and Southworth, 2010). At the same time aggressive, large-scale transformation of the North American Great Plains have taken place (Mahmood and Hubbard, 2002) assisting in the 240% increase in cereal crop production since 1961 by means of large-scale agriculture operations (IPCC, 2019). This unprecedented transformation is viewed as necessary to support human societies with little regard for its impacts on weather and climate, among others.

The Pioneers of the Great Plains believed that "rain follows the plow" (Charles Dana Wilber, 1871) and although this has proven to be partially true given the role that land use land cover change (LULCC) has on modulating regional weather and climate (Pielke et al., 2011; Mahmood et al., 2010, 2014; Pielke et al., 2016), the quantification of these impacts were not studied in detail until recently (Szilagyi and Franz, 2020). Climate variables impacted include surface short and longwave radiation and atmospheric turbulence, which impacts momentum, heat, water vapor and carbon dioxide fluxes (Pielke et al., 2011). These impacts are further exacerbated by the widespread adoption of irrigation. Large scale irrigation has become an important part of the agriculture sector, especially within the United States where water resources are readily accessible. Estimates show that 76% of land used for agriculture in the High Plains Aquifer (HPA) region of the south-central U.S. (Nebraska, Kansas, Oklahoma, Texas, Wyoming, Colorado and New Mexico) is irrigated (by county) (Mahmood et al., 2014). With the addition of significant amounts of excess moisture being introduced

into an already modified system (i.e., LULCC), notable impacts on the normal climate are to be expected. Pielke et al. (2016) noted that a change in the climate can be broken down into a simple perturbation or forcing that causes variables to fluctuate from their normal state. These variables include temperatures, precipitation, and heat fluxes contributing to the system's energy balance. Regional climate tends to deviate from global trends due to faster and more extreme variations in water and energy fluxes (Kang et al., 2011) associated with land surface processes (Seneviratne et al., 2006). The increased application of water associated with irrigation practices modifies energy partitioning by reducing sensible heat flux, increasing latent heat flux (Mahmood et al., 2017) and suppressing maximum air temperature values (Huber et al., 2014; Diffenbaugh, 2009). An increase in latent heat flux is directly related to an increase in evapotranspiration (Pielke et al., 2007). An increase in evapotranspiration directly relates to moisture sequestered near the Earth's surface. With the introduction of irrigation, a general cooling in daytime air temperatures has been observed over irrigated regions (Mahmood et al., 2014; Mueller et al., 2016; Alter et al., 2017; Mueller et al., 2017; Gameda et at., 2007).

To better understand the impacts of LULCC on near surface environmental conditions and energy exchange, several field campaigns have been conducted (e.g., LeMone et al., 2007). To further improve upon these findings, the Great Plains Irrigation Experiment (GRAINEX) was conducted in southeastern Nebraska (Figure 1.1). This is the first field campaign solely focused on impacts of irrigation on Land-Atmosphere (L-A)

interactions. Southeastern Nebraska is a region where non-irrigated agricultural land transitions into a significant and widespread irrigated agricultural land (Mahmood and Hubbard, 2002; Adegoke et al., 2003; Lawston et al., 2015; Kukal and Irmak, 2018). The goal of this study was to collect and analyze data in regions of

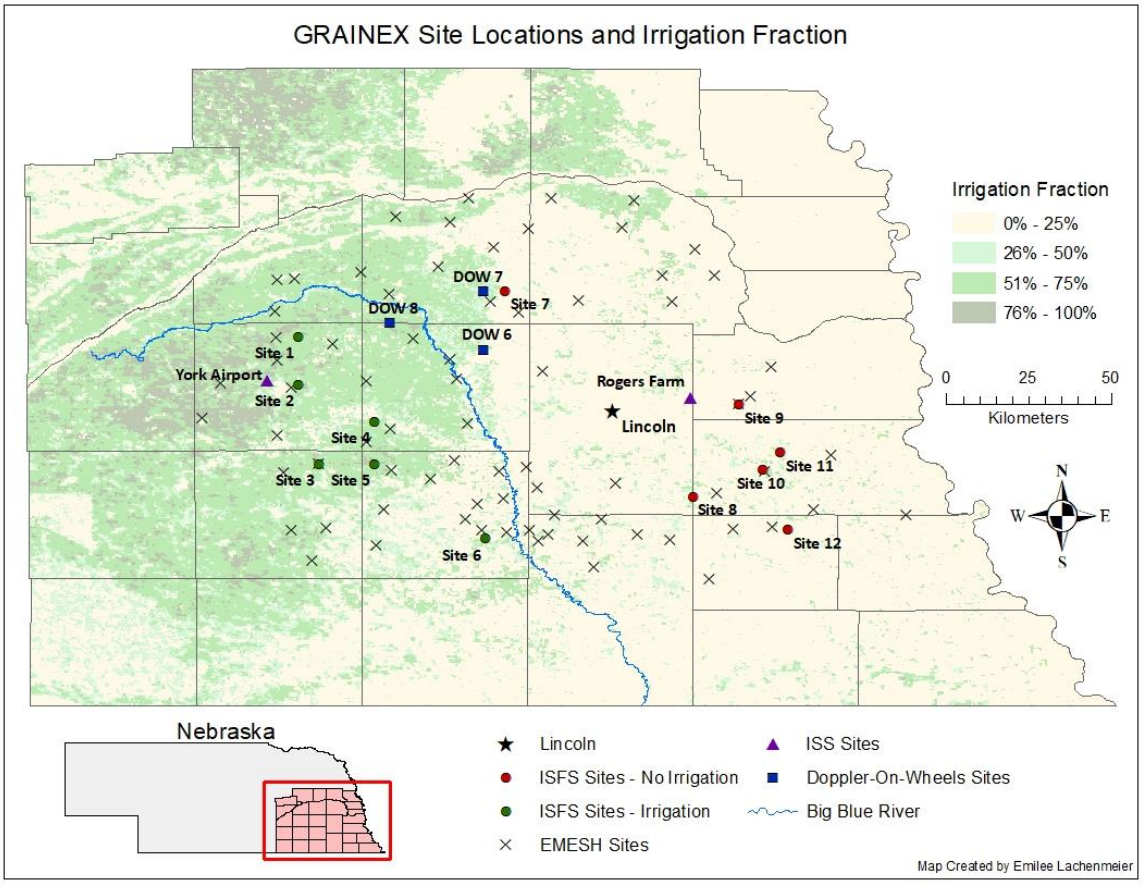

Figure 1.1: Map of the GRAINEX study area in southeast Nebraska. Data collection sites consisted of the twelve, integrated surface flux system sites (ISFS), two, integrated sounding system sites (ISS), three Doppler-on-Wheel deployment locations (DOWS), and the seventy-four Environmental Monitoring, Economical Sensor Hubs (EMESH) deployed by the University of Alabama in Huntsville. In addition, irrigation fraction and the Big Blue River are mapped to separate regions of irrigated and rainfed agriculture.

irrigated and rainfed agriculture in Southeastern Nebraska during the growing season of 2018 (late May through early August). The current research analyzed latent and sensible heat flux, near surface air temperature and moisture variables (dew point temperature, specific humidity), and radiosonde data to determine the impacts of irrigated and non-irrigated land uses on the near surface atmosphere and planetary boundary layer. In addition, an Exponential Filter Model produced by Wang et al. (2017) is applied for estimation of root zone soil water content (SWC).

The following chapters provide background of this study (Chapter 2), discuss data and methodology (Chapter 3), results from the GRAINEX project (Chapter 4), and finishes with conclusions (Chapter 5).

CHAPTER 2

BACKGROUND

Anthropogenic modifications resulting in changes to energy, water and momentum fluxes between land and atmosphere have both large and small scale climate change implications (Bonan, 1999). These contributions account for approximately 10-15% of CO_2 concentration increases in the atmosphere (Ciais et al., 2013). To fully understand how land use land cover change impacts the climate, we must consider both the biogeophysical and biogeochemical effects. The biogeophysical effects include modification to the environmental energy balance, the water budget and radiation balance (Pielke et al., 1998; Findell et al., 2007). Biogeochemical effects include the redistribution of nitrogen and carbon from land to atmosphere (Mahmood et al., 2016). The two are interconnected in the sense that biogeochemical fluxes depend on the biogeophysical characteristics (Pielke et al., 2017). For the purpose of this research, we will be focusing on biogeophysical impacts associated with LULCC.

Biogeophysical impacts are linked to the physical alteration of the landscape such as deforestation, urbanization, and conversion of rangeland to agriculture. As alluded before, changes in vegetation type and coverage area have a direct biogeophysical effect on climate through modifications to albedo and heat fluxes (Strandberg and Kjellstrom, 2018). Biogeophysical effects are difficult to quantify due to their dependency on local and regional characteristics such as soil moisture and type, available water for evapotranspiration, vegetation, snowpack, season length and

countless more (Strandberg et al., 2014; Alexandru and Sushama, 2016; Pielke et al., 2017). The following sections will discuss major areas of LULCC and their impacts on near-surface atmospheric variables.

2.1 Deforestation

Global and regional vegetation distribution significantly influences the mitigation of greenhouse gas emissions (Canziani and Benitez et al., 2012). Broadleaf and pine forests are one of the largest global carbon dioxide sinks (McGuffie, 1995) and rapid deforestation measures are aggressively reducing the sequestered CO_2 levels and increasing atmospheric CO_2 levels (Gitz and Ciais, 2004). Throughout the 1990s, an annual estimate of 1.5 billion metric tons of carbon, nearly 20% of the anthropogenic caused emissions, were released into the atmosphere (Gullison et al., 2007). Deforestation changes forest canopy cover, which allows for the preservation of soil quality and limits erosion from heavy rainfall events, directly impacting the hydrologic cycle by slowing and filtering surface runoff (Canziani and Benitez et al., 2012).

A larger number of research studies have been conducted in this area including field campaigns and modeling studies (e.g. Shukla et al., 1990; Silva et al., 2006; Sampaio et al., 2007; Medvigy et al., 2011; Moraes et al., 2012), which have brought to light new information about the impacts of deforestation on regional and global climates. Results from these studies suggest that deforestation creates higher surface albedo (i.e. and overall cooling effect), but this cooling is insignificant in comparison to the magnitude of

deforestation linked greenhouse gas induced warming (Forster et al., 2007; Brovkin et al., 2013). It is noted that reducing the global rate of deforestation is the most cost-effective option for long term climate change mitigation (Stern, 2006).

As the global demands for food and resources increase, so do biogeophysical impacts. A major driver causing these changes to take place is the assumed economic benefits that in many cases are nullified by the mitigation work following the destruction of the natural landscape (Mahmood et al., 2016). Some of the world's most extensively forested regions (i.e. Central and South America) have suffered greatly due to increases in the demand for agricultural goods and services (Canziani and Benitez et al., 2012). These demands have forced unprecedented levels of deforestation. Large expanses of forests in the tropics and the eastern portion of the United States, as well as tall grass prairies in the Great Plains, have been replaced with agricultural land (Bonan, 1999). The conversion of cleared areas into major agricultural crop operations has resulted in warmer and drier local conditions (Hahmann and Dickinson, 1997). Below we provide further discussions on the impacts of agriculture on weather and climate.

2.2 Agriculture

Success in the agricultural sector is highly dependent on weather and climate variability (Hayes and Decker, 1996; Anita et al., 2010; Challinor et al., 2014; Meijl et al., 2018). Climate is most widely viewed as an external forcing when assessing its role in agriculture (Pielke et al., 2007). Within the past century, the global expansion of

agriculture (and more specifically, in the Great Plains and Midwest regions of the United States) has taken place at an unprecedented rate (Adegoke et al., 2007). Natural forest and prairie systems have been cultivated to support the ever-growing global food demand but, until recently, the magnitude at which these LULCC shifts have impacted and are impacted by seasonal climatic variability was unquantified.

Continually, farmers must adapt to changes in growing season length and the number of growing degree days to ensure profitable crop production (Pielke et al., 2007; Anita et al., 2010). In addition, various biogeophysical properties are changed when vegetation modification takes place. These variables include but are not limited to, albedo, surface roughness, root zone depth soil moisture, soil quality, and leaf area index. The growing season albedos of crop and grass fields are relatively similar (Oke, 1987), but during the winter months when croplands expose bare soil, areas with full year native vegetation have higher albedos (Bonan, 2002). Both irrigated and non-irrigated crop land have taller vegetation (i.e. higher surface roughness) with broader leaf areas than native prairie grasses (Chase et al., 1999; Paruela et al., 2001; Bonan, 2002). Furthermore, moisture fluxes over agricultural crops are greater than grassland systems. This effect is even more pronounced with irrigated croplands (Chase et al., 1999).

Observed influences on climate and weather patterns related to these variables have been noted over a range of spatial and temporal scales (Adegoke and Carleton, 2000). In the Great Plains of North America, increases in growing season air

temperatures and decreases in precipitation have been notably impacting crop growth. To ensure that the plants have sufficient moisture and yields are consistent from year to year, the use of irrigation has been heavily implemented. Due to the great expansion of irrigation throughout the North American Great Plains, a further analysis of L-A interactions linked to significant moisture flux via irrigation must be discussed.

2.3 Irrigation

Irrigation has the potential to alter what was once unsuitable land for agriculture into highly fertile lands capable of growing a large range of crop types (Decker et al., 2017). As the need for more agriculturally developed lands have increased and expansion has taken place into previously uncultivated areas, the percentage of irrigated land has increased dramatically, specifically in the Great Plains of the United States. Huber et al. (2014) noted that irrigation changed the radiation balance, hydrologic cycle, and atmospheric patterns (including precipitation distribution and intensity) of the Great Plains. Modifications to the partitioning of sensible and latent heat fluxes have been linked to irrigation (Adegoke et al., 2003). With irrigation increasing regional moisture, a general cooling in daytime air temperatures have been observed. This is associated with the energy repartitioning, specifically the increase in latent energy flux (Mahmood et al., 2008; Lobell and Bonfils, 2008). The cooling effect has been observed during scenarios where the altered land surface significantly differed from the native cover (Mahmood and Pielke, 2017; Szilagyi and Franz, 2020). Practices

like irrigation intensify the instability of the system and exacerbates the impacts on the overlaying atmosphere (Pielke et al., 2016). Limited research has been conducted on the impacts irrigation have on characteristics of the planetary boundary layer.

This research aims to further expand upon previous findings regarding the interconnectivity between the surface and lower atmosphere considering irrigation which has been highly disregarded and or inappropriately represented by previous modelling and field research. As the need for irrigation increases, so does the need for continued research in order to quantify and potentially mitigate the inevitable impacts.

2.4 Irrigation and Atmosphere

Changes in air temperature, heat fluxes, and moisture associated with LULCC and the introduction of irrigation impacts the planetary boundary layer (PBL). The relationship between moisture, heat and the height of the PBL determines the rate at which convective systems can form and grow (Carleton et al., 2001). The stability of the lower troposphere is dependent on the local heating and winds. In areas where winds tend to converge, they act as a mixing and lifting mechanism for the heat and moisture fluxes from the surface. This mixing, if sufficient, can initiate areas of deep cumulus convections (thunderstorm development). Observations within the PBL can be made by deploying radiosondes, which provide a vertical profile of temperatures, winds, and moisture in the atmosphere. When these tools are used to compare regions of human influence and natural landscape, significant differences are observed in the amount of

cooling and moisture availability. In regions where irrigation is present, the landscape produces a cooler air temperature profile, but an overall increase in the presence of moisture as compared to a standard short grass prairie. In addition, vegetation also has a notable influence on vertical mixing. A study, conducted by Pielke et al. (2007), noted that an increase in moisture in the lower atmosphere associated with irrigation and increased evapotranspiration (ET) can have an enhancing effect on the convective boundary layer and in turn, increase precipitation. Moisture exchange within the PBL proved to play a role in the convective available potential energy (CAPE) leading to increased instability and daytime cumulus. Wetzel et al. (1996) investigated the formation of convective precipitation over sparsely vegetated land and a deciduous forest. Results showed that development of convective precipitation was delayed (1-2 hours) due to the suppressed mixing caused by the higher canopy of the forested landscape. It was also observed that in moisture starved conditions, areas of high sensible heat flux were significantly better at cumulus cloud formation than over areas dominated by latent heat flux. This finding supports the claim that the depth of the PBL is directly correlated with the amount of sensible heat flux into the atmosphere when moisture is limited.

Another approach to quantifying the effects of LULCC on regional and local climates is to implement modeling techniques. In a study by Adegoke et al. (2003), a Regional Atmospheric Modeling System (RAMS) was used to evaluate the surface heat fluxes related to irrigation and how they effected the convective potential in Nebraska.

A series of land use scenarios were considered for this study in an effort to best define the irrigation distribution of Nebraska. The resulting model runs corresponded well to the observed maximum, minimum and dew point temperatures. This validated the calculated flux responses, which showed that cooling at the surface in connection with irrigation increased the amount of latent heat flux by 36% and water vapor flux 500 meters above the surface by 28%. Other responses included a 15% reduction in sensible heat flux and elevated dew point temperatures. Variables such as albedo, surface roughness length changes, and increased soil moisture cannot be overlooked in order to accurately model the differences between irrigated and non-irrigated systems.

2.5 Justification for Research

It is evident that LULCC notably impacts weather and climate. However, additional research is needed for better understanding between LULCC-weather-climate interactions. To this end, there is a significant void in observed atmospheric data that could show linkages between irrigated and non-irrigated land uses and evolution of the near surface meteorology and lower troposphere. To meet this need, the GRAINEX field campaign was conducted. This thesis analyzes data collected by the GRAINEX campaign to investigate impacts of irrigated and non-irrigated land uses on the near surface meteorology, L-A interactions, and PBL development.

CHAPTER 3

DATA AND METHODOLOGY

3.1 GRAINEX Overview

The GRAINEX field campaign was conducted in southeast Nebraska from late May through early August of 2018. Nebraska, located within the North American Great Plains, is one of the most extensively irrigated regions in the world. The primary source of water is the High Plains Aquifer which is also known as the Ogallala Aquifer. As shown in Figure 1.1, a concentrated area of irrigated cropland is found to the west of the Big Blue River and alternatively, non-irrigated rainfed cropland is found to the east.

This study included two intensive-observation periods (IOPs) during which all data were collected. The first phase took place from 30 May to 13 June (IOP 1). The second phase from 16 July to 30 July (IOP 2). The window of dates for IOP 1 was chosen in an effort to observe L-A interactions amidst the early onset of irrigation (i.e. a rapid increase in moisture availability in both surface and subsurface regions). IOP 2 was chosen to capture L-A interactions during the peak growing season when the irrigation amount is maximized in response to crop-water demand.

A variety of observational platforms were used for data collection. These included twelve Integrated Surface Flux Systems (ISFS), two Integrated Sounding Systems (ISS), three Doppler on Wheels (DOW) mobile radar units, which also deployed radiosondes and Environmental Monitoring, Ecological Sensor Hubs (EMESH) (Photos of

the GRAINEX sites can be found in the Appendix). Further details including a description of the instrumentation, data collected and quality of data from each observational platform are discussed in the following sections. The National Aeronautical and Space Administration (NASA) also participated by collecting soil moisture data using radiometers mounted on a Twin Otter aircraft.

3.1.1 Integrated Surface Flux Systems (ISFS)

A total of twelve ISFS sites were deployed for the GRAINEX campaign. Six sites were deployed in irrigated crop environments, six in non-irrigated (Fig. 1.1, Table 3.1). The six irrigated sites were located in the western irrigated part of the study area (i.e. west of the Big Blue River), and the remaining six in the eastern non-irrigated part. The meteorological and environmental parameters measured at the ISFS sites included latent and sensible heat fluxes, air temperature, relative humidity, pressure, precipitation, wind speed, wind direction, incoming and outgoing solar radiation, and soil moisture. Specifics regarding the sensors used to collect these variables can be found in Table 3.2.

Table 3.1. Locations and descriptions of ISFS sites including nearby town, geographical coordinates and additional characteristics.

Location and Descriptions of GRAINEX ISFS Sites						
Site	**Nearest Town**	**Latitude (deg N)**	**Longitude (deg W)**	**Fetch North**	**Fetch South**	**Surface Soil Type**
1	Benedict, NE	41.00967	-97.5412	NA	Corn (rad)	Hastings Silt Loam
2	York, NE	40.87961	-97.5419	Soy (rad)	Soy	Hastings Silt Loam
3	Exeter, NE	40.66228	-97.4846	Corn	Corn (rad)	Butler Silt Loam
4	Beaver Crossing, NE	40.77854	-97.3317	Soy	Corn/soy (rad)	Butler Silt Loam/Crete Silt Loam
5	Friend, NE	40.66222	-97.3335	Corn	Corn (rad)	Hastings Silty Clay Loam
6	Wilber, NE	40.4585	-97.0289	NA	Corn (rad)	Crete Silt Loam
7	Loma, NE	41.13573	-96.9744	Corn/grass (rad)	Soy	Yutan Silty Clay Loam
8	Panama, NE	40.57374	-96.4618	Corn (rad)	Corn	Wymore Silty Clay Loam/Pawnee Clay Loam
9	Elmwood, NE	40.8238	-96.3352	Corn	Corn (rad)	Wymore Silty Clay Loam
10	Unadilla, NE	40.64591	-96.2713	Soy	Corn (rad)	Wymore Silty Clay
11	Unadilla, NE	40.6932	-96.2232	Corn	Soy (rad)	Wymore Silty Clay Loam
12	Cook, NE	40.4831	-96.2026	Soy	Corn (rad)	Wymore Silty Clay Loam/Wymore Silty Clay

Table 3.2. Measurements taken at the ISFS sites and the respective sensor used during deployment

GRAINEX ISFS Site Variables and Sensors	
Variables	**Sensor**
Air temperature	NCAR TRH
Air pressure	Vaisala PTB220, PTB2010 barometers; Paroscientific nanobarometer
Carbon dioxide	Campbell CSAT3A/EC150
Horizontal wind speed/direction	Gill WindObserver 2D sonic anemometer
Momentum fluxes	Campbell CSAT3A/EC150
Precipitation (rain)	MRI tipping bucket
Radiation (4-components)	Hukseflux NR01 integrated radiometer
Relative humidity	NCAR TRH
Sensible/latent heat	Campbell CSAT3A/EC150
Soil heat capacity	Hukseflux TP01
Soil heat flux	REBS HFT
Soil moisture	Decagon EC-5
Soil temperature	NCAR Tsoil

Data for all of the ISFS sensors were collected at a sample rate of 50 samples per second, which was relayed in near real-time to the Lower Atmosphere Observing Facilities (LAOF), Earth Observing Laboratory (EOL) via cell modem. ISFS sites continually recorded data throughout the full project period, but a small amount of data were lost due to equipment malfunctions. The entire data set was quality-controlled and released to the EOL/NCAR data portal as five-minute averages in NetCDF format (https://data.eol.ucar.edu/master_lists/generated/grainex/). Variables collected at the ISFS sites were graphically analyzed and T-tests were conducted to evaluate the statistical significance of the differences in irrigated and non-irrigated air temperature, dew point temperature, and specific humidity during IOP 1 and 2 separately.

3.1.2 Integrated Sounding Systems (ISS)

In addition to the ISFS sites, two ISS sites were assigned in an effort to capture anomalies in the PBL associated with irrigated and non-irrigated agricultural practices (Table 3.3). The first ISS site was located at the York Airport in York, Nebraska, a small airfield along the I-80 corridor. Nearby crop fields are extensively irrigated and radiosonde launches were conducted in an area displaced from runway activities. The second ISS site was located at Rogers Memorial Farm (Rogers Farm), a University of Nebraska owned and operated test farm east of Lincoln. This site lies within the confines of the non-irrigated ISFS sites. Radiosonde launches took place simultaneously at two-hour intervals from sunrise (Approx. 6:00 AM Local Time) to sunset (Approx. 8:00 PM Local Time) each day. In other words, eight radiosonde launches were completed each day from each site resulted in about 480 launches (8 launches x 2 sites x 30 days = 480 launches). These sites also operated a wind profiler, a ceilometer and collected surface meteorological observations (Table 3.4).

Table 3.3. Locations and descriptions of ISS sites.

Location and Descriptions of GRAINEX ISS Sites			
Site	**Description**	**Latitude (deg N)**	**Longitude (deg W)**
ISS2	Rogers Memorial Farm, Lincoln	40.8444	-96.4683
ISS3	York Municipal Airport	40.8916	-97.6261

Table 3.4. Measurements taken at the ISS sites and the respective sensor used during deployment

GRAINEX ISS Site Variables and Sensors		
System	**Variables**	**Sensor**
Upper Air	Cloud Height	Vaisala CL31 and CL51 Ceilometer
	Sounding Variables	Vaisala MW41/RS 41 Radiosondes
	Wind profile	LAP3000 915 MHz DBS wind profiler with RASS
Surface	Pressure	PTB210
	Radiation (4-components)	Hukseflux NR01
	Precipitation (rain)	HAS Tipping Bucket
	Meteorological Summary - Air Temperature - Relative humidity - Precipitation type - Precipitation intensity - Precipitation quantity - Air pressure - Wind direction - Wind speed - Radiation	WS700/800 Weather Sensors

These sites were only operational during IOP 1 and 2, therefore, this analysis of the GRAINEX data highlights events constrained by these time windows. This will provide the most comprehensive data set to be used to develop conclusions in regards to how LULCC associated with agriculture and irrigation impact the development of features within the PBL.

3.1.3 Doppler on Wheels (DOW)

Three DOW units were deployed and triangulated over a transition region between irrigated and non-irrigated crop land (Table 3.5). This formation was assigned in order to capture fine-scale transitional variability from irrigated to non-irrigated areas and vice versa. Doppler radar scans consisting of reflectivity and velocity fields were

conducted in order to identify boundary formations and severe weather development within the PBL. The DOW sites also conducted radiosonde launches, which corresponded to the launch times of the ISS sites. In total, approximately 24 launches were conducted per day (technical issues/early termination resulted in some launches being missed), totaling about 720 launches. Overall, taking into account all of the days included in IOP 1 and 2, the resulting radiosonde total for the GRAINEX project totaled approximately 1200 launches. For the purpose of this study, radiosonde data at both the ISS and DOW sites were analyzed. Future analysis of the radar scans are highly anticipated to further investigate convective development associated with irrigation.

Table 3.5. Locations and descriptions of DOW sites.

Location and Descriptions of GRAINEX Doppler on Wheels (DOW) Sites			
Site	**Nearest Town**	**Latitude (deg N)**	**Longitude (deg W)**
DOW6	Bee, Nebraska	40.97387	-97.03419
DOW7	Dwight, Nebraska	41.13317	-97.03346
DOW8	Surprise, Nebraska	41.04693	-97.2912

3.1.4 Environmental Monitoring, Ecological Sensor Hubs (EMESH)

To expand upon the surface observation coverage of the ISFS sites, the University of Alabama in Huntsville developed a network of rapidly deployable weather stations that were deployed and recorded observations throughout the GRAINEX project window (late May to early August of 2018). The network consisted of 74 meteorological stations that were placed in both irrigated (28 stations) and non-irrigated (47 stations) regions. A description of the EMESH stations locations can be found in the Appendix.

These stations have significant implications for future research but are not be referenced as part of this study.

3.1.5 NASA Goddard Radio Frequency Explorer (GREX) Instrument

As a method of observing transects of soil moisture amidst and between the deployed ground stations (ISFS and EMESH), NASA used one of its Twin Otter planes equipped with the GREX microwave (L-band) radiometer to conduct seven flights during the second IOP. The GREX radiometer conducts measurements at a < 1 km spatial resolution and is capable of measuring brightness temperatures similar to those observed by the Soil Moisture Active-Passive (SMAP) satellite. The two observational radiometers (SMAP and GREX) operate on very similar frequencies (1400 to 1427 MHz). With the addition of the data collected during these flights, a spatial analysis of soil moisture gradients, soil property transition zones, as well as a comparison of point measurements to those measured by the GREX sensor, can be conducted as part of future research. These data are currently undergoing the QA/QC process and were not discussed in this study.

3.2 Calculation of Latent and Sensible Heat Flux

A number of numerical calculations were required to fully utilize the data collected during the GRAINEX project, including those for latent (LE) and sensible (H)

heat flux. Using the observed variables and R code archived with the GRAINEX data set, values for LE and H were calculated with the following equations:

$$LE = L_v * \rho_{air} * w'mr' * (1x10^{-3}) \quad \text{(Equation 1)}$$

$$H = \rho_{air} * ((C_{pd} * w't') + (C_{pv} * T * w_q * (1x10^{-3}))) \quad \text{(Equation 2)}$$

where L_v is the latent heat of vaporization ($2.5x10^6$ Jkg^{-1}), ρ_{air} is the density of air calculated by dividing pressure (Pa) with the product of the gas constant R (287 $JKg^{-1}K^{-1}$) and air temperature T (K), C_{pd} is the specific heat of dry air at a constant pressure (1006 $JKg^{-1}K^{-1}$), C_{pv} is the specific heat of water vapor at a constant pressure (1857 $JKg^{-1}K^{-1}$), w_q is a directional component of water vapor density (ms^{-1} gm^{-3}), and $w't'$ and $w'mr'$ are correction factors calculated using specific humidity, the density of air, air temperature (K), pressure (Pa), virtual air temperature from the speed of sound and water vapor density. The correction factor is implemented in an effort to account for variability in wind (speed and direction) influencing water vapor flux. Finally, a multiplicand is added to make the output values in units of Wm^{-2}.

Values for air temperature, pressure, and w_q were collected and archived into the GRAINEX dataset. Latent and sensible heat were calculated using the ISFS 5 minute, quality controlled dataset and were later used to create 30 minute, full day (Midnight to Midnight) and daytime (11 to 1 UTC; 6:00 AM to 8:00 PM LT) averages. To test for statistical significance between irrigated and non-irrigated latent and sensible heat

during IOP 1 and IOP 2 separately, T-Tests were conducted on the 30-minute daytime data and daytime averages.

3.3 Calculations of Equivalent Temperature

Further analysis of the L-A interactions observed during GRAINEX required the calculation of equivalent temperature (T_E), a variable best utilized for expressing changes in heat content related to changes in moisture (i.e. moist enthalpy) (Pielke et al., 2004). Equivalent temperature can be expressed as follows:

$$H = C_pT + L_vq \quad \text{(Equation 3)}$$

where H is moist enthalpy (JKg^{-1}), C_p is the isobaric specific heat of air (1005 $JKg^{-1}K^{-1}$), T is air temperature (K), L_v is the latent heat of vaporization ($2.5x10^6$ Jkg^{-1}) and q is specific humidity. Specific humidity, a variable not available in the GRAINEX dataset was calculated using the two equations below and compared for consistency before completion of the equivalent temperature calculations:

$$\text{(Method 1) } q = w / (w + 1) \quad \text{(Equation 4)}$$

$$\text{(Method 2) } q = (0.622 * e) / (P – (0.378 * e)) \quad \text{(Equation 5)}$$

where w is the mixing ratio, calculated from measurements of air temperature, relative humidity and pressure, e is the vapor pressure of air calculated using measured values of dew point temperature applied to Bolton's (1980) empirical relationship and P is observed pressure. After comparison of these two calculation methods, it was

determined that the differences were insignificant and values for q from Method 1 were used. Finally, to convert moist enthalpy into units of temperature (K), thereby creating a variable comparable to air temperature that more completely represents atmospheric heat can be expressed as follows:

$T_E = H / C_p$ …… *(Equation 6)*

Values of T_E were then compared to observed air temperatures at the individual ISFS sites and later averaged over the six irrigated and six non-irrigated sites separately. Once again, T-tests of the 30-minute daytime (11 to 1 UTC; 6:00 AM to 8:00 PM LT) data and daytime averages were conducted to determine the statistical significance between irrigated and non-irrigated equivalent temperature during IOP 1 and IOP 2 separately.

3.4 Soil Moisture Model

To further understand L-A interactions, a soil modeling component was included. Based on Wang et al. (2017), an Exponential Filter Model was applied to the 5 cm soil moisture data collected during GRAINEX to create a full root zone moisture profile. The original purpose of this Exponential Filter Model was to expand upon soil moisture data collected through airborne and satellite observations. These datasets are restricted to the near surface due to penetration depths of the onboard sensors being limited to the top ~5 cm of the soil profile. Through study and application of the interconnectivities

between surface and root zone soil moisture, Wang et al. (2017) constructed this model and current research (including this project) has been testing its uses and limitations.

To apply the Exponential Filter Model, textural components of the site soils were required. For this thesis, the USDA web soil survey was used to determine these percentages for each of the 12 ISFS sites. In order to calculate the optimum characteristic time length, T_{opt}, a regression curve was matched to the plot of the sand and clay percentages from each site. This method of calculating T_{opt} was modelled after Wang et. al. (2017). In addition, 95 percent confidence intervals were calculated but results were insignificant and were not included in the soil moisture model runs. The T_{opt} parameter, which is uniquely designed to represent the soil characteristics at a specific depth in order to estimate moisture transition speeds through a given layer in the profile, was calculated for both 25 cm and 50 cm depths and used as a model input along with 5 cm soil moisture in percent volume. Other site specific variables used in the model included time of year, time of day, and latitude and longitude coordinates.

The model uses 5 cm observed data from the ISFS sites as an input to simulate daily soil moisture for 25 cm and 50 cm for late May through early August. In order for the model to be properly assimilated by the start of IOP 1, 5 days of data were added to the beginning of each model run. According to Wang et al. (2017), the simplicity of the Exponential Filter Model allows for the extrapolation of the surface moisture to root zone depths in varying climatic and land surface conditions, which is representative of the conditions under observation during the GRAINEX field campaign. The resulting

model runs at the 12 ISFS sites are presented in this paper, but potential remains for future cross analysis and further application (with data from the EMESH sites and NASA flights).

3.5 Lower Atmosphere Analysis

As indicated previously, approximately 40 radiosondes were launched daily during the first and second IOPs of GRAINEX. By implementing radiosonde data collection into the project plan, a multidimensional view of lower atmospheric variabilities was constructed. From radiosonde data from both ISS sites (York Airport and Rogers Farm) and the three DOW sites, an analysis representing both irrigated and non-irrigated areas can be used to study how variables such as planetary boundary layer height are impacted by irrigation. By developing a Python code for plotting the radiosonde data onto skew-T log*p* graphs, important measures including the lifting condensation level (LCL), the level of free convection (LFC), and PBL height can be calculated and plotted for analysis. The LCL can be defined as the level at which water vapor starts to condense inside of a dry-adiabatically lifted parcel (American Meteorological Society, 2012) and the LFC can be expressed as the level at which a parcel's air temperature is decreasing more rapidly than the moist adiabatic lapse rate at that same level (American Meteorological Society, 2012). These measures are widely used in meteorological research (Schrieber et al., 1996; Craven et al., 2002; Muñoz et al., 2015; Romps, 2017; Brown and Nowotarski, 2019).

Using MetPy functions in Python, the values for the LCL and LFC can be calculated (Unidata, 2020a, 2020b). For the purpose of this study, the PBL height was determined to be the height at which the calculated bulk Richardson number (R_i) is equal to 0.25. To determine this height, the R_i was calculated for all points within the sounding profile using the following equation:

$$R_i = [(g/T_v)\,\Delta\theta_v\,\Delta z] / [(\Delta U)^2 + (\Delta V)^2] \quad \text{(Equation 7)}$$

Where g is gravitational acceleration (9.81 ms^{-1}), T_v is the virtual temperature (K), $\Delta\theta_v$ is the virtual potential temperature (K), Δz is the thickness of the layer between the surface and point of interest and ΔU and ΔV are the changes in horizontal and vertical wind across the layer z, respectively. The established threshold of 0.25 (critical Richardson number) was then used to return a height (this is the PBL height) and plot a line corresponding to this height on the skew-T log$p$ diagram. Being able to visually analyze this variable will allow for the comparison of PBL height over irrigated and non-irrigated areas as well as during windows of significant precipitation or excessive dryness. PBL height was also used along with LCL and LFC to determine impacts of irrigation on convective environment.

CHAPTER 4

RESULTS

4.1 Near Surface Meteorology

The meteorological variables collected at the ISFS sites during GRAINEX include, among others (Table 3.2), 2-meter air temperature and relative humidity, which were recorded at 5 minutes intervals. These variables were used to calculate (see data and methodology) dew point temperature and specific humidity. Utilizing the 5-minutes air temperature, dew point temperature and specific humidity, 30-minute, hourly and daily averages were calculated. Minimum and maximum values were also considered during analysis. To further understand changes in these variables linked to irrigation, averages for the six irrigated (ISFS 1 through 6) and six non-irrigated sites (ISFS 7 through 12) were calculated. The results of this analysis are shown in Figures 4.1-4.3. Values corresponding to Figure 4.1-4.3 can be found in the Appendix (Table A.2-A.5).

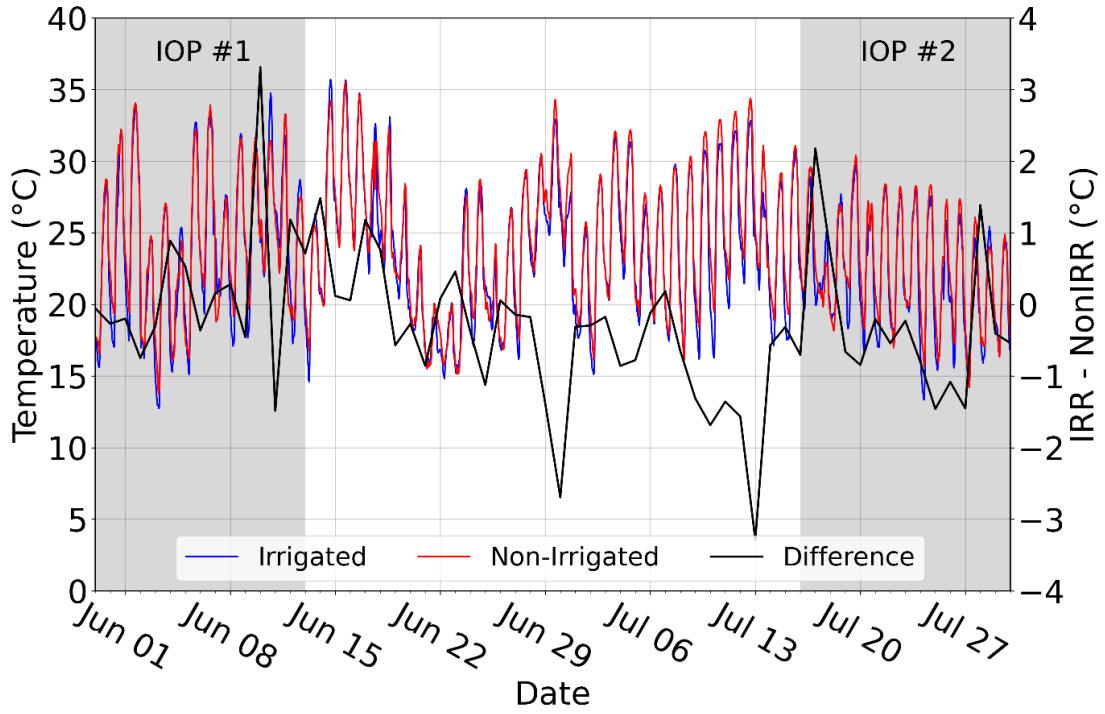

Figure 4.1: 30-minute air temperatures averaged over the 6 irrigated and 6 non-irrigated sites during the growing season of 2018. Note: A comparison of irrigated and non-irrigated air temperatures during IOP 1 resulted in no statistical significance, but IOP 2 comparisons resulted in statistically significant differences.

An analysis of air temperature, dew point temperature and specific humidity data reveal notable differences in near-surface meteorological conditions over irrigated and non-irrigated land uses during IOP 1 and IOP 2. During IOP 1, observed air temperatures at irrigated and non-irrigated sites were quite similar, with daily maximum differences remaining consistently around 0° C. Deviations from this pattern corresponded to precipitation events. Due to the active synoptic conditions during IOP 1, frequent fluctuations in irrigated and non-irrigated daily maximum air temperatures were observed over the study area. On the other hand, overall, IOP 2 experienced larger and more consistent differences between air temperatures over irrigated and non-

irrigated areas. The difference in average temperatures for the irrigated and non-irrigated ISFS sites were 0.15 °C for IOP 1 and 0.42 °C for IOP 2. Average maximum air temperature differences were slightly larger with a spread of 0.29 °C for IOP 1 and 0.60 °C for IOP 2. This was due to the applications of irrigation resulting in higher latent heat fluxes and lower sensible heat fluxes (Additional discussions are provided in Section 4.2) during the peak growth period of the plants.

Much like air temperature, differences between dew point temperature over irrigated and non-irrigated croplands were small in the early growing season (IOP 1;). In fact, the average dew point temperature over irrigated areas were slightly lower (20.34 °C) compared to non-irrigated areas (20.79 °C) (Table A.2). On the other hand, around the first week in July, when irrigation applications became more frequent, dew point temperatures at the irrigated sites were noticeably greater than the non-irrigated sites. It is found that average dew point temperatures over irrigated and non-irrigated areas were 22.67 °C and 21.57 °C during IOP 2, respectively (Table A.2). In other words, there was a 1.10 °C increase in dew point temperatures over irrigated areas during IOP 2. Figure 4.2 depicts this midseason shift and elevated dew point temperatures over irrigated sites during IOP 2.

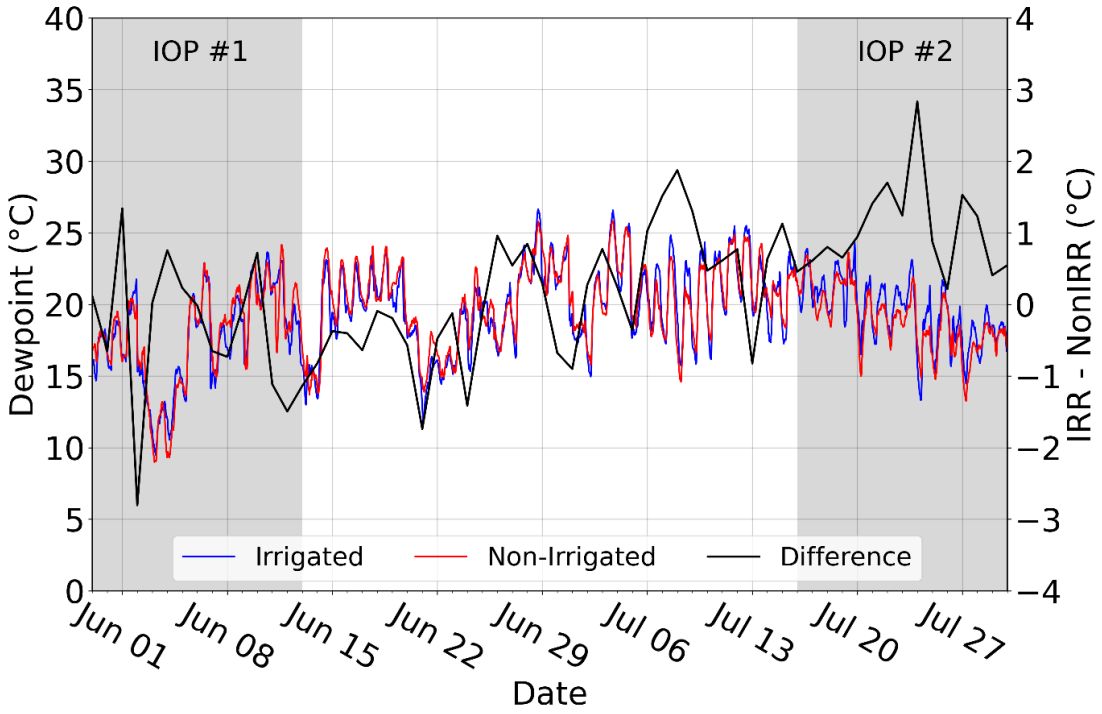

Figure 4.2: 30-minute dew point temperatures averaged over the 6 irrigated and 6 non-irrigated sites during the growing season of 2018. Note: A comparison of irrigated and non-irrigated dew point temperatures during IOP 1 resulted in no statistical significance, but IOP 2 comparisons resulted in statistically significant differences.

Another measure of atmospheric moisture associated with irrigation, as well as precipitation events, can be represented by specific humidity. Figure 4.3 reveals that, on average, specific humidity was somewhat similar over irrigated and non-irrigated sites during IOP 1, while there was a clear mid-growing season increase over irrigated areas during IOP 2 over irrigated croplands.

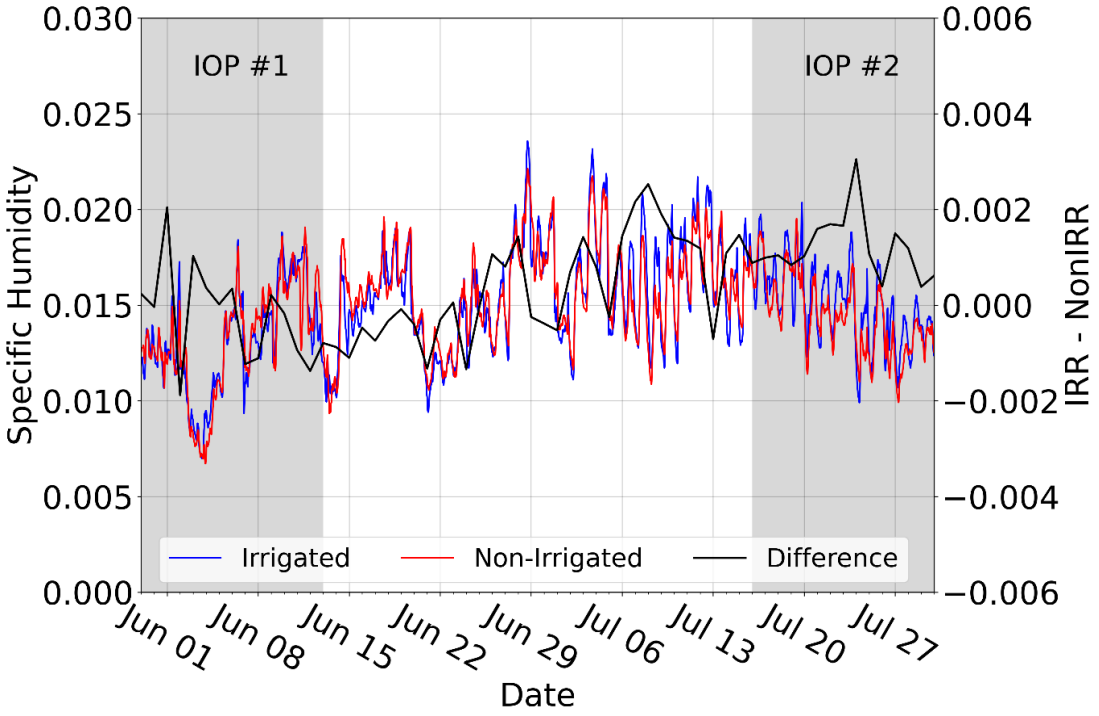

Figure 4.3: 30-minute specific humidity averaged over the 6 irrigated and 6 non-irrigated sites during the growing season of 2018. Note: A comparison of irrigated and non-irrigated specific humidity during IOP 1 resulted in no statistical significance, but IOP 2 comparisons resulted in statistically significant differences.

4.2 Heat Fluxes

As noted in Chapter 3, measurements of latent and sensible heat flux were also made at the ISFS sites. During IOP 1 and 2, values of latent heat flux were greater than those of sensible heat flux (Fig. 4.4 and 4.5). Further inspection of these variables during the IOP windows reveals that differences in sensible and latent heat flux early in the growing season (IOP 1) were much less than the differences observed later into the growing season (IOP 2). These differences can be attributed to the increase in water

consumption by crops supplemented by the increased application of water through irrigation. The additional energy partitioned into plant growth is observed through the latent heat flux increases in IOP 2.

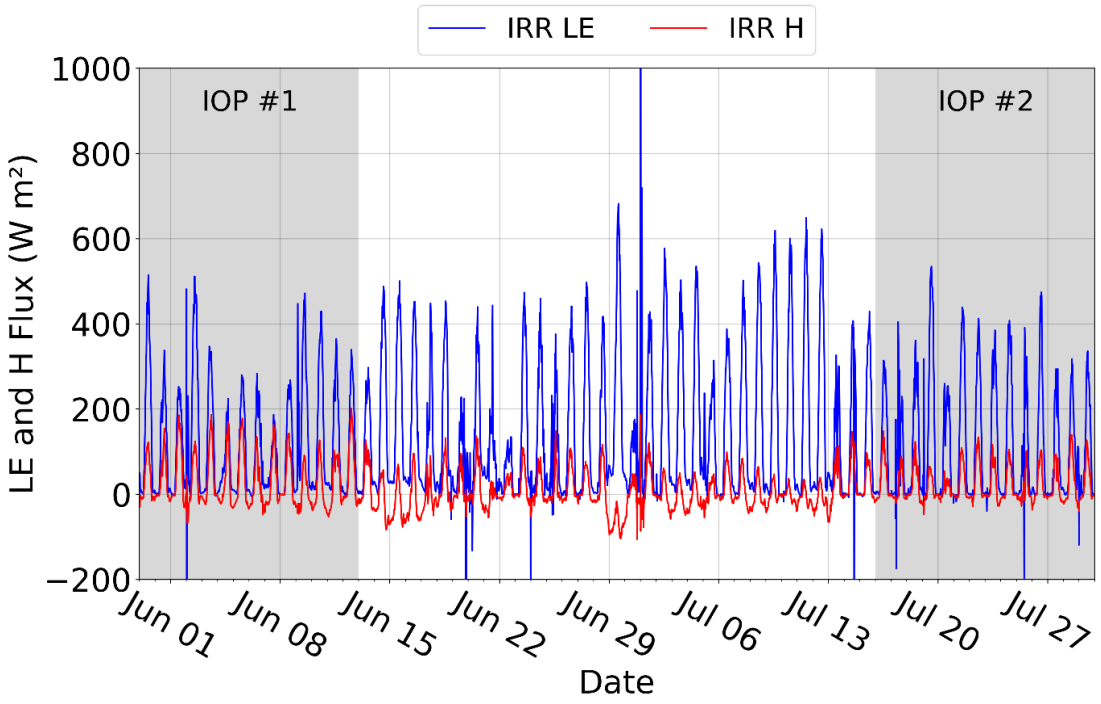

Figure 4.4: 30-minute latent (LE) and sensible (H) heat flux averaged over irrigated ISFS sites (1-6) during the growing season of 2018.

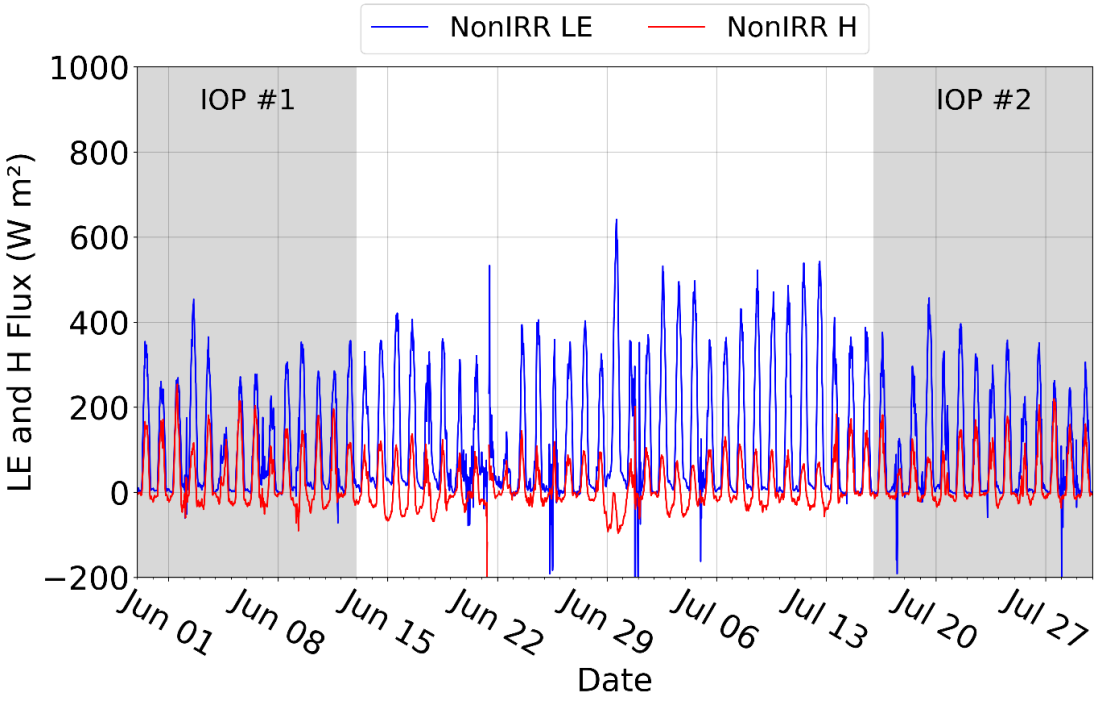

Figure 4.5: 30-minute latent (LE) and sensible (H) heat flux averaged over non-irrigated ISFS sites (7-12) during the growing season of 2018.

These responses can be observed in daily observations from an irrigated (Fig. 4.6 a-b) and non-irrigated (Fig. 4.6 c-d) site during IOP 1 and 2 (6 June and 24 July, respectively). Observed values of latent heat flux were substantially greater during the late growing season (IOP 2) over both irrigated (e.g., site 1) and non-irrigated (e.g., site 9) areas. An approximate difference of 200 W m^{-2} (100 W m^{-2}) between early and late season latent heat flux maximums was observed at the irrigated (non-irrigated) site (Figure 4.6 a-b and Figure 4.6 c-d respectively). In addition, magnitudes of latent and sensible heat flux differences became larger over irrigated sites during IOP 2. This suggests greater repartitioning of energy into latent heat flux linked to increased irrigation due to crop water demand.

A)

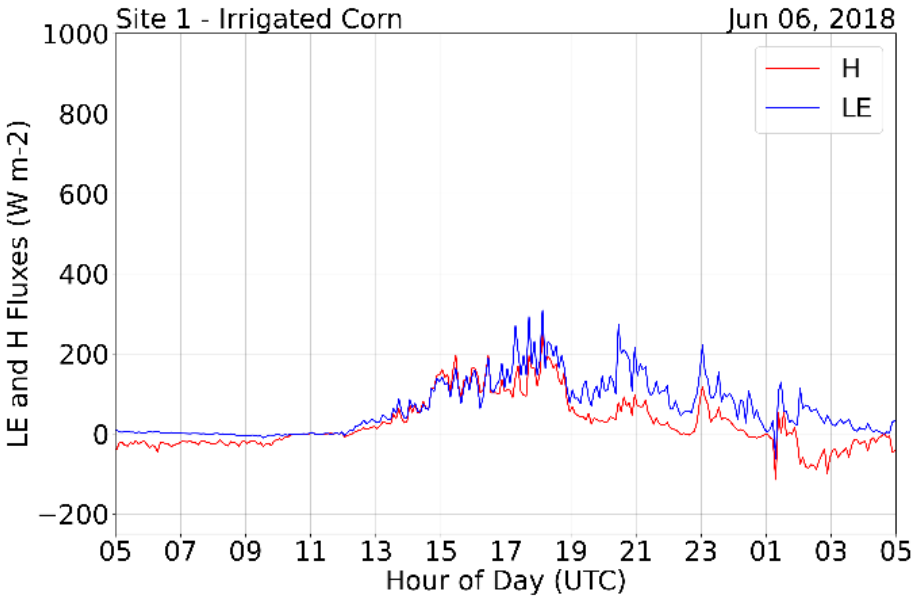
Site 1 - Irrigated Corn
Jun 06, 2018
H
LE
LE and H Fluxes (W m-2)
1000
800
600
400
200
0
−200
05 07 09 11 13 15 17 19 21 23 01 03 05
Hour of Day (UTC)

B)

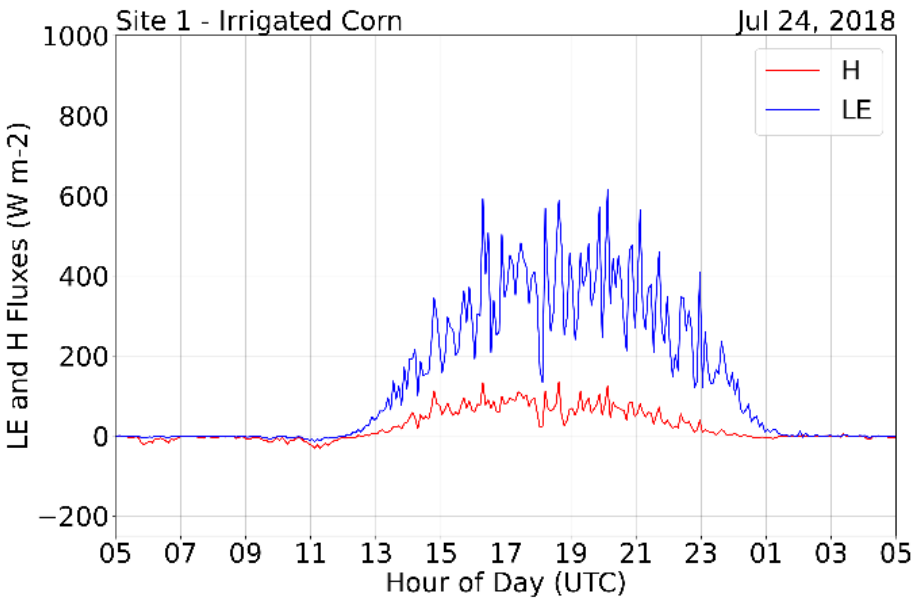
Site 1 - Irrigated Corn
Jul 24, 2018
H
LE
LE and H Fluxes (W m-2)
1000
800
600
400
200
0
−200
05 07 09 11 13 15 17 19 21 23 01 03 05
Hour of Day (UTC)

C)

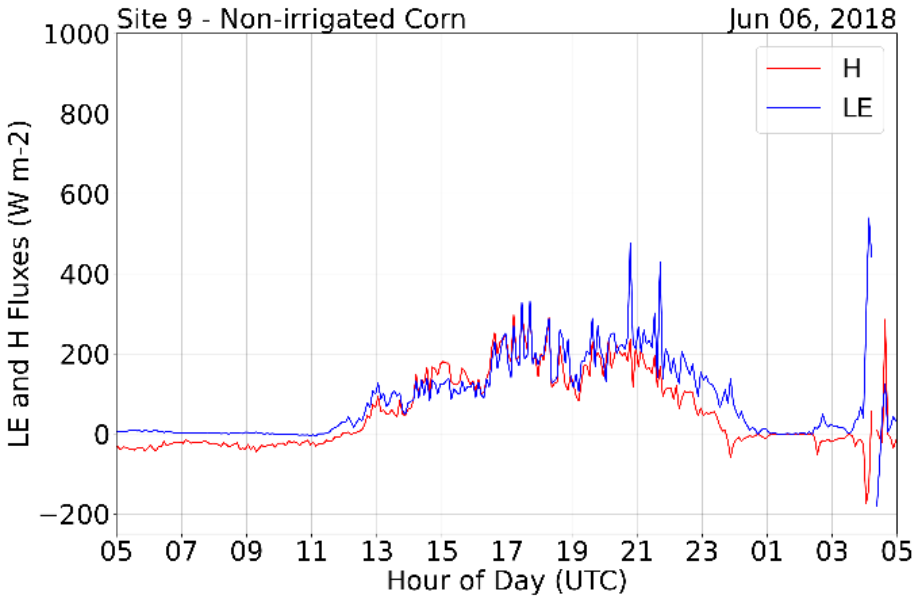

D)

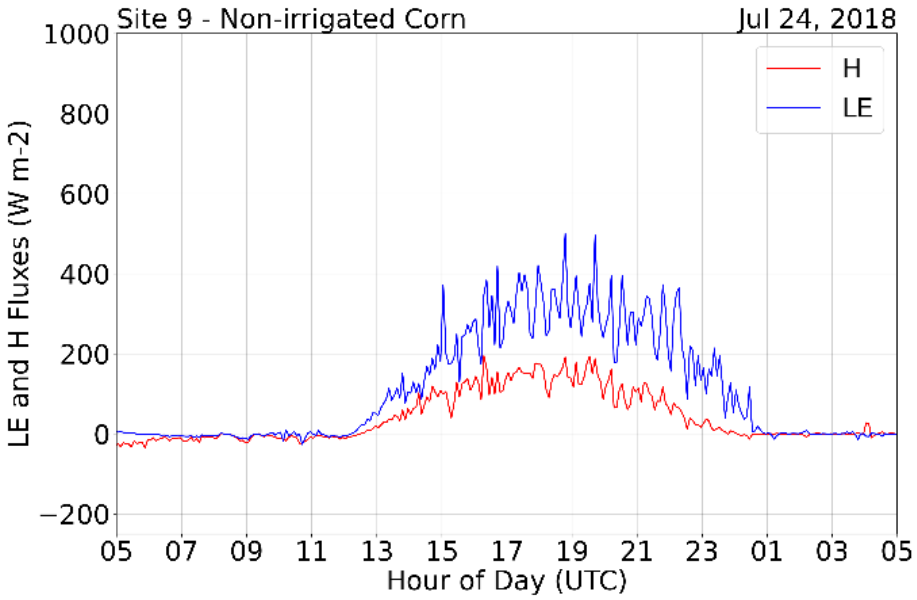

Figure 4.6: 5-minute latent (LE) and sensible (H) heat flux at ISFS site 1 (A,B) which is irrigated and site 9 (C,D) which is non-irrigated for 6 June (A,C) and 24 July (B,D).

When daily averages for IOP 1 (Fig. 4.7) and IOP 2 (Fig. 4.8) were compared, a consistent difference between latent and sensible heat flux values was also observed with latent heat fluxes dominating the daily averages. For IOP 1, higher values of latent heat flux were produced possibly by precipitation events, whose onset can be identified in the air temperature, dew point temperature, and soil moisture observations. Given the relatively wet conditions during the early growing season of 2018, signatures like that observed on 2 June in Figure 4.7 were similar to signatures produced from irrigation application days in IOP 2 (Figure 4.8). In other words, in 2018, early growing season latent heat flux was partly influenced by precipitation while during the peak growing season was largely influenced by applications of irrigation. Overall, both IOP 1 and IOP 2 produced higher values of latent heat flux and lower values of sensible heat flux (Figure 4.7 and 4.8; Table 4.1 and 4.2). During IOP 1, irrigated LE averaged 14.62 W m^{-2} higher and H 7.24 W m^{-2} lower than non-irrigated LE and H, respectively. Comparable differences were observed but in greater magnitudes for IOP 2 where irrigated LE averaged 20.46 W m^{-2} higher and H 17.08 W m^{-2} lower than non-irrigated LE and H, respectively. These differences are observed in Figure 4.7, where LE dominated for fewer days and in smaller magnitude as compared to figure 4.8, representing IOP 1 and IOP 2 respectively. These differences provide a clear indication of the land-atmospheric interactions associated with irrigation.

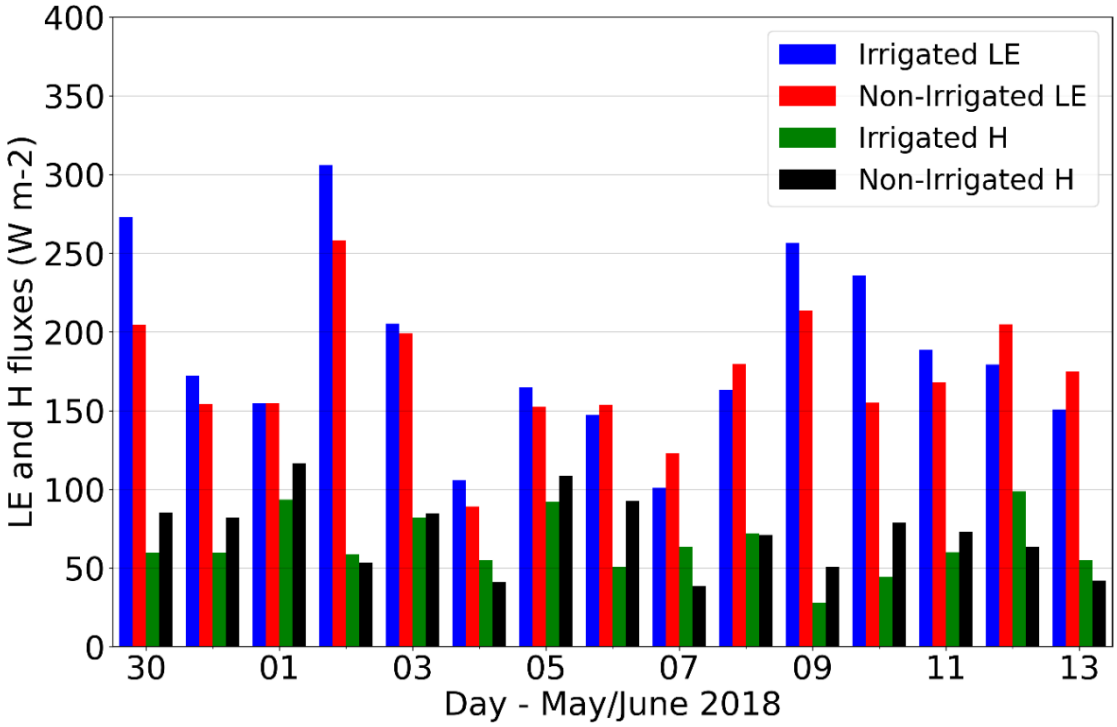

Figure 4.7: Daytime (11 UTC to 1 UTC) average latent (LE) and sensible (H) heat flux for irrigated and non-irrigated sites during IOP 1.

Table 4.1: Daytime (11 UTC to 1 UTC) average, minimum and maximum latent (LE) and sensible (H) heat flux for irrigated and non-irrigated sites during IOP 1. Observations correspond to Figure 4.7. Note: There is no statistical significance when comparing the irrigated and non-irrigated average daily values shown below (n=15), but statistical significance was found in an analysis of the irrigated and non-irrigated 30-minute daytime values (n=720) (Figure 4.4) used to calculate these averages.

IOP #1 – Irrigated vs. Non-Irrigated Full Day Average Latent (LE) and Sensible (H) Heat Flux			
	Date	LE (Wm^{-2})	H (Wm^{-2})
Irrigated	5/30/2018	273.21 (-0.47 to 789.29)	59.75 (-32.76 to 231.76)
	5/31/2018	172.41 (-7.39 to 666.05)	59.68 (-30.14 to 358.67)
	6/1/2018	154.63 (-94.34 to 450.49)	93.52 (-41.47 to 353.13)
	6/2/2018	306.07 (-1085.10 to 1932.87)	58.55 (-193.04 to 241.67)
	6/3/2018	205.39 (-20.61 to 739.04)	82.33 (-46.01 to 366.49)
	6/4/2018	105.80 (-388.99 to 1050.35)	55.11 (-37.12 to 362.01)
	6/5/2018	164.80 (-3.54 to 555.31)	92.27 (-29.03 to 341.51)
	6/6/2018	147.33 (-6.82 to 730.26)	50.97 (-45.84 to 279.69)
	6/7/2018	100.90 (-61.42 to 918.16)	63.65 (-65.68 to 324.19)
	6/8/2018	163.30 (-3.75 to 640.29)	71.97 (-31.88 to 275.61)
	6/9/2018	256.45 (-412.78 to 777.53)	28.18 (-108.88 to 161.94)
	6/10/2018	235.95 (-23.50 to 836.15)	44.32 (-92.82 to 408.86)
	6/11/2018	188.59 (-270.40 to 785.19)	60.16 (-76.43 to 258.42)
	6/12/2018	179.41 (-8.27 to 648.21)	98.76 (-30.02 to 372.42)
	6/13/2018	150.71 (-445.62 to 523.47)	55.10 (-84.94 to 243.97)
	Full IOP	187.00 (-1085.10 to 1932.87)	64.96 (-193.04 to 408.86)
Non-Irrigated	5/30/2018	204.75 (-5.05 to 1590.64)	85.28 (-38.60 to 463.97)
	5/31/2018	154.16 (-6.09 to 549.26)	82.28 (-36.01 to 416.04)
	6/1/2018	154.76 (-4.85 to 580.19)	116.54 (-60.80 to 432.52)
	6/2/2018	258.34 (-5.65 to 666.46)	53.48 (-50.93 to 225.77)
	6/3/2018	199.12 (0.00 to 611.40)	84.54 (-50.15 to 300.90)
	6/4/2018	89.28 (-67.63 to 551.80)	41.07 (-44.77 to 302.23)
	6/5/2018	152.33 (-4.10 to 587.16)	108.64 (-54.13 to 352.04)
	6/6/2018	153.80 (-7.85 to 618.57)	92.74 (-59.55 to 343.86)
	6/7/2018	123.10 (-4.60 to 573.24)	38.74 (-90.59 to 282.59)
	6/8/2018	179.67 (-16.98 to 697.00)	71.13 (-42.29 to 323.69)
	6/9/2018	213.69 (-1000.26 to 1417.62)	50.90 (-230.86 to 249.34)
	6/10/2018	155.09 (-71.45 to 580.83)	78.87 (-47.64 to 291.11)
	6/11/2018	167.95 (-1733.82 to 4399.97)	73.01 (-206.99 to 272.87)
	6/12/2018	204.92 (-4.18 to 710.14)	63.77 (-37.32 to 242.97)
	6/13/2018	174.77 (-2.07 to 598.25)	42.05 (-38.60 to 214.91)
	Full IOP	172.38 (-1733.82 to 4399.97)	72.20 (-230.86 to 463.97)

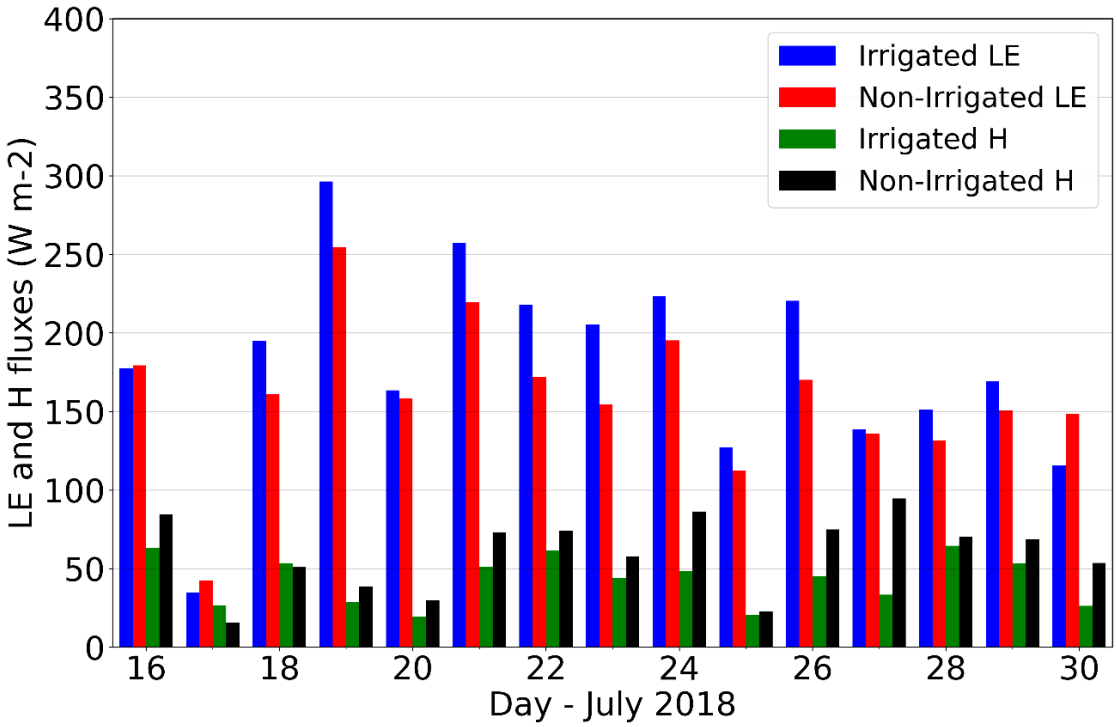

Figure 4.8: Daytime (11 UTC to 1 UTC) average latent (LE) and sensible (H) heat flux for irrigated and non-irrigated sites during IOP 2.

Table 4.2: Daytime (11 UTC to 1 UTC) average, minimum and maximum latent (LE) and sensible (H) heat flux for irrigated and non-irrigated sites during IOP 2. Observations correspond to Figure 4.8. Note: There is no statistical significance when comparing the irrigated and non-irrigated average daily values shown below (n=15), but statistical significance was found in an analysis of the irrigated and non-irrigated 30-minute daytime values (n=720) (Figure 4.5) used to calculate these averages.

IOP #2 – Irrigated vs. Non-Irrigated Full Day Average Latent (LE) and Sensible (H) Heat Flux			
	Date	LE (Wm^{-2})	H (Wm^{-2})
Irrigated	7/16/2018	177.55 (-35.41 to 697.76)	63.18 (-16.63 to 305.84)
	7/17/2018	34.74 (-10989.78 to 3766.80)	26.42 (-302.45 to 782.28)
	7/18/2018	195.00 (-61.97 to 692.44)	53.50 (-29.91 to 334.81)
	7/19/2018	296.34 (-347.80 to 1245.35)	28.87 (-38.43 to 146.82)
	7/20/2018	163.43 (-1701.73 to 1492.15)	19.40 (-45.85 to 187.09)
	7/21/2018	257.09 (-139.63 to 915.22)	51.23 (-22.75 to 196.64)
	7/22/2018	218.13 (-6.95 to 762.24)	61.49 (-41.78 to 300.28)
	7/23/2018	205.40 (-1255.08 to 1170.72)	44.14 (-58.62 to 233.64)
	7/24/2018	223.14 (-29.75 to 701.23)	48.53 (-31.10 to 213.88)
	7/25/2018	127.27 (-7534.63 to 3208.07)	20.53 (-183.52 to 360.77)
	7/26/2018	220.42 (-42.01 to 1013.06)	45.08 (-20.84 to 202.29)
	7/27/2018	138.86 (-2456.75 to 1003.63)	33.49 (-49.62 to 222.90)
	7/28/2018	151.32 (-21.80 to 711.34)	64.55 (-28.17 to 303.80)
	7/29/2018	169.08 (-140.50 to 690.88)	53.26 (-27.10 to 265.26)
	7/30/2018	115.70 (-4778.08 to 4612.56)	26.26 (-342.29 to 274.76)
	Full IOP	179.56 (-10989.78 to 4612.56)	42.66 (-342.29 to 782.28)
Non-Irrigated	7/16/2018	179.35 (-21.71 to 640.46)	84.41 (-18.77 to 478.07)
	7/17/2018	42.39 (-4120.22 to 4862.89)	15.73 (-344.01 to 203.10)
	7/18/2018	161.11 (-3.46 to 613.05)	50.91 (-27.76 to 241.02)
	7/19/2018	254.59 (-123.19 to 735.04)	38.65 (-42.13 to 193.02)
	7/20/2018	158.37 (-122.95 to 1379.05)	29.95 (-59.42 to 224.03)
	7/21/2018	219.71 (-11.38 to 697.65)	73.10 (-48.30 to 320.58)
	7/22/2018	171.93 (-2308.80 to 562.68)	74.11 (-27.26 to 330.89)
	7/23/2018	154.52 (-1797.76 to 709.47)	57.70 (-28.26 to 362.24)
	7/24/2018	195.29 (-8.90 to 586.92)	86.43 (-27.05 to 492.41)
	7/25/2018	112.56 (-858.80 to 1014.21)	22.79 (-152.13 to 248.79)
	7/26/2018	170.04 (-4.55 to 614.86)	74.96 (-24.08 to 504.25)
	7/27/2018	135.96 (-11.28 to 693.10)	94.64 (-17.71 to 501.33)
	7/28/2018	131.47 (-1299.99 to 1859.10)	70.47 (-120.64 to 357.70)
	7/29/2018	150.65 (-12.79 to 658.85)	68.65 (-37.22 to 483.22)
	7/30/2018	148.51 (-4374.50 to 2581.72)	53.63 (-204.28 to 253.17)
	Full IOP	159.10 (-4374.50 to 4862.89)	59.74 (-344.01 to 504.25)

4.3 Equivalent Temperature (T_E)

A comparison of IOP 1 (Fig. 4.9; Table 4.3) and IOP 2 (Fig. 4.10; Table 4.4) T_E for irrigated and non-irrigated areas shows values similar to the summer season average calculated by Younger et al. (2018) for western Kentucky. In other words, T_E values over southeastern Nebraska were as high as the more moist east-central US. Differences in irrigated and non-irrigated T_E during IOP 1 were smaller in the early growing season. Limited irrigation applications played a role in these small differences (Table 4.3). As we progress through the growing season, and pass a key transitional point in early July from less irrigation to consistently higher irrigation applications over irrigated sites (sites 1 through 6), a more clear increase in T_E was observed (Figure 4.9). Irrigated site averages were noticeably higher during IOP 2 with the exception of 16 July, when a precipitation event occurred over much of the study area. Younger et al. (2018) found an average ~60 °C T_E during the summer months in Kentucky. On average, T_E values over irrigated areas in eastern Nebraska was 62 °C during IOP 2 (Table 4.4). In other words, due to irrigation, T_E in eastern Nebraska was as high as in the east-central United States during similar time periods. The range of T_E observed during IOP 1 was also greater than that observed during IOP 2 (Approximately 4° C greater) due to larger, day-to-day fluctuations in springtime air temperatures as compared to observed, mid-summer air temperatures. Table 4.3 and 4.4 provide daily T_E averages and ranges for irrigated and non-irrigated sites during IOP 1 and IOP 2 respectively.

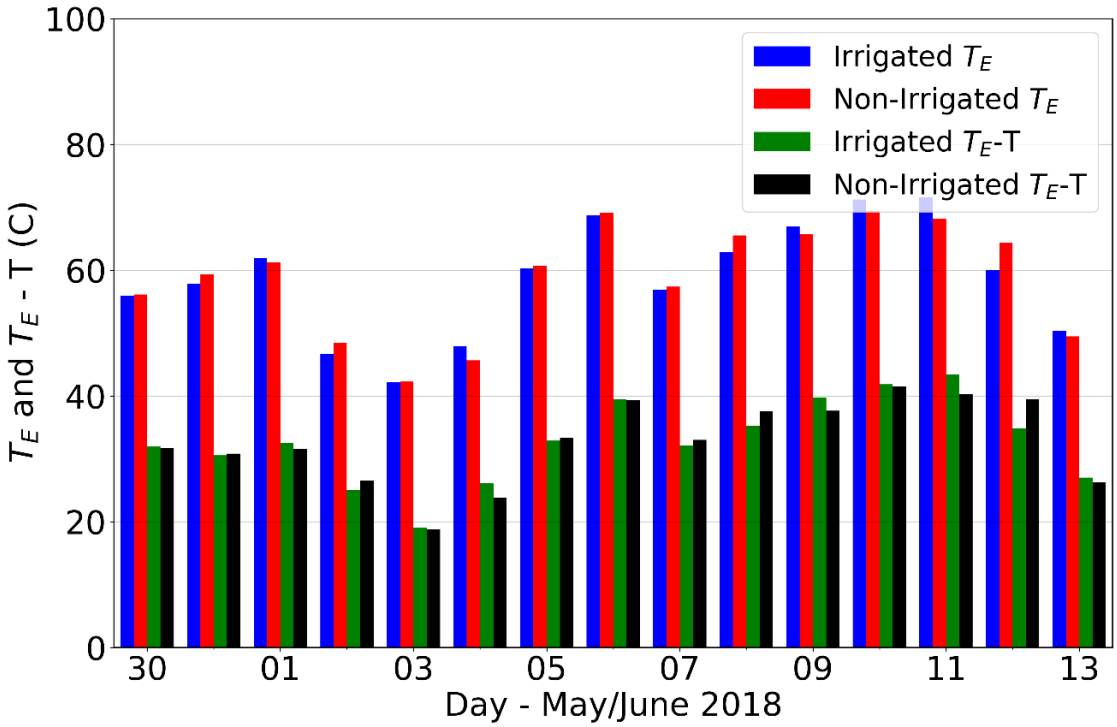

Figure 4.9: Daytime (11 UTC to 1 UTC) average equivalent temperature (T_E) for irrigated and non-irrigated sites during IOP 1.

Table 4.3: Daytime (11 UTC to 1 UTC) average, minimum and maximum equivalent temperature (T_E) for irrigated and non-irrigated sites during IOP 1. Values correspond to Figure 4.9. Note: There is no statistical significance when comparing the irrigated and non-irrigated average daily values shown below (n=15), but statistical significance was found in an analysis of the irrigated and non-irrigated 30-minute daytime values (n=720) used to calculate these averages.

IOP #1 – Irrigated vs. Non-Irrigated Full Day Average Equivalent Temperature (T_E) and Equivalent Temperature/Temperature Difference (T_E – T)			
	Date	T_E (°C)	T_E - T (°C)
Irrigated	5/30/2018	55.95 (42.63 to 62.20)	31.92 (27.16 to 36.05)
	5/31/2018	57.87 (44.28 to 64.40)	30.56 (23.15 to 36.48)
	6/1/2018	61.94 (45.76 to 70.54)	32.55 (24.74 to 40.23)
	6/2/2018	46.70 (42.75 to 53.93)	25.06 (18.86 to 33.04)
	6/3/2018	42.24 (31.34 to 48.94)	19.07 (15.39 to 23.61)
	6/4/2018	47.96 (37.36 to 55.83)	26.14 (20.44 to 32.60)
	6/5/2018	60.32 (39.20 to 68.95)	32.90 (25.06 to 39.11)
	6/6/2018	68.75 (51.20 to 76.97)	39.47 (30.23 to 47.71)
	6/7/2018	56.86 (47.45 to 63.97)	32.14 (26.85 to 36.28)
	6/8/2018	62.92 (46.46 to 68.89)	35.27 (29.78 to 38.77)
	6/9/2018	66.98 (48.06 to 78.21)	39.73 (29.20 to 47.82)
	6/10/2018	71.22 (58.66 to 85.14)	41.86 (32.68 to 51.10)
	6/11/2018	71.55 (59.89 to 79.26)	43.39 (36.12 to 48.25)
	6/12/2018	60.03 (46.52 to 68.93)	34.87 (28.12 to 41.13)
	6/13/2018	50.39 (33.27 to 56.97)	27.02 (21.17 to 31.47)
	Full IOP	58.78 (31.34 to 85.14)	32.80 (15.39 to 51.10)
Non-Irrigated	5/30/2018	56.12 (43.96 to 62.31)	31.71 (28.00 to 36.34)
	5/31/2018	59.34 (46.24 to 66.50)	30.81 (23.28 to 37.52)
	6/1/2018	61.27 (49.09 to 68.73)	31.55 (23.13 to 39.36)
	6/2/2018	48.46 (0.00 to 58.71)	26.51 (0.00 to 35.11)
	6/3/2018	42.27 (0.00 to 47.11)	18.81 (0.00 to 22.10)
	6/4/2018	45.68 (34.88 to 52.33)	23.77 (18.02 to 29.08)
	6/5/2018	60.73 (40.43 to 68.32)	33.32 (25.29 to 38.51)
	6/6/2018	69.11 (56.63 to 77.81)	39.32 (32.87 to 46.85)
	6/7/2018	57.36 (47.59 to 65.06)	33.02 (26.17 to 39.01)
	6/8/2018	65.52 (52.19 to 74.32)	37.55 (32.72 to 44.21)
	6/9/2018	65.71 (47.76 to 81.57)	37.66 (25.26 to 51.61)
	6/10/2018	69.45 (57.16 to 78.89)	41.55 (36.30 to 46.90)
	6/11/2018	68.19 (51.51 to 84.40)	40.25 (29.42 to 50.28)
	6/12/2018	64.32 (50.33 to 72.94)	39.45 (29.06 to 45.36)
	6/13/2018	49.47 (39.90 to 55.78)	26.25 (19.25 to 31.85)
	Full IOP	58.87 (0.00 to 84.40)	32.77 (0.00 to 51.61)

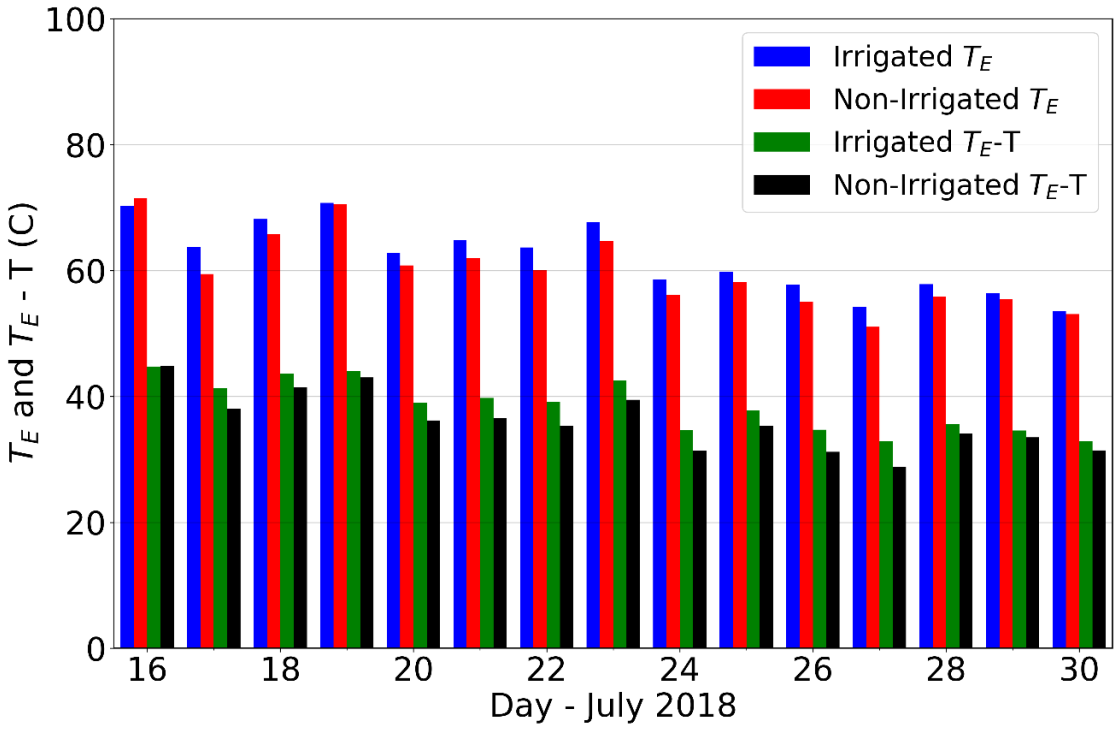

Figure 4.10: Daytime (11 UTC to 1 UTC) average equivalent temperature (T_E) for irrigated and non-irrigated sites during IOP 2.

Table 4.4: Daytime (11 UTC to 1 UTC) average, minimum and maximum equivalent temperature (T_E) for irrigated and non-irrigated sites during IOP 2. Values correspond to Figure 4.10. Note: There is no statistical significance when comparing the irrigated and non-irrigated average daily values shown below (n=15), but statistical significance was found in an analysis of the irrigated and non-irrigated 30-minute daytime values (n=720) used to calculate these averages.

IOP #2 – Irrigated vs. Non-Irrigated Full Day Average Equivalent Temperature (T_E) and Equivalent Temperature/Temperature Difference (T_E – T)			
	Date	T_E (°C)	T_E - T (°C)
Irrigated	7/16/2018	70.27 (51.08 to 85.08)	44.78 (33.06 to 55.33)
	7/17/2018	63.69 (53.28 to 72.98)	41.31 (33.72 to 47.10)
	7/18/2018	68.18 (54.10 to 78.98)	43.62 (35.40 to 50.83)
	7/19/2018	70.73 (51.93 to 80.94)	44.04 (33.84 to 53.07)
	7/20/2018	62.85 (44.29 to 74.11)	38.99 (28.60 to 47.85)
	7/21/2018	64.85 (44.40 to 76.63)	39.75 (28.79 to 47.90)
	7/22/2018	63.66 (48.48 to 72.74)	39.14 (31.32 to 45.29)
	7/23/2018	67.66 (53.20 to 79.19)	42.58 (34.45 to 50.42)
	7/24/2018	58.55 (34.32 to 70.09)	34.64 (22.38 to 44.35)
	7/25/2018	59.80 (42.53 to 74.42)	37.82 (27.52 to 47.13)
	7/26/2018	57.73 (40.06 to 79.13)	34.71 (25.95 to 55.18)
	7/27/2018	54.20 (37.77 to 63.71)	32.88 (24.65 to 39.08)
	7/28/2018	57.82 (45.10 to 67.97)	35.56 (29.17 to 41.56)
	7/29/2018	56.38 (46.43 to 65.71)	34.58 (30.05 to 40.45)
	7/30/2018	53.58 (41.22 to 61.94)	32.86 (25.53 to 38.95)
	Full IOP	62.00 (34.32 to 85.08)	38.48 (22.38 to 55.33)
Non-Irrigated	7/16/2018	71.46 (55.86 to 80.44)	44.82 (36.20 to 49.66)
	7/17/2018	59.43 (52.36 to 68.51)	38.08 (33.97 to 43.28)
	7/18/2018	65.78 (51.31 to 80.24)	41.41 (33.46 to 47.30)
	7/19/2018	70.57 (57.05 to 80.31)	43.02 (29.00 to 50.86)
	7/20/2018	60.82 (45.65 to 70.41)	36.19 (26.58 to 43.56)
	7/21/2018	61.95 (49.58 to 69.76)	36.52 (31.91 to 41.60)
	7/22/2018	60.11 (46.68 to 67.26)	35.37 (29.77 to 39.00)
	7/23/2018	64.67 (54.69 to 73.97)	39.46 (32.55 to 45.61)
	7/24/2018	56.14 (40.32 to 63.98)	31.42 (26.12 to 37.19)
	7/25/2018	58.17 (41.31 to 70.49)	35.27 (26.70 to 42.95)
	7/26/2018	55.01 (44.46 to 62.57)	31.19 (24.19 to 37.14)
	7/27/2018	51.04 (35.02 to 62.08)	28.82 (22.73 to 35.85)
	7/28/2018	55.85 (46.80 to 63.72)	34.11 (30.36 to 38.29)
	7/29/2018	55.46 (44.15 to 62.34)	33.49 (28.44 to 37.93)
	7/30/2018	53.07 (0.00 to 59.67)	31.44 (0.00 to 37.63)
	Full IOP	59.97 (0.00 to 80.44)	36.04 (0.00 to 50.86)

4.4 Root Zone Soil Moisture

Using the Wang et. al. (2017) Exponential Filter Model, the 5-cm soil moisture data from the ISFS sites were used to create modelled soil moisture for 25 and 50 cm depths. Additionally, the T_{opt} parameter, which was calculated based on surface soil characteristics, was a key input for the Exponential Filter Model. Since soil cores were not available during data analysis for this thesis, alternative data were used for calculating T_{opt}. Additional calculations for verification of accuracy were not conducted. A root zone moisture profile of the soils in the irrigated and non-irrigated sites provided insight as to the rate at which moisture was able to percolate through the soil and the depths impacted by precipitation and irrigation events at the surface. The results from each of the ISFS sites are shown in Figure 4.11.

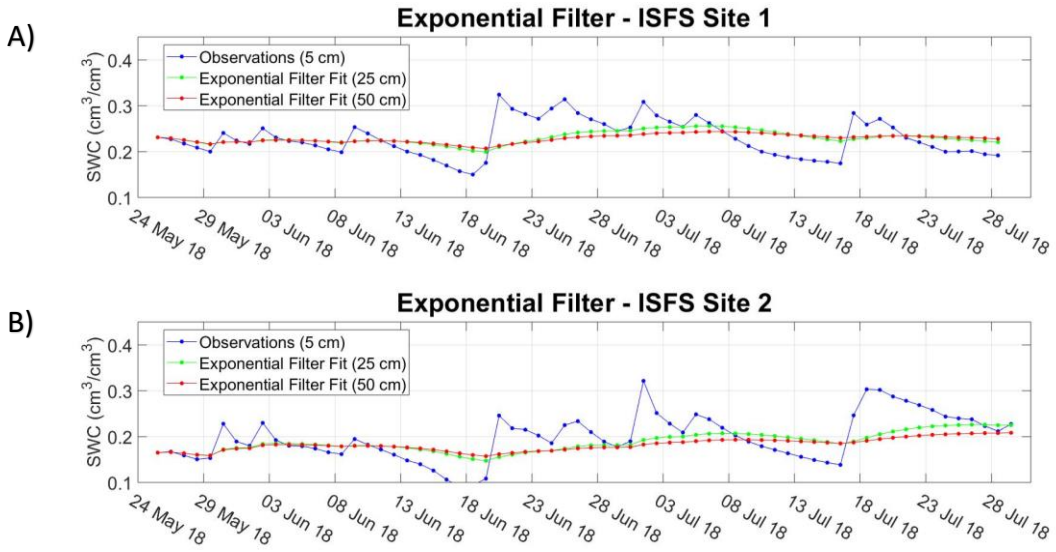

C)

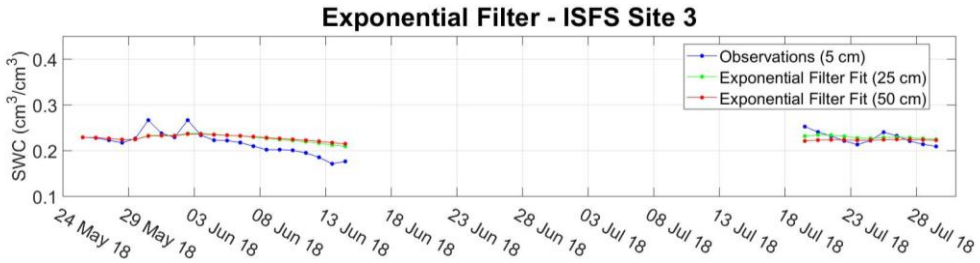
Exponential Filter - ISFS Site 3
Observations (5 cm)
Exponential Filter Fit (25 cm)
Exponential Filter Fit (50 cm)
SWC (cm3/cm3)
0.1
0.2
0.3
0.4
24 May 18
29 May 18
03 Jun 18
08 Jun 18
13 Jun 18
18 Jun 18
23 Jun 18
28 Jun 18
03 Jul 18
08 Jul 18
13 Jul 18
18 Jul 18
23 Jul 18
28 Jul 18

D)

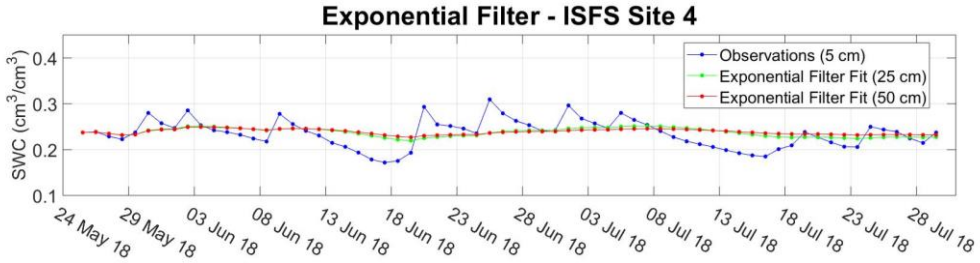
Exponential Filter - ISFS Site 4
Observations (5 cm)
Exponential Filter Fit (25 cm)
Exponential Filter Fit (50 cm)
SWC (cm3/cm3)
0.1
0.2
0.3
0.4
24 May 18
29 May 18
03 Jun 18
08 Jun 18
13 Jun 18
18 Jun 18
23 Jun 18
28 Jun 18
03 Jul 18
08 Jul 18
13 Jul 18
18 Jul 18
23 Jul 18
28 Jul 18

E)

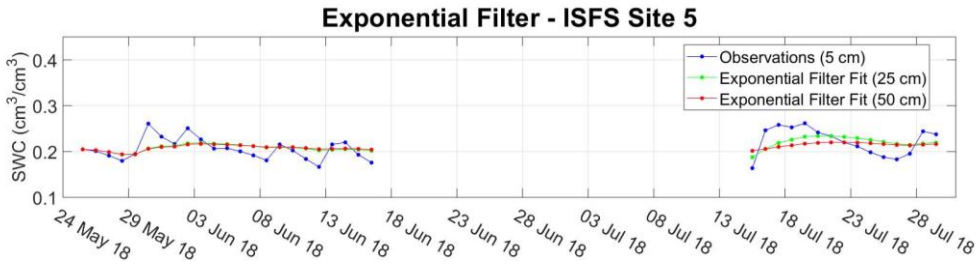
Exponential Filter - ISFS Site 5
Observations (5 cm)
Exponential Filter Fit (25 cm)
Exponential Filter Fit (50 cm)
SWC (cm3/cm3)
0.1
0.2
0.3
0.4
24 May 18
29 May 18
03 Jun 18
08 Jun 18
13 Jun 18
18 Jun 18
23 Jun 18
28 Jun 18
03 Jul 18
08 Jul 18
13 Jul 18
18 Jul 18
23 Jul 18
28 Jul 18

F)

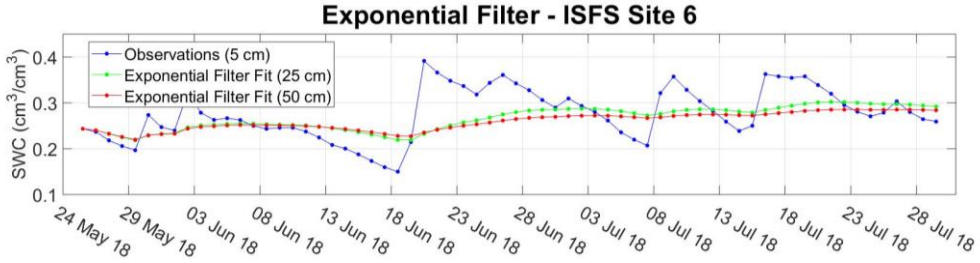
Exponential Filter - ISFS Site 6
Observations (5 cm)
Exponential Filter Fit (25 cm)
Exponential Filter Fit (50 cm)
SWC (cm3/cm3)
0.1
0.2
0.3
0.4
24 May 18
29 May 18
03 Jun 18
08 Jun 18
13 Jun 18
18 Jun 18
23 Jun 18
28 Jun 18
03 Jul 18
08 Jul 18
13 Jul 18
18 Jul 18
23 Jul 18
28 Jul 18

G)

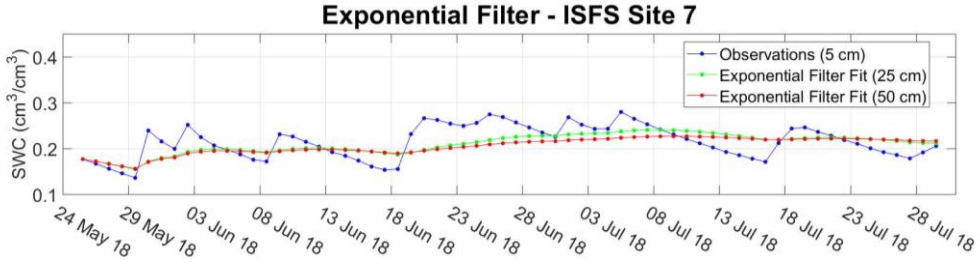
Exponential Filter - ISFS Site 7
Observations (5 cm)
Exponential Filter Fit (25 cm)
Exponential Filter Fit (50 cm)
SWC (cm3/cm3)
0.1
0.2
0.3
0.4
24 May 18
29 May 18
03 Jun 18
08 Jun 18
13 Jun 18
18 Jun 18
23 Jun 18
28 Jun 18
03 Jul 18
08 Jul 18
13 Jul 18
18 Jul 18
23 Jul 18
28 Jul 18

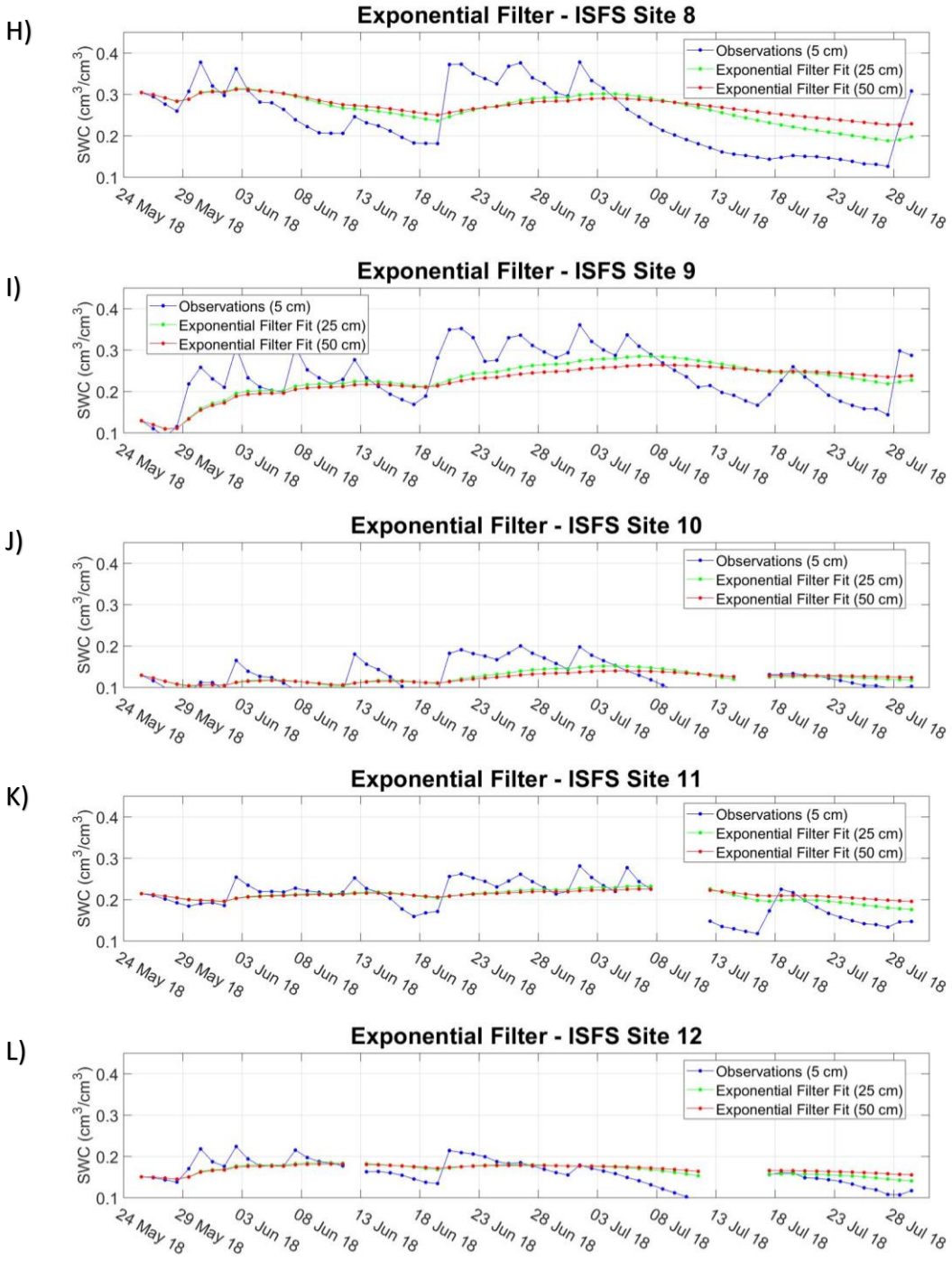

Figure 4.11: Modelled soil water content for the ISFS sites 1-12 (A through L respectively).

From the modeled data, it was observed that soil water content (SWC) for both irrigated and non-irrigated sites in the early part of the growing season (IOP 1) were

comparable across eleven of the twelve sites with the exception of site 10, a non-irrigated site that exhibited significantly lower SWC likely attributed to sloped topography and increased runoff rates. Rapid increases in SWC were observed throughout the first half of the growing season in connection with reported precipitation events. For precipitation events that exhibited heavy rain rates over a short window of time, little to no fluctuations were observed in the modelled 25 and 50-cm SWC. On the other hand, slower precipitation spanning over longer time-windows showed gradual increases in both the 25 and 50-cm modelled SWC. This confirms the model's capability to handle different precipitation rates and amounts. Moreover, responses in the 25-cm modelled SWC were more common than those at 50-cm.

In the second half of the growing season (IOP 2), contrasts between the irrigated and non-irrigated sites became more noticeable. Declines in SWC for the non-irrigated sites (7-12) were observed in the 5-cm data and modelled 25 and 50-cm data. Due to the increased need for water by the crops, significant drawdowns in SWC at all depths started in early July and progressed through the end of IOP 2. Data from ISFS site 8 (Fig. 4.11 H) depicts this dramatic transition and illustrates a reversal in the order of SWC by depth (i.e. 50-cm SWC is greater than 5-cm SWC for an extended period). All irrigated sites during IOP 2 observed an increase or plateauing of SWC, indicating that the additional water applied through irrigation was steadily infiltrating through the soil profile and allowing SWC to increase or remain unchanged during the time period when water extraction by plants was greatest.

Another key factor impacting soil water retention, runoff and infiltration rates was the difference in soil type at the irrigated and non-irrigated sites. As shown in Table 4.5, the soils at the non-irrigated locations east of the Big Blue River (primarily hydrologic class D) have higher clay percentages than the hydrologic class C, irrigated soils west of the Big Blue River. Due to these differences in characteristics, T_{opt} also shows variability between the irrigated and non-irrigated sites. In conclusion, the soils present in the south eastern portion of Nebraska are similar, but the slight characteristic differences influence factors that cannot be neglected.

Table 4.5: Soil characteristics of ISFS sites 1-12 including calculated T_{opt} for 25 and 50 cm depths. Columns with two values represent sites covering multiple map units in the web soil survey.

Site	Soil Type	Clay %	Sand %	Silt %	T_opt_25	T_opt_50
1	Hastings Silt Loam	28.7	8.7	62.6	13.4577	42.0338
2	Hastings Silt Loam	28.7	8.7	62.6	13.4577	42.0338
3	Butler Silt Loam	33.2	5.1	61.7	14.8883	48.0944
4	Butler Silt Loam/Crete Silt Loam	33.2 34.7	5.1 14.4	61.7 50.9	14.8883 15.3306	48.0944 50.1183
5	Hastings Silty Clay Loam	29.7	8.4	61.9	13.7891	43.3792
6	Crete Silt Loam	32.3	5.4	62.3	14.6147	46.8809
7	Yutan Silty Clay Loam	27.8	13.2	59	13.1528	40.8238
8	Wymore Silty Clay Loam/Pawnee Clay Loam	36.6 36.9	2.2 27.5	61.2 35.6	15.8658 15.9478	52.6847 53.0901
9	Wymore Silty Clay Loam	37	2.2	60.8	15.975	53.2253
10	Wymore Silty Clay	37.1	2.1	60.8	16.0021	53.3605
11	Wymore Silty Clay Loam	36.8	2.2	61	15.9206	52.955
12	Wymore Silty Clay Loam/Wymore Silty Clay	37	2.2	60.8	15.975	53.2253

4.5 PBL, LCL and LFC Variations

To determine variations in PBL, LCL, and LFC heights, radiosonde data from the DOW and ISS sites were analyzed. Average PBL heights were calculated for irrigated and non-irrigated areas for IOP 1 and 2 using data from all radiosonde launches. The data were then plotted with respect to the deployment hours (Figure 4.12). As shown previously, ISS 2 and 3 sites were over non-irrigated and irrigated land uses, respectively. DOW 8 was located in an irrigated area and DOW 6 and 7 along the boundary of non-irrigated and irrigated areas (see Figure 1.1). Results from these radiosonde data analyses (Fig. 4.12) indicate that boundary layer heights during the early part of the growing season (IOP 1) were higher over both irrigated, transitional and non-irrigated environments as compared to the late growing season (IOP 2). Considering the weather-wise more active IOP 1 and larger values of sensible heat flux (increased surface turbulence), a deeper PBL during this time was expected. In addition, compared to non-irrigated locations, the PBL heights over irrigated areas were lower during IOP 2.

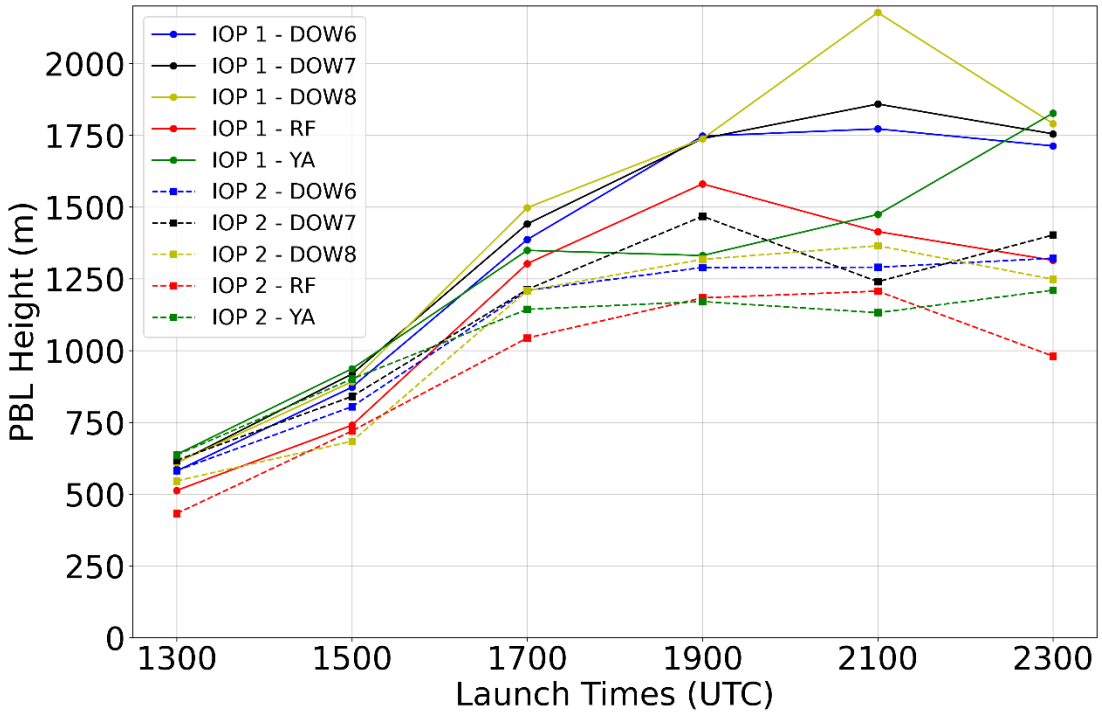

Figure 4.12: Full IOP average PBL Heights for the DOW sites (6, 7, 8), Rogers Farm (ISS site; RF) and York Airport (ISS site; YA) at the respective radiosonde launch times. Corresponding values are in the Appendix (Table A.6 and A.7).

At the apex of the growing season, when surface temperatures and latent heat flux are higher and sensible heat flux lower, PBL and LCL heights are expected to be lower over both irrigated and non-irrigated areas. Results from IOP 2 (Fig. 4.12) demonstrate these expectations with shifts in PBL development time (i.e. earlier in the day) associated with less convective activity and quicker stabilization of the near surface layer. The soundings from the DOW sites used for this analysis can be found in the following section highlighting specific events during both IOP 1 and 2. Note, that the difference of heights between LFC and LCL can be used to determine potential for convective development. Analysis of LFC height data and their linkages to land use land

cover is currently ongoing and not included in the discussions. However, they are (LFC heights) included in selected tables below for further ease in understanding of lower tropospheric developments.

4.6 Interesting Dates During IOP 1

The interesting dates for IOP 1 (and IOP 2) were chosen based on the potential for L-A interactions or presence of convective activity disrupting expected energy exchanges and meteorological conditions. IOP 1 focused on early growing season interactions when irrigation applications were less compared to peak growing season. Dates chosen for IOP 1 include 3 June, when conditions were favorable for land-atmospheric interactions and 9 June, when convective activity impacted the entire GRAINEX study area. Data used for analysis of the selected dates (for both IOP 1 and 2) include air and dew point temperatures, specific humidity, energy fluxes (specifically latent and sensible heat) averages over irrigated and non-irrigated sites, equivalent temperatures, surface soil moisture data, modeled root zone moisture profiles, and radiosonde profiles from the DOW sites.

4.6.1. 3 June

On 3 June, the GRAINEX study region was dominated by high pressure and as a result, fair weather and clear skies were observed. A three day stretch of cooler air temperatures was observed around 3 June, which reflected the climatological normals

as compared to the weeks preceding and following 3 June (Fig. 4.1) where 3 °C to 6 °C temperature departures were observed (illustrated in the June 2018 – National Climate Report - https://www.ncdc.noaa.gov/sotc/national/201806). It can be noted based on Figure 4.13, latent and sensible heat fluxes were very similar over both irrigated and non-irrigated areas since both were subject to similar meteorological conditions and potentially limited moisture associated with irrigation (early growing season).

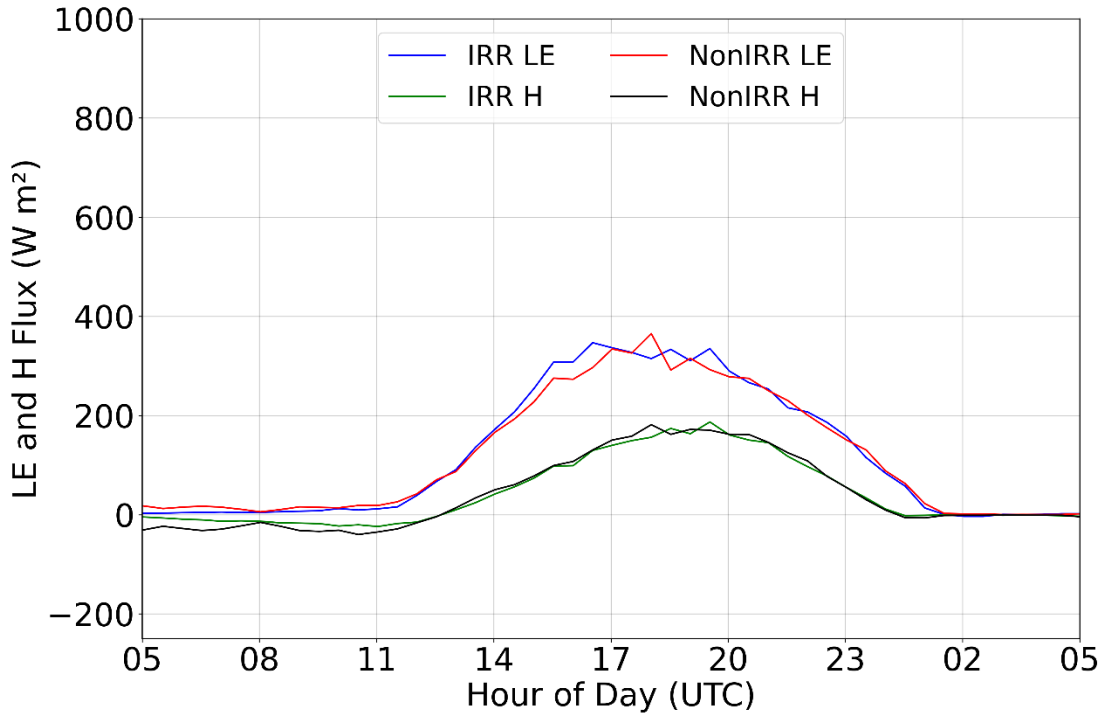

Figure 4.13: 30-minute averaged latent (LE) and sensible (H) heat flux for irrigated and non-irrigated sites on 3 June.

The difference of equivalent temperatures between irrigated and non-irrigated areas were small (Fig. 4.9). The soil moisture model (Fig. 4.11) indicated that 3 June was the initiation date for a stretch of drying for both irrigated and non-irrigated sites until precipitation on 9 June (which is the secondary date of interest analyzed during IOP 1).

The DOW soundings of 3 June (Fig. 4.14) suggest a significantly dry layer between 800 and 750 hPa (2200 to 3200 meters above MSL) was the upper limit of the boundary layer's development at both the DOW and ISS radiosonde sites. PBL and LCL heights for all launches on 3 June can be found in Table 4.6. Notably, 3 June had the highest average PBL heights compared to all other dates from IOP 1.

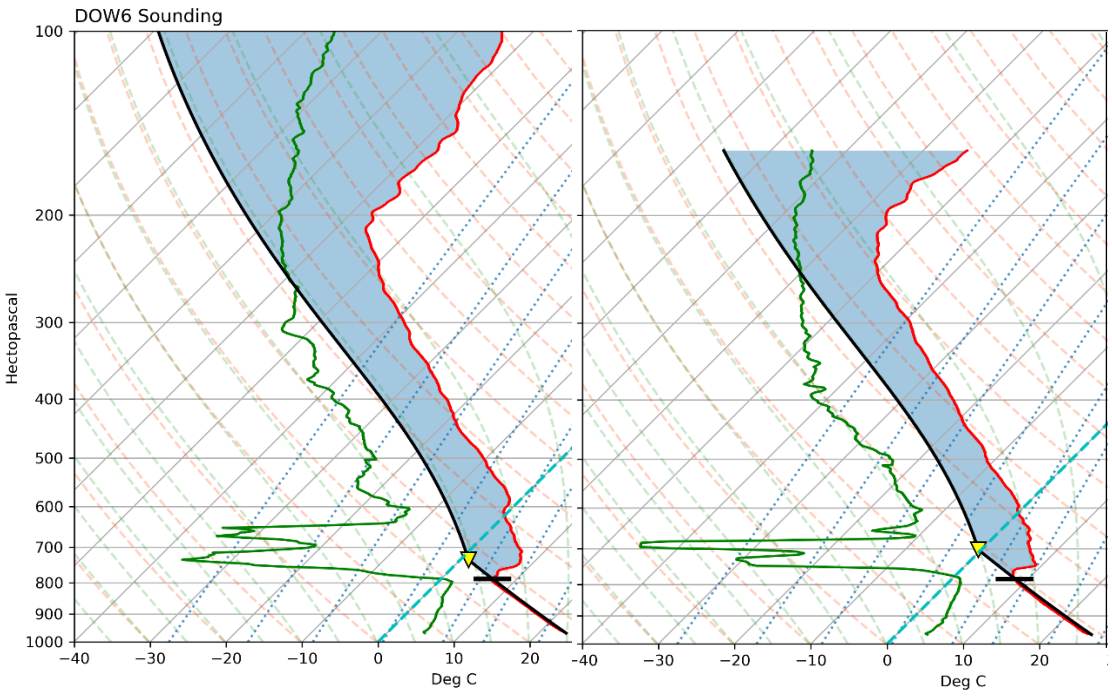

Figure 4.14: Soundings from the 1700 (left) and 2100 (right) UTC (12:00 and 4:00 p.m. LT) launches on 3 June at the DOW 6 location (exact site coordinates found in Table 3.5).

From the observations in Table 4.6, it is found that fair weather conditions were favorable for observing relatively high PBL heights. Since 3 June was during IOP 1, it is reasonably assumed that smaller amounts of irrigation were occurring and the differences observed in PBL heights at the five locations throughout the day were most likely associated with the land use type hindering or assisting daytime mixing and thus

slowing or speeding up the development of the PBL. An example of this difference can be observed during 1700 UTC (12:00 p.m. LT) when the radiosonde from the York Airport (ISS 3) experienced a lower PBL than the other four sites, but by the 2100 UTC (4:00 p.m. LT) launch comparable PBL heights were observed at all five locations. This suggests slower development of the PBL over irrigated areas.

Table 4.6: PBL and LCL heights (in meters above MSL) from DOW 6, 7, 8, Rogers Farm and York Airport radiosonde launches on 3 June.

		1100	1300	1500	1700	1900	2100	2300	0100
DOW 6	PBL				2211	2168	2254	2320	549
	LCL	1161		2257	2794	3127	3154	3241	3161
	LFC								
DOW 7	PBL		556	976	2562		2496	2314	2118
	LCL	1030	1656	2324	2697	2948	3178	3340	2920
	LFC								
DOW 8	PBL			814	2423	2323		2297	
	LCL	917	1308	2094	2773	3079	3238	3251	3101
	LFC								
Rogers Farm	PBL				2474	2445	2391		
	LCL	1100	1387	2162	2723	2788	2880	2492	1967
	LFC								
York Airport	PBL		574		1899		2378	2397	
	LCL	858	1256	1911	2643	2826	2820	3027	2615
	LFC								

4.6.2. 9 June

This day (9 June) experienced significant convective activity in the form of an afternoon mesoscale convective system (8 June) forming in southern South Dakota and central Nebraska and propagating east. Impacts to the GRAINEX study area were observed in the early morning hours (9 June) and included damaging winds and heavy rain. A southerly low-level jet provided a rich source of moisture and large buoyancy,

which gave this system its convective potential. Larger differences between irrigated and non-irrigated site averages were observed on 9 June (approximately 3° C) with air temperatures over the irrigated region being higher than the non-irrigated site air temperatures (Fig. 4.1 and Fig. 4.2). This difference is likely associated with the west to east propagation of the storm and the delayed early morning heating of the eastern sites (non-irrigated) due to residual cloud cover. Irrigated latent and sensible heat flux were responsive to this differential heating and therefore higher and lower respectively. (Fig. 4.15).

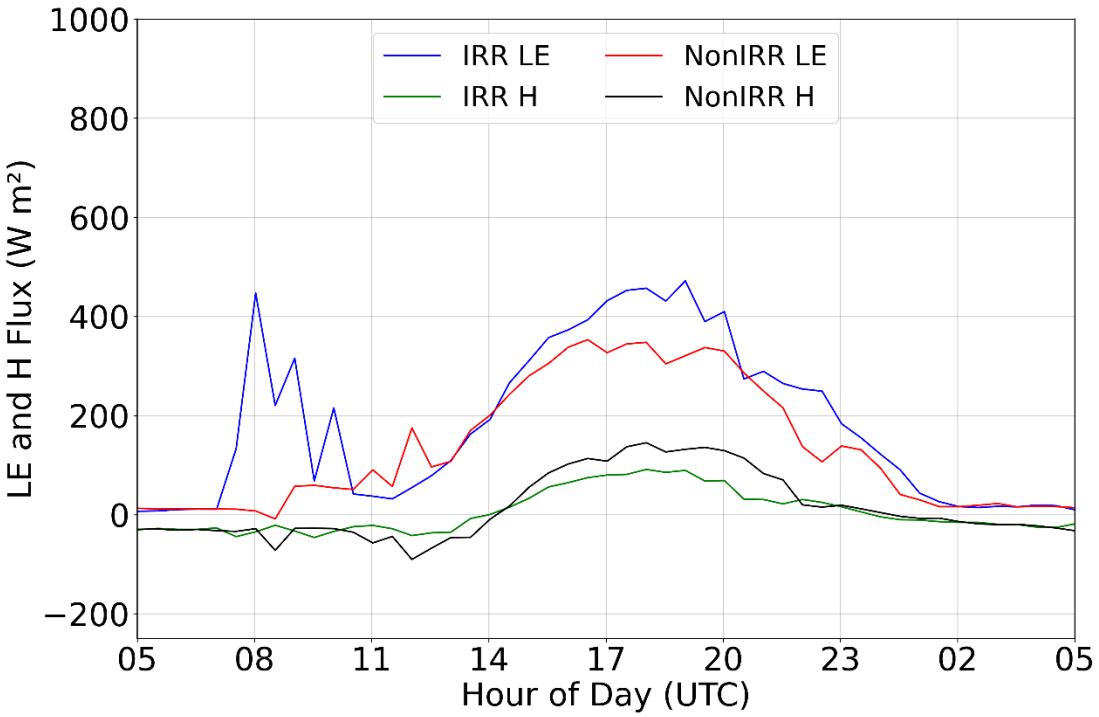

Figure 4.15: 30-minute averaged latent (LE) and sensible (H) heat flux for irrigated and non-irrigated sites on 9 June.

As discussed previously, on 8-9 June precipitation ended a period of drawdown in soil moisture with some sites experiencing much greater precipitation totals then

others (Fig. 4.11). Lastly, the DOW sounding data from this event did not capture the storm passage due to the timing of the launches but they do reflect the early morning cloud cover and additional surface moisture that impeded PBL growth (Fig. 4.16). The heights of the PBL and LCL were notably lower than those on 3 June and can be found in Table 4.6.

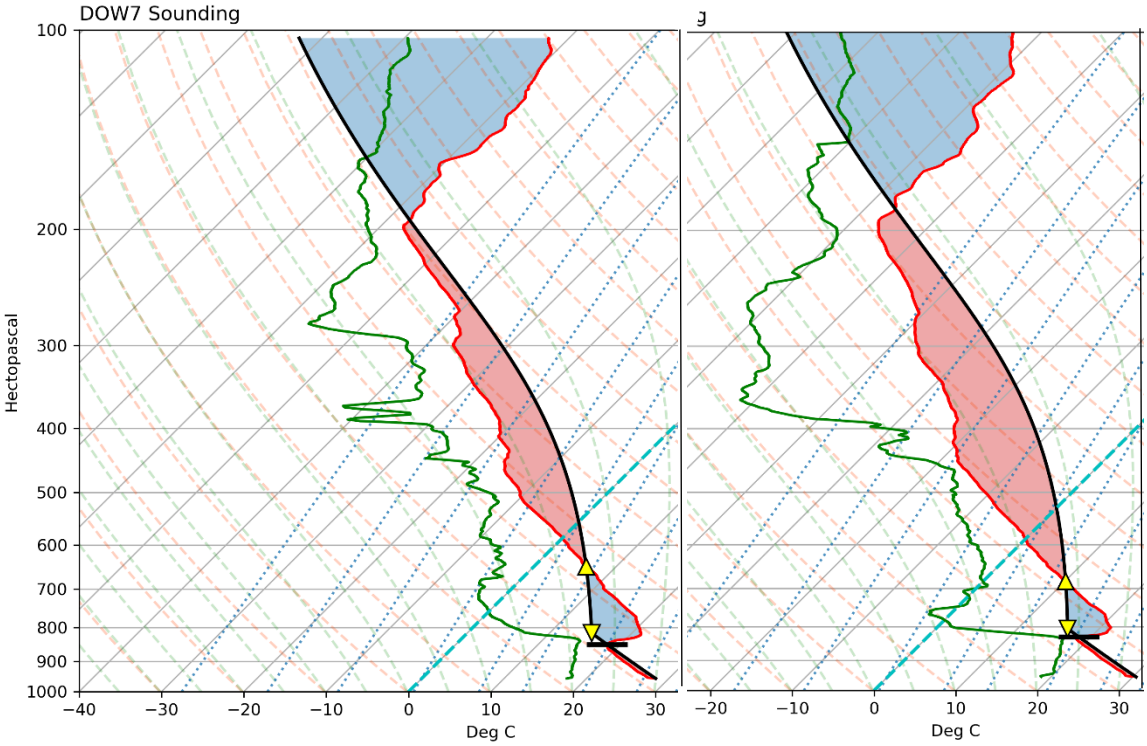

Figure 4.16: Figure 4.16: Soundings from the 1700 (left) and 2100 (right) UTC (12:00 and 4:00 p.m. LT) launches on 9 June at the DOW 7 location (exact site coordinates found in Table 3.5).

Since the 9 June precipitation event occurred during the morning hours outside of the launch window of the radiosondes, no rapid increase in PBL heights were observed (via Table 4.7) and by the 1100 UTC (6:00 a.m. LT) launch, any development that had occurred associated with the early morning convection had diminished. It is

evident from Table 4.7 that there was a tendency of lower PBL and LCL heights over irrigated areas compared to non-irrigated areas during the peak PBL growth period (mid to early afternoon). For example, over the irrigated York Airport area, PBL and LCL heights at 1900 UTC (2:00 p. m. LT) were 1416 and 1649 m, respectively (Table 4.7). At the same time, PBL and LCL heights were 1496 and 1723 m, respectively over Rogers Farm (Table 4.7). In addition, compared to 3 June (Table 4.6), PBL development occurred much slower on 9 June and lowering of the PBL occurred early in the afternoon. LCL heights also remained low associated with near surface instability and higher moisture content within the PBL.

Table 4.7: PBL and LCL heights (in meters above MSL) from DOW 6, 7, 8, Rogers Farm and York Airport radiosonde launches on 9 June.

		1100	1300	1500	1700	1900	2100	2300	0100
DOW 6	PBL				1327	1481	1858	946	514
	LCL	1387	1362	1965	1851	1827	1949	1727	1643
	LFC		6251	4843	3910	3622	3471	3183	3066
DOW 7	PBL			737	1526	1576	1722		640
	LCL	565	1536	1753	1869	1806	1973	1710	1703
	LFC	5486	5059	4126	3822	3305	3375	3141	3194
DOW 8	PBL			758	1568	1428	1710	1077	536
	LCL	618	1034	1539	1785	1840	1965	1703	1655
	LFC	4962	4747	3820	3625	3492	3498	3126	3035
Rogers Farm	PBL			462	1082	1496			
	LCL		1043	1857	1471	1723	1875	1465	1244
	LFC		5207	4304	3590	3417	3279	2763	2714
York Airport	PBL		552	822		1416	1762		
	LCL		1133	1486	1520	1649	1899	1735	1482
	LFC		4560	3965	3329	3074	3171	2888	2405

4.7 Interesting Dates During IOP 2

Similar to IOP 1, IOP 2 consisted of cooler and drier periods interspersed by sporadic rain events. The number of precipitation events were notably less during the second half of the growing season (including the IOP 2 window) resulting in increased irrigation at ISFS sites 1 through 6. Since IOP 2 targeted the peak growing season, four dates were chosen for analysis as compared to the two discussed for IOP 1. These dates include 19 July which exhibited an early morning severe weather event with heavy precipitation simultaneously impacting irrigated and non-irrigated portions of the GRAINEX study area starting around 0600 UTC (1:00 a.m. Local Time) and 22, 23, and 24 July which included a day of widespread precipitation (23 July) bookended by two days of strong L-A interactions (22 and 24 July).

4.7.1 19 July

In the early morning hours of 19 July, a multicellular convective complex originating from a closed upper-level low in western South Dakota moved southeast across Nebraska and into parts of Iowa, Missouri, and Kansas. A moist and unstable downstream air mass fueled the growth and progression of this system. The initial cold front passage produced super cells in the late evening of 18 July, which remained west of the study area, but associated stratiform precipitation extended over the irrigated sites. The secondary boundary, which produced the complex that impacted the

GRAINEX area the morning of 19 July, formed multiple cells, of which, the most severe were located west of the Big Blue River where irrigation was actively occurring.

Prior to the precipitation event, higher air temperatures were observed over irrigated areas. Following the precipitation event, higher air temperatures were observed over non-irrigated areas and conversely lower dew point temperatures and specific humidity (Fig. 4.1, 4.2 and 4.3). Alternatively, lower air temperatures and higher dew point temperatures and specific humidity were observed over irrigated areas (Fig. 4.1. 4.2, and 4.3). Latent heat fluxes were dominant prior to and following the precipitation over the irrigated sites (Fig. 4.17). Through investigation of the soil moisture data, noticeable drying of the modelled soil moisture was observed at the non-irrigated sites prior to the 19 July precipitation event (Fig. 4.11). In response to the precipitation, peaks in the 5-cm SWC at both irrigated and non-irrigated sites were observed.

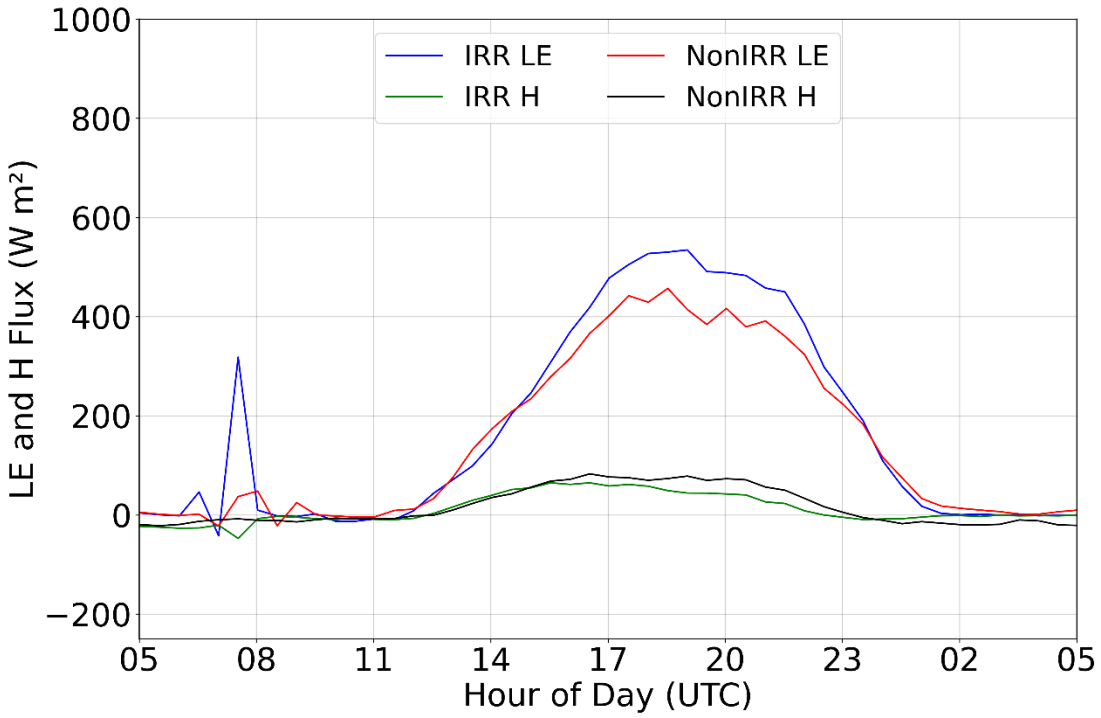

Figure 4.17: 30-minute averaged latent (LE) and sensible (H) heat flux for irrigated and non-irrigated sites on July 19th.

Once again, timing of the radiosonde launches were unable to capture the immediate impacts from the precipitation event. However, the late day soundings indicated PBL development and reduced heights as compared to soundings from IOP 1. This difference was due to access moisture and scattered cloud cover present mainly over the non-irrigated sites throughout the 19 July. For example, data from the 1900 UTC (2:00 p.m. LT) launch (Table 4.8) on 19 July indicates slightly greater PBL heights for the York Airport (irrigated) than Rogers Farm (non-irrigated). This difference was likely due to residual cloud cover limiting daytime heating over the non-irrigated sites and not associated with surface moisture, as the previous discussion indicated higher SWC in the irrigated areas. Other launches including the 1300 and 1500 UTC (8:00 a.m. and 10:00

a.m. LT, respectively) indicate lower PBL heights over the irrigated sites, which is expected.

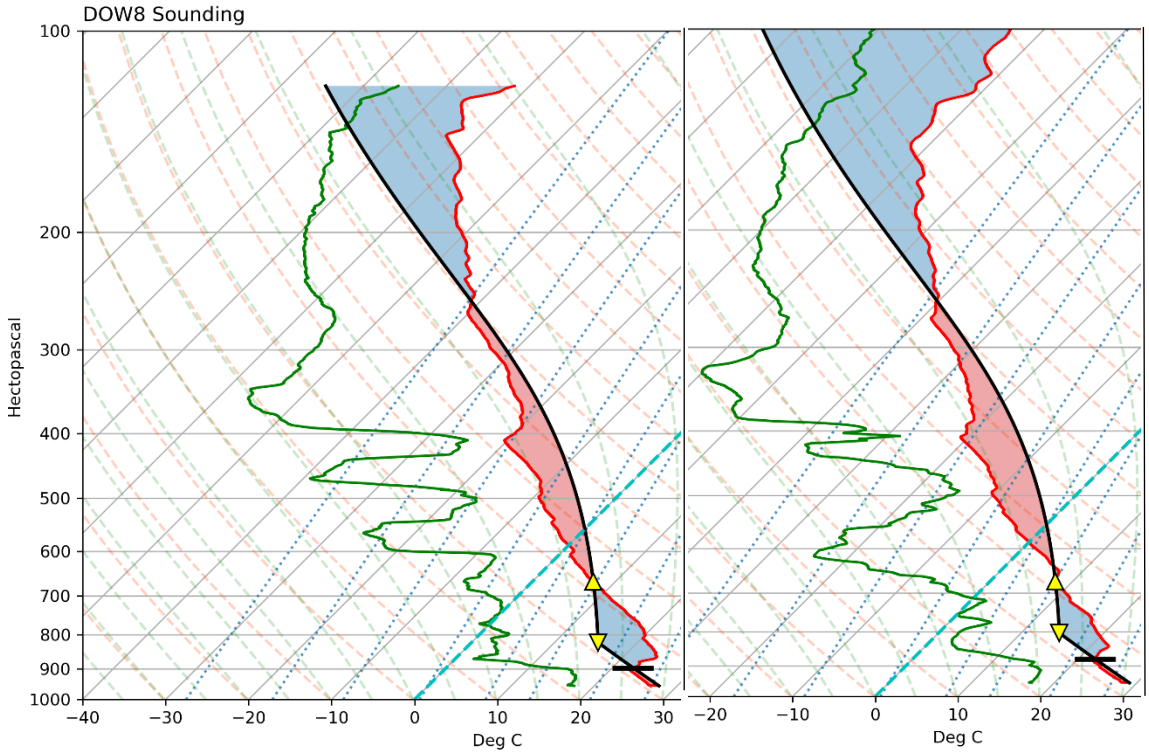

Figure 4.18: Soundings from the 1900 (left) and 2100 (right) UTC (2:00 and 4:00 p.m. LT) launches on 19 July at the DOW 8 location (exact site coordinates found in Table 3.5).

The PBL and LCL heights of 19 July (Table 4.8) indicate a similar lack in rapid increase (like 9 June) due to the precipitation occurring throughout the overnight hours. Both PBL and LCL heights for all sites on 19 July were notably lower, even when compared to 9 June, when similar weather conditions were occurring. These differences were especially noticeable during the 1900 and 2100 UTC (2:00 p.m. and 4:00 p.m. LT, respectively) launch windows, which would correspond to peaks in daytime heating and the times when the greatest influxes in PBL growth should occur. For example, all PBL heights for the 1900 and 2100 UTC launches on 9 June were above 1400 m, the lowest

of which was 1416 m at the York Airport (irrigated) at 1900 UTC (2:00 p.m. LT). For 19 July, the highest PBL was 1367 m at DOW7 (transitional) at 2100 UTC (4:00 p.m. LT). All sites experienced large reductions in PBL height due to higher latent heat flux linked to moisture from irrigation and precipitation.

Table 4.8: PBL and LCL heights (in meters above MSL) from DOW 6, 7, 8, Rogers Farm and York Airport radiosonde launches on 19 July.

		1100	1300	1500	1700	1900	2100	2300	0100
DOW 6	PBL	507		891		1161	1120	1059	
	LCL	1328	693	1066		1852	2016	1861	1437
	LFC		3498	2853		3701	3505	3175	2929
DOW 7	PBL		597	925	817	1078	1367	1507	557
	LCL		1002	1278	1472	1507	2183	2093	1685
	LFC		3727	3192	3805	3239	3422	3684	3221
DOW 8	PBL			500		1030	1208	1227	
	LCL		518	694		1791	1990	1876	1451
	LFC		3785	2216		3570	3486	3469	2855
Rogers Farm	PBL		464	827	1092	859	1066	464	
	LCL		609	852	1196	1487	1561	1589	1392
	LFC	2701	2870	2408	2267	3245	2936	2776	3209
York Airport	PBL		564	842		999			
	LCL	543	577	1066	1296	1547	1828	1582	1287
	LFC	4749	3584	2975	3081	3325	3344	2797	2639

4.7.2 22, 23, and 24 July

Conditions on 22 July were dominated by high pressure, with relatively clear skies following the dissipation of early morning fog. Seasonally normal air temperatures were observed throughout the entire period of interest. A cold front associated with a low pressure system in central Canada propagated through the GRAINEX study area during the morning hours of 23 July, bringing with it a swath of precipitation moving

from Northwest to Southeast over the irrigated cropland that dissipated as it transitioned over the non-irrigated cropland. A secondary boundary formed to the east of the non-irrigated sites along the Missouri river valley. Conditions remain overcast into the afternoon of the 23 July and sporadic showers were observed throughout the study area. High pressure returned to the area and created optimal conditions for observing L-A interactions on 24 July.

Air temperature differences over irrigated and non-irrigated regions were minimal (Fig. 4.1), but it is notable that irrigated areas were slightly cooler on 22 and 24 July when clear skies and solar radiation allowed for evapotranspiration to occur. On 23 July, when conditions were overcast over the GRAINEX study area and precipitation was occurring over irrigated sites (saturated near surface atmosphere), no additional cooling associated with evapotranspiration was observed. Observed dew point temperatures were higher for 22 and 23 July over irrigated sites. Fog and precipitation were also observed during this period and over the western portion of the study area where irrigated sites were located. Both irrigated and non-irrigated dew point temperatures were lower on 24 July with non-irrigated area midday dew point temperatures remained higher than irrigated dew point temperatures. This was likely associated with slower morning fog 'burn off' leaving residual moisture in the non-irrigated areas (Fig. 4.2). Likewise, the same pattern was observed in specific humidity (Fig. 4.3). For all three days, average latent heat fluxes over both irrigated and non-irrigated sites were higher than sensible heat fluxes (Fig. 4.19-4.21).

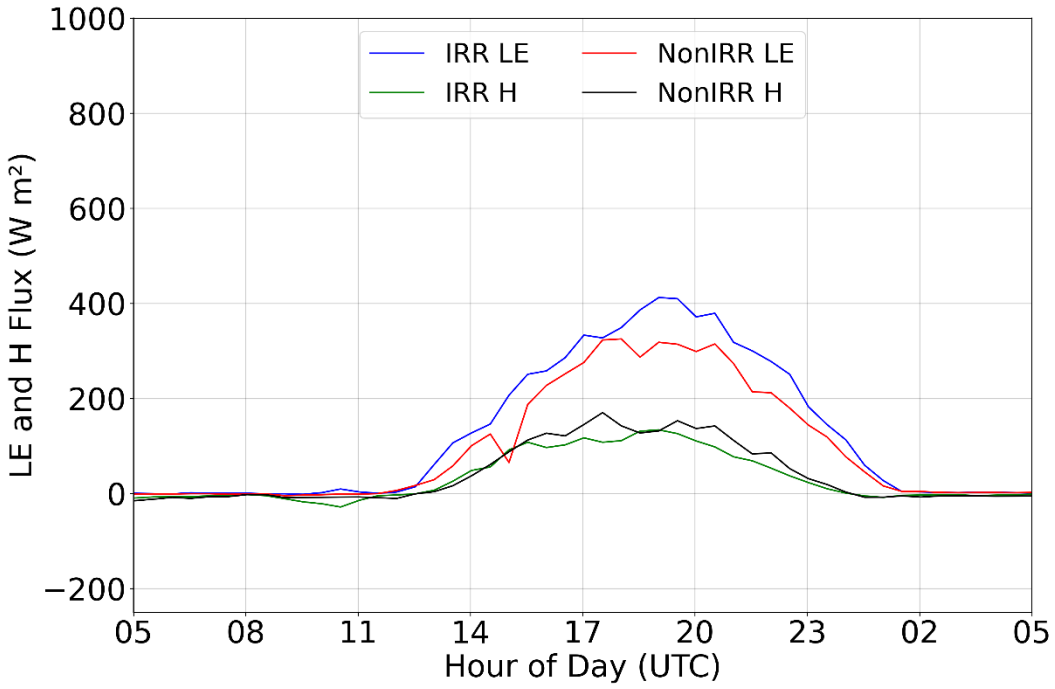

Figure 4.19: 30-minute averaged latent (LE) and sensible (H) heat flux for irrigated and non-irrigated sites on 22 July.

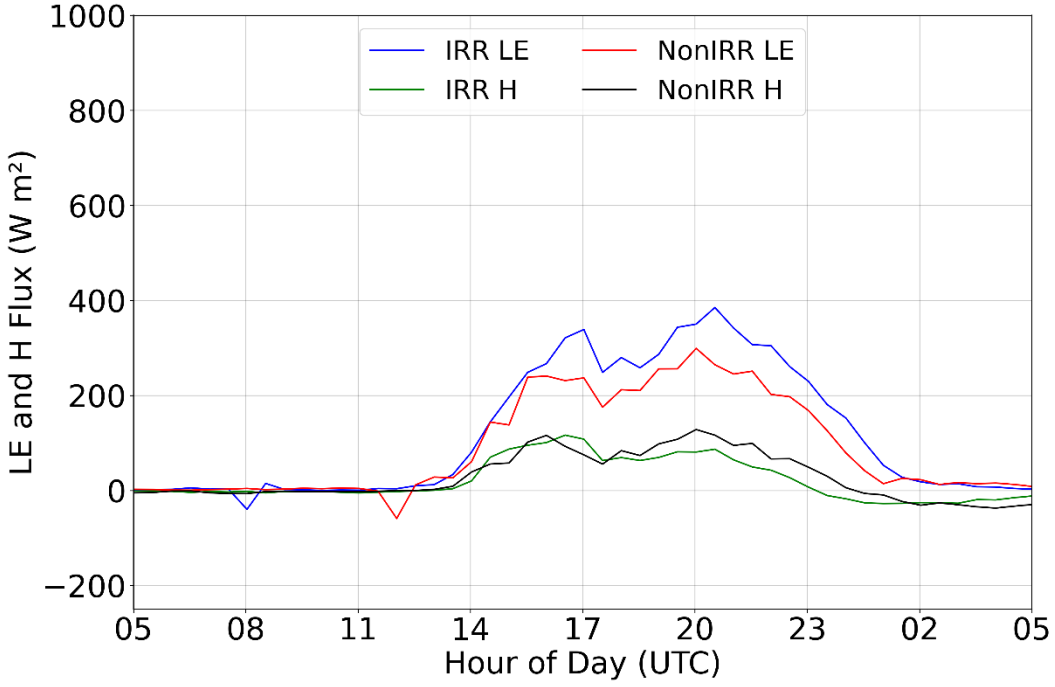

Figure 4.20: 30-minute averaged latent (LE) and sensible (H) heat flux for irrigated and non-irrigated sites on 23 July.

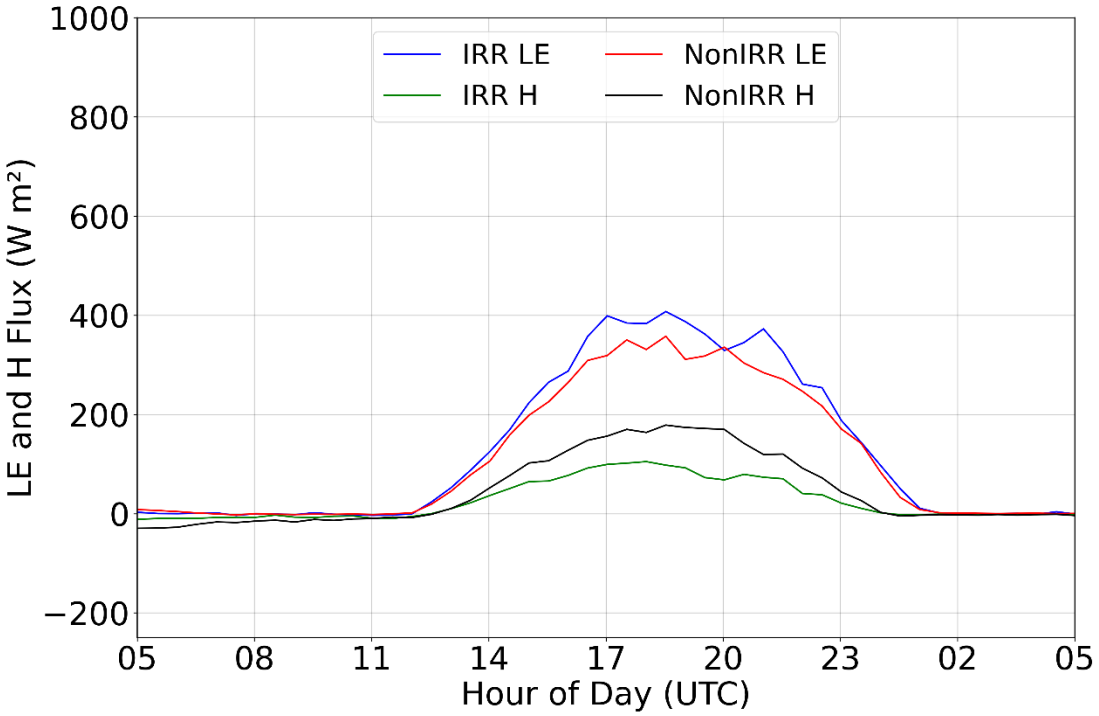

Figure 4.21: 30-minute averaged latent (LE) and sensible (H) heat flux for irrigated and non-irrigated sites on 24 July.

As expected, T_E over irrigated areas was greater for all three days with the 23 July T_E values being the largest for both irrigated and non-irrigated sites (Fig. 4.10). Since air temperatures for irrigated and non-irrigated sites remained largely unchanged for these dates, it is likely that the atmospheric moisture contributed to this increase. Precipitation amounts from the 23 July event had little or no impact on the soil moisture of higher depths in both irrigated and non-irrigated areas (Fig. 4.11). Reductions in SWC continued into the later part of IOP 2 and drying was clearly slower for the ISFS sites 1-6 due to irrigation application. DOW soundings during these dates show a well-developed PBL on 22 July (Fig. 4.22), a rapidly growing PBL in the late afternoon as the cloud cover

dissipated on 23 July (Fig. 4.23), and the return to a typical PBL under high pressure on 24 July (Fig. 4.24). The PBL and LCL heights for 22, 23, and 24 July can be found in Table 4.9, 4.10, and 4.11, respectively. A notable observation included in these tables was the consistent PBL heights for Rogers Farm and the York Airport on 23 July associated with the precipitation event, cloud cover and moist atmosphere. Once the precipitation passed and high pressure returned to the area (i.e. 24 July), a significant difference between the York Airport and Rogers Farm PBL heights became apparent (please consider 1900 UTC launch values in Table 4.11).

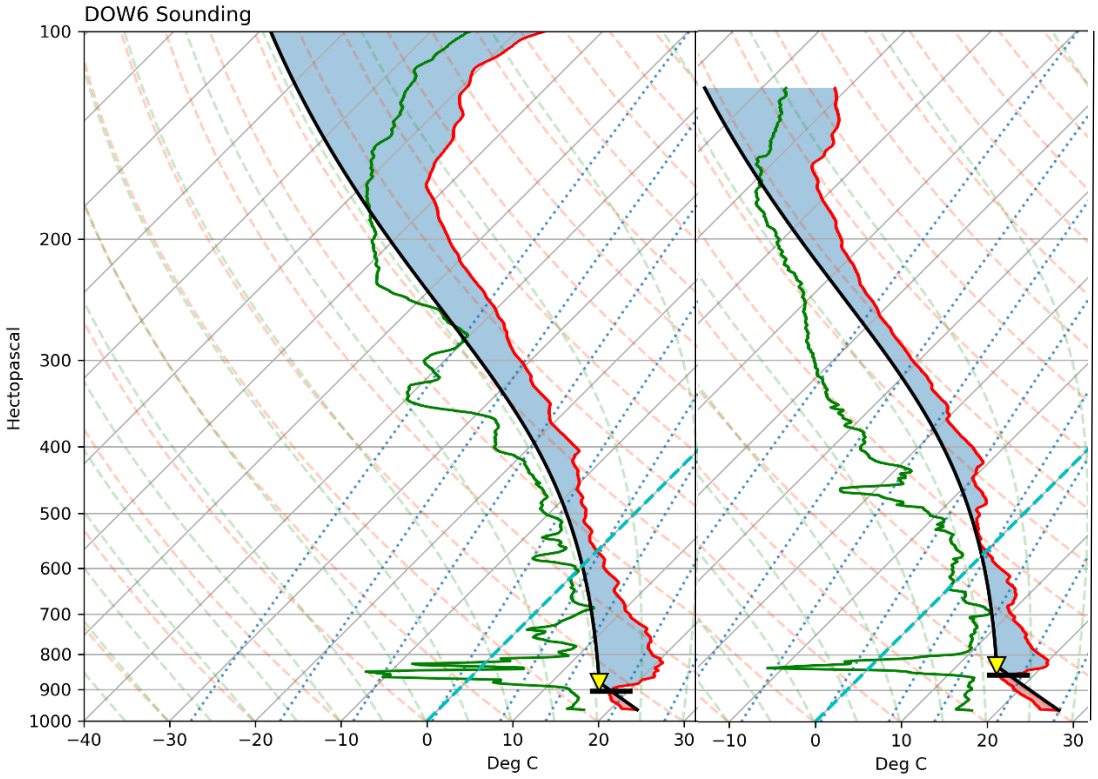

Figure 4.22: Soundings from the 1500 (left) and 1900 (right) UTC (10:00 a.m. and 2:00 p.m. LT) launches on 22 July at the DOW 6 location (exact site coordinates found in Table 3.5).

From the observations in Table 4.9, notably higher mid-afternoon PBL heights were seen for the DOW6 and Rogers Farm sites, which resided in non-irrigated and transitional regions of the study area, than DOW7, DOW8 and the York Airport. During the 2100 UTC launch (4:00 p.m. LT), PBL heights for DOW6 and Rogers Farm were 1440 m and 1414 m. These were the two highest PBL heights for this launch time. This is compared to the launch two hours prior (1900 UTC; 2:00 p.m. LT) where Rogers Farm had the lowest PBL height of the launch time (1298 m) and DOW6 had the highest of the launch time and the day (1498 m). For the late afternoon launches (2300 UTC; 6:00 p. m. LT), PBL heights over highly irrigated sites such as DOW8 and York Airport continued to rise while PBL heights at the non-irrigated site such as Rogers Farm and DOW 6 had already begun to lower for the day. It is likely that not only was PBL and LCL heights suppressed by the access moisture associated with irrigation at that time, but also the residual moisture caused a lag effect in the growth of the PBL. This is also visible in the averages plotted in Figure 4.12.

Table 4.9: PBL and LCL heights (in meters above MSL) from DOW 6, 7, 8, Rogers Farm and York Airport radiosonde launches on 22 July.

		1100	1300	1500	1700	1900	2100	2300	0100
DOW 6	PBL		567	1008	1308	1498	1440	1396	821
	LCL	630	835	1263	1589	1752	1845	1960	1421
	LFC								
DOW 7	PBL		627	1029	1355	1370		1360	1118
	LCL	626	835	1214	1585	1811		1905	1429
	LFC								4208
DOW 8	PBL				1386		1364	1412	
	LCL				1542		1935	1939	1460
	LFC								4227
Rogers Farm	PBL		417	621	1284	1298	1414	426	409
	LCL		570	989	1306	1496	1670	1454	1208
	LFC				5191	4881	5630	3960	4157
York Airport	PBL		652		1305	1346	1344	1354	
	LCL	704	854	1108	1210	1493	1644	1491	1278
	LFC				4750	5061	8594	3979	4236

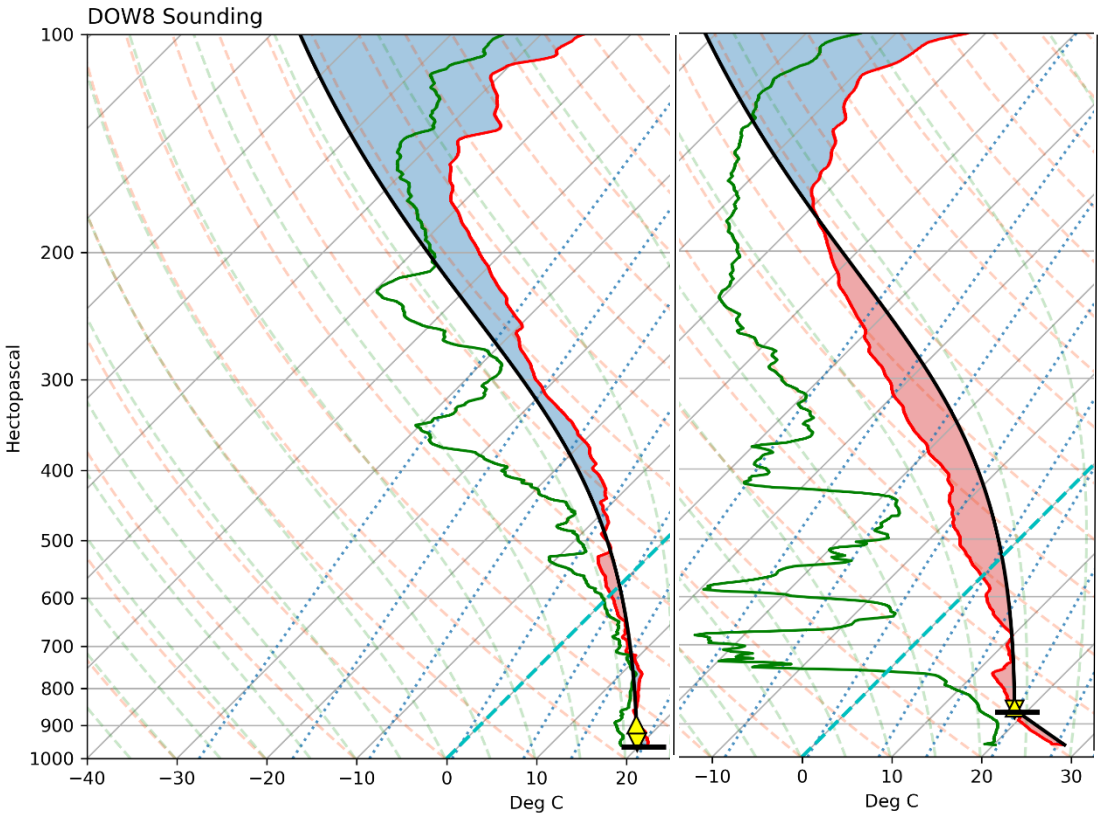

Figure 4.23: Soundings from the 1300 (left) and 2100 (right) UTC (8:00 a.m. and 4:00 p.m. LT) launches on 23 July at the DOW 8 location (exact site coordinates found in Table 3.5).

The observations in Table 4.10 show the timeline discussed previously for 23 July. The morning and early afternoon (1300 and 1500 UTC; 8:00 a.m. and 10:00 a.m. LT) values for PBL and LCL were lower than the previous day being significantly impacted by the newly introduced surface moisture. As the day progressed and the moisture at the surface had time to be used by the plants or evaporated, rapid expansion of the PBL occurred in the late afternoon (2300 and 0100 UTC; 6:00 p.m. and 8:00 p.m. LT). These values for PBL and LCL heights are comparable to the early afternoon (1900 and 2100

UTC; 2:00 p.m. and 4:00 p.m. LT) heights on 25 July, which was dominated by high pressure and longer exposure to solar radiation.

Table 4.10: PBL and LCL heights (in meters above MSL) from DOW 6, 7, 8, Rogers Farm and York Airport radiosonde launches on 23 July.

		1100	1300	1500	1700	1900	2100	2300	0100
DOW 6	PBL			797	1261		1637		564
	LCL	836		896	1250		1367		1646
	LFC	4579		1429	2801		1367		4786
DOW 7	PBL			812		1282	1221	1736	
	LCL	690		892		1248	1352	1615	1591
	LFC			3261		1335	1361	3851	4778
DOW 8	PBL				1250	1143	1396	1841	624
	LCL		620		1357	1242	1471	1605	1621
	LFC		1106		1405	1289	1515	2450	
Rogers Farm	PBL		419	781	1096	1157	1322	1528	411
	LCL	625	496	1013	1191	1281	1260	1338	1160
	LFC		6271	1416	1380	2762		1338	1340
York Airport	PBL					1097	1307		
	LCL		617	919	854		1149	1356	1074
	LFC	3003	2570	2821			1149	3753	4237

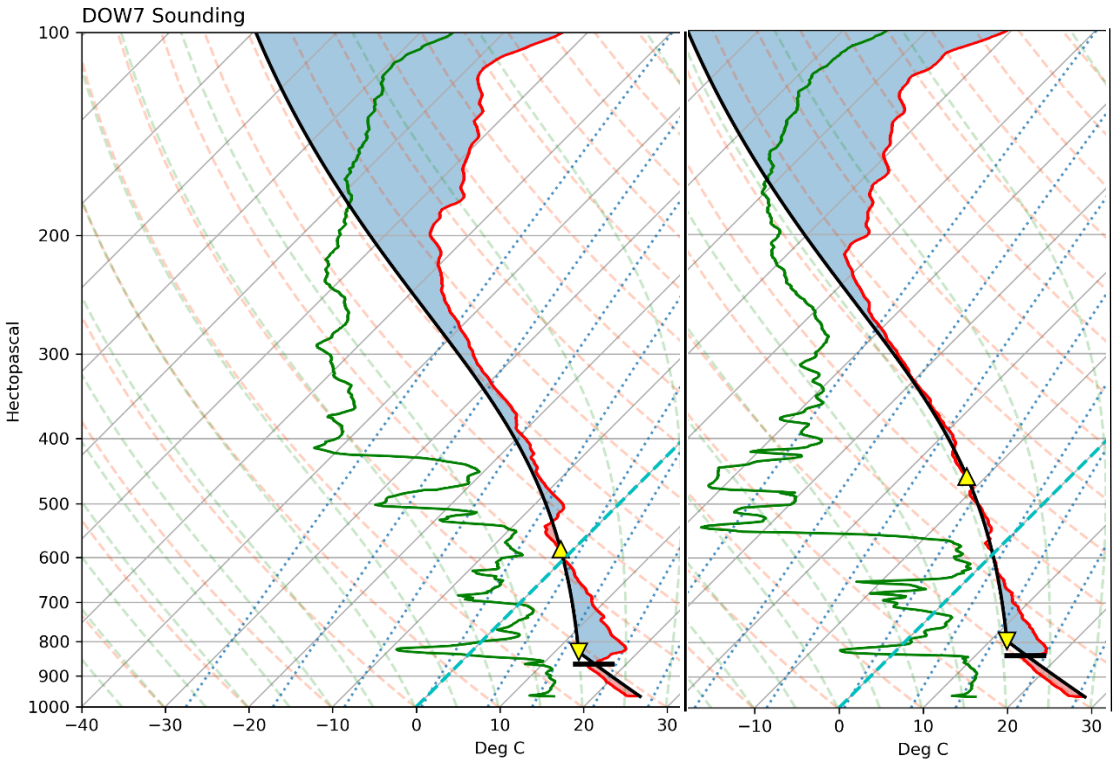

Figure 4.24: Soundings from the 1700 (left) and 2100 (right) UTC (12:00 a.m. and 4:00 p.m. LT) launches on 24 July at the DOW 7 location (exact site coordinates found in Table 3.5).

The 24 July case study during IOP 2 is most comparable to the 3 June case study during IOP 1 where high pressure was dominant. Although these dates were meteorologically similar, differences between Table 4.6 and Table 4.11 illustrate the impacts increased surface moisture, both natural and irrigated, have on the lower atmosphere. The observed PBL and LCL heights of all sites on the 24 July were much lower than those observed on 3 June and other comparable dates during IOP 1. A delay in PBL growth is also noted when comparing the 3 June observed values (Table 4.6) to the 24 July values (Table 4.11).

Table 4.11: PBL and LCL heights (in meters above MSL) from DOW 6, 7, 8, Rogers Farm and York Airport radiosonde launches on 24 July.

		1100	1300	1500	1700	1900	2100	2300	0100
DOW 6	PBL			828	1399	1640	1649	1567	603
	LCL			1451	1852	1941	2168	2166	1872
	LFC			4419	4957	4466	6144	3852	3873
DOW 7	PBL			947	1449	1658	1712	1534	1118
	LCL	822	872	1510	1799	2135	2135	2238	1894
	LFC			4443	4689	4732	6635	7241	3598
DOW 8	PBL			707		1564	1699		1325
	LCL	814		1291		1995	2180		1923
	LFC			4121		4514	4706		3710
Rogers Farm	PBL		423	591	1287	1453		1397	
	LCL		542	1065	1568	1732	1845	2096	1512
	LFC			4549	4353	4822	4851	4646	3830
York Airport	PBL				1255	1366			627
	LCL	549	669	1075	1552	1733	1525	1770	1530
	LFC			3690	4271	4090	2964	3596	2995

The data from GRAINEX suggests lower PBL and LCL heights over irrigated sites were most noticeable during IOP 2 when irrigation was more widespread. During the case study dates impacted by convective precipitation initiating early in the day (9 June, 19 July and 23 July), lower PBL heights were seen due to additional surface moisture, subsequent cloud cover and cooler temperatures associated with frontal passage(s). Lower sensible heat and a smaller differences between latent and sensible heat flux were observed over irrigated and precipitation impacted regions. Overall, these findings support previous findings addressing the connectivity of surface fluxes and planetary boundary layer development and stability linked to increased soil moisture (Eltahir and Pal, 1996; Eltahir, 1998; Findell and Eltahir, 1999; Pielke et al., 2007; Winchester et al., 2017). Lower PBL and LCL heights provide increased potential for cloud development

and convective initiation. Stratiform and other low level cloud formations (fog) were also associated with the increased surface moisture in irrigated regions.

CHAPTER 5

CONCLUSIONS

Humans rely on agriculture to provide food, fiber, and a variety of other resources. Recent shifts in temperature and precipitation patterns have been addressed with new technology and farming techniques in order to ensure crop yields match the demands from the global market. Transitioning from horse-drawn plows to large mechanical equipment (running on carbon rich fuel) has positively impacted the ability of the farmer to grow more product, but negatively impacted global CO_2 levels along with other industrial and socio-economic activities. Deforestation has caused warming in tropical regions and changes to Earth's surface albedo; reforestation efforts have reclaimed some of the land impacted by deforestation, but efforts must continue to re-establish what has been lost. Deforestation and reforestation is also known as land use land cover change (LULCC).

During the 20th Century, the Great Plains of the United States have experienced significant LULCC where humans overturned natural grassland to irrigated and non-irrigated agriculture. The LULCC not only changes albedo, it also impacts energy partitioning and various near surface meteorological variables, evolution of the planetary boundary layer, and meteorological events. These changes particularly become magnified under irrigated conditions. The repartitioning of heat and energy, as well as localized changes in air temperature and moisture throughout the Great Plains, associated with the widespread adoption of irrigation is complex and multifaceted. In

order to understand these relationships, extensive data collection effort is required and, in response, GRAINEX was conducted.

The analysis presented in this thesis explores a variety of meteorological variables including air temperature, dew point temperature, specific humidity, equivalent temperature, latent and sensible heat fluxes. In addition, the evolution of PBL and LCL heights were also analyzed. These variables are dependent on moisture (natural and artificially applied) and differences were observed between irrigated and non-irrigated areas specifically in the latter half of the growing season. Compared to IOP 1, maximum air temperatures over irrigated areas averaged ~2.75 °C lower during IOP 2, while dew point temperatures and specific humidity averaged ~0.8 °C and 0.01 higher, respectively. In addition, when we compared data from irrigated and non-irrigated sites, latent and sensible heat fluxes during IOP 1 were somewhat similar and conversely, more pronounced during IOP 2. Differences between average irrigated and non-irrigated latent and sensible heat fluxes during IOP 1 were 14.62 Wm^{-2} and 7.24 Wm^{-2}, respectively. During IOP 2, differences in average irrigated and non-irrigated latent and sensible heat fluxes were 20.46 Wm^{-2} and 17.08 Wm^{-2}, respectively. Over irrigated areas, latent heat was larger and sensible heat smaller than over non-irrigated areas. An example of this is observed in 30 minute plots of latent and sensible heat fluxes on days with strong L-A interactions like 3 June, 22 and 24 July (Fig. 4.13, 4.19 and 4.21, respectively). This difference illustrates the repartitioning of energy associated with access moisture in the cropping system.

Equivalent temperature (T_E) calculations were completed to analyze variability associated with the gradual increase in irrigation throughout the growing season. As expected, T_E values were somewhat similar at irrigated and non-irrigated sites during IOP 1, but higher over irrigated areas during IOP 2. For example, average T_E differences between irrigated and non-irrigated sites were 0.11 °C and 2.03 °C during IOP 1 and 2, respectively. Since moisture notably influences T_E, higher T_E over irrigated areas suggests a significantly higher moisture contribution as compared to the non-irrigated T_E values in IOP 2. Root zone soil moisture profiles at 25 and 50 cm depths were modelled utilizing the 5 cm soil moisture observations collected at the ISFS sites and the Wang et al. (2017) Exponential Filter Model. These data provided a detailed assessment of subsurface conditions and the magnitude and timing of the SWC responses to precipitation and irrigation applications, as well as plant uptake and soil drawdown throughout the season. The results of this model allowed for tracking of precipitation events and the visualization of a third dimension that contributed to changes in surface and lower atmospheric conditions.

To explore lower tropospheric conditions (specifically contained within the PBL), data from the radiosonde launches at the three DOW locations, Rogers Farm and the York Airport were referenced throughout this analysis. The sounding data were used to complete lifting condensation level (LCL), level of free convection (LFC), and PBL height calculations. The results suggest discernably lower LCL and PBL heights over irrigated areas during the second half of the growing season (IOP 2). A total of about 1200 (~40

per day over a 100 x 100 km area) radiosondes were launched during the two 15 day IOP windows. There was some noise in the data; however, analyses were still able to show the higher PBL heights during IOP 1, associated with larger sensible heat and increased turbulence, and lower PBL heights during IOP 2, associated with rapid plant growth, applications of irrigation due higher plant-water demand, and resultant increased latent heat flux. The conclusions of this research are further summarized in Figure 5.1.

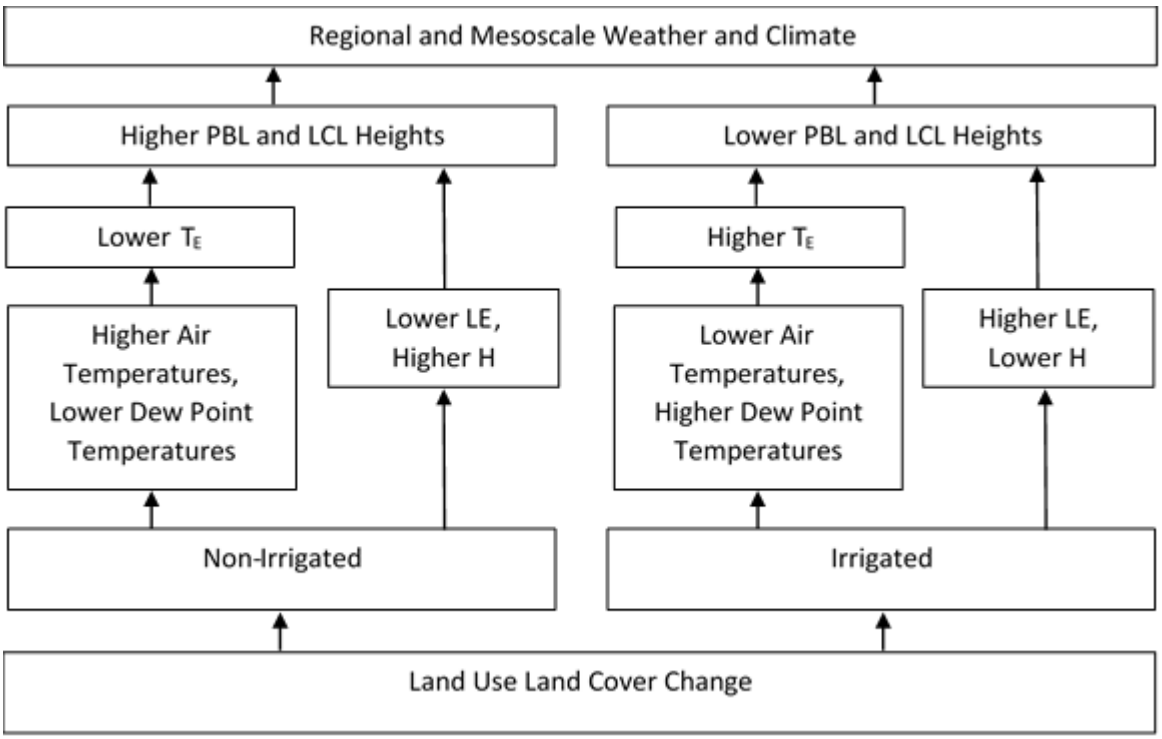

Figure 5.1. A simplified conceptual model highlighting the impacts of irrigation and non-irrigation. (Modified from Winchester et al. (2017)).

From this analysis it is clear that the data from GRAINEX can be used to explore land-atmospheric interactions and more specifically the impacts of irrigation on near surface atmospheric conditions, the PBL, and the lower troposphere. With the new

insights provided by GRAINEX, a thorough understanding of the meteorological, climatological, and LULCC impacts associated with agriculture and irrigation can be more accurately quantified and properly addressed as the global community continues the work towards establishing a healthier and sustainable planet for generations to come.

REFERENCES

Adegoke, J.O. and A. M. Carleton, 2000: Warm season land surface – climate interactions in the United States Midwest from mesoscale observations. *Linking Climate Change to Land Surface Change, 83-97*.

Adegoke, J.O., R. A. Pielke, J. Eastman, R. Mahmood, and K. G. Hubbard, 2003: Impact of irrigation of midsummer surface fluxes and temperature under dry synoptic conditions: A regional atmospheric model study of the U.S. High Plains. *Mon. Wea. Rev., **131**, 556- 564.*

Adegoke, J.O., R. A. Pielke, and A. M. Carleton, 2007: Observational and modeling studies of the impacts of agriculture-related land use change on planetary boundary layer processes in the central US. *Agric. For. Meteor.,*

Alexandru, A., and L. Sushama, 2016: Impact of land-use and land-cover changes on CRCM5 climate projections over North America for the twenty-first century. *Climate Dyn., **47**, 1197–1209.*

Alter, R.E., H. C. Douglas, J. M. Winter and E. A. B. Eltahir, 2017: 20th-century regional climate change in the central United States attributed to agricultural intensification. *Geophys. Res. Lett., **45**, 1586-1594.*

American Meteorological Society, 2012: Lifting condensation level. Glossary of Meteorology, accessed 1 November 2020, https://glossary.ametsoc.org/wiki/Lifting_condensation_level

American Meteorological Society, 2012: Level of free convection. Glossary of Meteorology, accessed 1 November 2020, https://glossary.ametsoc.org/wiki/Level_of_free_convection

Bolton, D., 1980: The computation of equivalent potential temperature. *Mon. Wea. Rev., **108**, 1046-1053.*

Bonan, G., 1999: Observational evidence for reduction of daily maximum temperature by croplands in the Midwest United States. *Climatic Change, **37**, 449-486.*

Bonan, G. B., K. W. Oleson, M. Vertenstein, S. Levis, X. Zeng, Y. Dai, R. E. Dickinson, and Z. Yang, 2002: The Land Surface Climatology of the Community Land Model Coupled to the NCAR Community Climate Model. *J. Climate, **15**, 3123–3149.*

Brovkin, V, L. Boysen, V. K. Arora, J. P. Boisier, P. Cadule, L. Chini, M. Claussen, P. Friedlingstein, V. Gayler, B. J. J. M. Van Den Hurk, G. C. Hurtt, C. D. Jones, E. Kato, N. de Noblet- Ducoudré, F. Pacifico, J. Pongratz, and M. Weiss, 2013: Effect of anthropogenic land-use and land-cover changes on climate and land carbon storage in CMIP5 Projections for the Twenty-First Century. *J. Climate, **26**, 6859-6881.*

Brown, M., and C. J. Nowotarski, 2019: The influence of lifting condensation level on low-level outflow and rotation in simulated supercell thunderstorms. *J. Atmos. Sci., **76**, 1349-1372.*

Canziani, P.O., and G. C. Benitez, 2012: Climate impacts of deforestation/land-use changes in central South America in the PRECIS regional climate model: Mean precipitation and temperature responses to present and future deforestation scenarios. *Sci. World J., **2012**, 1-20.*

Carleton, A.M., J. O. Adegoke, J. Allard, D. L. Arnold, D. J. Travis, 2001: Synoptic context of summer season land cover-convective cloud associations for the Midwest US "Corn Belt". *Geophys. Res. Lett. **28** (9), 1679-1682.*

Challinor, A.J., J. Watson, D. B. Lobell, S. M. Howden, D. R. Smith, and N. Chhetri, 2014: A meta-analysis of crop yield under climate change and adaptation. *Nat. Climate Change, **4**, 287-291.*

Chase, T.N., R. A. Pielke Sr., T. G. F. Kittel, J. S. Baron, and T. J. Stohlgren, 1999: Potential impacts on Colorado Rocky Mountain weather due to land use changes on the adjacent Great Plains. *J. Geophys. Res., **104**, 16673-16690.*

Ciais, P., T. Gasser, J. Paris, K. Caldeira, M. R. Raupach, J. Canadell, A. Patwardhan, P. Friedlingstein, S. Piao, and V. Gitz, 2013: Attributing the increase in atmospheric CO2 to emitters and absorbers, *Nature Clim. Change, **3**, 926–930.*

Craven, J.P., R. E. Jewell, and H. E. Brooks, 2002: Comparison between observed convective cloud-base heights and lifting condensation level for two different lifted parcels. *Wea. Forecasting, **17**, 885-890.*

De Silva, C.S., E. K. Weatherhead, J. W. Knox, and J. A. Rodriguez-Diaz, 2007: Predicting the impacts of climate change – a case study of paddy irrigation water requirements in Sri Lanka. *Agri. Water Manag., **93**, 19-29.*

Decker, M., M. Shaoxiu, and A. Pitman, 2017: Local land-atmosphere feedbacks limit I rrigation demand. *Envir. Res. Lett., **12**, 1-8.*

Diffenbaugh, N.S., 2009: Influence of modern land cover on the climate of the United States. *Climate Dyn., **33**, 945-958.*

Elahir, A.B., and J. S. Pal, 1996: Relationship between surface conditions and subsequent rainfall in convective storms. *J. Geophy. Res., **101**, 26,237-26,245.*

Elahir, A.B., 1998: A soil moisture-rainfall feedback mechanism. *Water Resources Res., **34**, 765-776.*

Findell, K.L., and E. A. B. Eltahir, 1999: Analysis of the pathways relating soil moisture and subsequent rainfall in Illinois. *J. Geophy. Res., **104**, 31,565-31,574.*

Findell, K.L., E. Shevliakova, P. C. D. Milly, and R. J. Stouffer, 2007: Modeled impacts of anthropogenic land cover change on climate. *J. Climate, **20**, 3621-3634.*

Forster, P., V. Ramaswamy, P. Artaxo, T. Berntsen, R. Betts, D. W. Fahey, J. Haywood, J. Lean, D. C. Lowe, G. Myhre, J. Nganga, R. Prinn, G. Raga, M. Schulz, and R. Van Dorland, 2007: *Changes in Atmospheric Constituents and in Radiative Forcing Chapter 2.* Cambridge University Press. 106 pp.

Gameda, S., B. Qian, C. A. Campbell, and R. L. Desjardins, 2007: Climatic trends associated with summerfallow in the Canadian Prairies. *Agric. For. Meteor., **142**, 170-185.*

Gitz, V., and P. Ciais, 2004: Future expansion of agriculture and pasture acts to amplify atmospheric co2 levels in response to fossil-fuel and land-use change emissions. *Clim. Change. **67**, 161-184.*

Gullison, R.E., P. C. Frumhoff, J. G. Canadell, C. B. Field, D. C. Nepstad, K. Hayhoe, R. Avissar, L. M. Curran, P. Friedlingstein, C. D. Jones, and C. Nobre, 2007: Tropical Forest and Climate Policy. *Policy Forum.* **316**, 985-986

Hahmann, A.N., and R. Dickinson, 1997: RCCM2-BATS Model over Tropical South America: Application to Tropical Deforestation. *J. Climate, **10**, 1944–1964.*

Hatfield, J.L., and J. H. Prueger, 2015: Temperature extremes: Effect on plant growth and development. *Weather Clim. Extremes, **10**, 4– 10*.

Hayes, M.J., and W. L. Decker. 1996: Using NOAA AVHRR Data to Estimate Maize Production in the United States Corn Belt. *Int. J. Remote Sens.,* **17**, 3189–3200.

Huber, D., D. Mechem, and N. Brunsell, 2014: The effects of Great Plains irrigation on the surface energy balance, regional circulation, and precipitation. *Climate, **2**, 103-128.*

Kang, S., and G. H. Bryan, 2011: A large-eddy simulation study of moist convection initiation over heterogeneous surface fluxes. *Bull. Amer. Meteor. Soc., **139**, 2901-2917.*

Kukal, M.S., and S. Irmak, 2018: Climate-driven crop yield and yield variability and climate change impacts on the U.S. Great Plains agricultural production. *Sci. Rep., **8**, 1-18.*

Lawston, P. M., J. A. Santanello Jr., B. F. Zaitchik, and M. Rodell, 2015: Impact of irrigation methods on land surface model spin up and initialization of WRF Forecasts. *J. Hydrometeor., **16**, 1135– 1154.*

LeMone, M.A., F. Chen, J. G. Alfieri, R. H. Cuenca, Y. Hagimoto, P. Blanken, D. Niyogi, S. Kang, K. Davis, and R. L. Grossman, 2007: NCAR/CU surface, soil, and vegetation observations during the International H2O Project of 2002 field campaign. *Bull. Amer. Meteor. Soc., **88**, 65-82.*

Linderholm, H.W., 2006: Growing season changes in the last century. *Agric. For. Meteor.,* **137**, 1–14.

Lobell, D.B., and C. Bonfils, 2008: The effect of irrigation on regional temperatures: a spatial and temporal analysis of trends in California. *J. Climatol., **21**, 2064-2071.*

Loveland, T. R., and R. Mahmood, 2014: A design for a sustained assessment of climate forcing and feedbacks related to land us and land cover change. *Bull. Amer. Meteor. Soc.,* **95**, 1563-1572.

Mahmood, R., and K. G. Hubbard, 2002: Anthropogenic land-use change in the North American tall grass-short grass transition and modification of near-surface hydrologic cycle. *Climate Res., **21**, 83-90.*

Mahmood, R., K. G. Hubbard, R. Leeper, and S. A. Foster, 2008: Increase in near surface atmospheric moisture content due to land use changes: Evidence from the observed dew point temperature data. *Mon. Wea. Rev., **136**, 1554-1561*.

Mahmood, R., R. A. Pielke Sr., K. G. Hubbard, D. Niyogi, G. Bonan, P. Lawrence, B. Baker, R. McNider, C. McAlpine, A. Etter, S. Gameda, B. Qian, A. Carleton, A. Beltran-Przekurat, T. Chase, A. I. Quintanar, J. O. Adegoke, S. Vezhapparambu, G. Conner, S. Asefi, E. Sertel, D. R. Legates, Y. Wu, R. Hale, O. N. Frauenfeld, A. Watts, M. Shepherd, C. Mitra, V. G. Anantharaj, S. Fall, R. Lund, A. Nordfelt, P. Blanken, J. Du, H-I., Chang, R. Leeper, U. S. Nair, S. Dobler, R. Deo, and J. Syktus, 2010: Impacts of land use land cover change on climate and future research priorities. *Bull. Amer. Meteor. Soc., **91**, 37-46.*

Mahmood, R., T. Keeling, S. A. Foster, and K. G. Hubbard, 2013: Did irrigation impact 20th century air temperature in the High Plains aquifer region? *Appl. Geogr., **38**, 11-21*

Mahmood, R., R. A. Pielke Sr., K. G. Hubbard, D. Niyogi, P. Dirmeyer, P., C. McAlpine, A. M. Carleton, R. Hale, S. Gameda, A. Beltran-Przekurat, B. Baker, R. McNider, D. R. Legates, M. Shepherd, J. Du, P. Blanken, O. W. Frauenfeld, U. S. Nair, and S. Fall, 2014: Land cover changes and their biogeophysical effects on climate. *Int. J. Climatol., **34**, 929–953.*

Mahmood, R., R. A. Pielke Sr., C. A. McAlpine, 2016: Climate-relevant land use and land cover change policies. *Bull. Amer. Meteor. Soc., **97***, 195-202.

Mahmood, R. and R. A. Pielke Sr., 2017: Land-use/cover change and climate. *Inter. Encycl. Geogr.*

McGuffie, K., A. Henderson-Sellers, H. Zhang, T. B. Durbidge, and A. J. Pitman, 1995: Global Climate Sensitivity to Tropical Deforestation. *Global Planet Change, **10**, 97–128.*

Medvigy, D., R. L. Walko, and R. Avissar, 2011: Effects of deforestation on spatiotemporal distributions of precipitation in South America. *J. Climate, **24**, 2147-2163.*

Moraes, E.C., S. H. Franchito, and V. B. Rao, 2013: Amazonian deforestation: Impact of global warming on the energy balance and climate. *J. Appl. Meteorol. Climatol., **52**, 521-530.*

Mueller, N.D., E. E. Butler, K. A. McKinnon, A. Rhines, M. Tingley, N. M. Holbrook, and P. Huybers, 2016: Cooling of US Midwest summer temperature extremes from cropland intensification. *Nat. Climate Change, **6**, 317-322.*

Mueller, N.D., A. Rhines, E. E. Butler, D. K. Ray, S. Siebert, N. M. Holbrook, and P. Huybers, 2017: Global relationships between cropland intensification and summer temperature extremes over the last 50 years. *J. Climate, **30**, 7505-7528.*

Muñoz, E., R. Mundaray, and N. Falcón, 2015: A simplified analytical method to calculate the lifting condensation level from a skew-t log-p chart. *Adv. Sci. Eng., **7**, 124-129.*

Nagendra, H., and J. Southworth, 2010: *Reforesting Landscapes: Pattern and Process.*, No. 10, Springer Link.

Oke, T. R., 1987: *Boundary Layer Climates*, Psychology Press, 435 pp.

Paruelo, J., E. Jobbágy, and O. Sala, 2001: Current Distribution of Ecosystem Functional Types in Temperate South America. *Ecosystems, **4**, 683-698.*

Pielke Sr., R.A., R. Avissar, M. Raupach, A. J. Dolman, X. Zeng, and A. S. Denning, 1998: Interactions between the atmosphere and terrestrial ecosystems: Influence on weather and climate. *Global Change Biol., **4**, 461-475.*

Pielke Sr., R.A., C. Davey, J. Morgan, 2004: Assessing "global warming" with surface heat content. *Eos Trans., **85**, 210-211*

Pielke Sr., R.A., J. O. Adegoke, A. Beltran-Przekurat, C. A. Hiemstra, J. Lin, U. S. Nair, D. Niyogi, and T. E. Nobis, 2007: An overview of regional land-use and land-cover impacts on rainfall. *Tellus: Climate Phys. Meteorol., **59**, 587-601.*

Pielke Sr., R.A., J. O. Adegoke, T. N. Chase, C. H. Marshall, T. Matsui, and D. Niyogi, 2007: A new paradigm for assessing the role of agriculture in the climate system and in climate change. *Agric. For. Meteor., **142**, 234-254.*

Pielke Sr., R.A., A. Pitman, D. Niyogi, R. Mahmood, C. McAlpine, F. Hossain, K. Klein Goldewijk, U. Nair, R. Betts, S. Fall, M. Reichstein, P. Kabat, and N. de Noblet-Ducoudré, 2011: Land use/land cover changes and climate: Modeling analysis and observational evidence. Wiley Interdisc. *Rev.: Climate Change **2**, 828-850.*

Pielke Sr., R. A., R. Mahmood, and C, McAlpine, 2016: Land's complex role in climate change. *Phys. Today, **69**, 40-46.*

Romps, D.M., 2017: Exact expression for the lifting condensation level. *J. Atmos. Sci., **74**, 3891-3900.*

Sampaio, G., C. Nobre, M. H. Costa, P. Satyamurty, B. S. Soares-Filho, and M. Cardoso, 2007: Regional climate change over eastern Amazonia caused by pasture and soybean cropland expansion. *Geophys. Res. Lett., **34**,* L17709.

Schrieber, K., R. Stull, and Q. Zhang, 1996: Distributions of surface-layer buoyancy versus lifting condensation level over a heterogeneous land surface. *J. Atmos. Sci., **53**, 1086-1107.*

Seneviratne, S.I., D. Lüthi, M. Litschi, and C. Schär, 2006: Land-atmosphere coupling and climate change in Europe. *Nature. **443**, 205-209.*

Shukla, P.R., J. Skea, R. Slade, R. van Diemen, E. Haughey, J. Malley, M. Pathak, and J. Portugal Pereira. Technical Summary, 2019. In: *Climate Change and Land: an IPCC special report on climate change, desertification, land degradation, sustainable land management, food security, and greenhouse gas fluxes in terrestrial ecosystems.*

Shukla, J., C. Nobre, and P. Sellers, 1990: Amazon Deforestation and Climate Change. *Science, **247**, 1322-1325.*

Solomon, S., G. K. Plattner, R. Knutti, and P. Friedlingstein, 2009: Irreversible climate change due to carbon dioxide emissions. *PNAS, **106**, 1704-1709*

Stern, N., 2006: *The Economics of Climate Change: the Stern Review.* Cambridge University Press. 576 pp.

Strandberg, G., and E. Kjellström, 2019: Climate impacts from afforestation and deforestation in Europe. *Earth Interact, **23***, 1-27.

Strandberg, G., E. Kjellström, A. Poska, S. Wagner, M. J. Gaillard, A. K. Trondman, A. Mauri, B. A. S. Davis, J. O. Kaplan, H. J. B. Birks, A. E. B, R. Fyfe, T. Giesecke, L. Kalnina, M. Kangur, W. O. van der Knaap, U. Kokfelt, P. Kuneš, M. Latalowa, L. Marquer, F. Mazier, A. B. Nielsen, B. Smith, H. Seppä, and S. Sugita, 2014: Regional climate model simulations for Europe at 6 and 0.2 k BP: Sensitivity to changes in anthropogenic deforestation. *Climate Past, **10**, 661–680.*

Szilagyi, J., and T. E. Franz, 2020: Anthropogenic hydrometeorological changes at a regional scale: observed irrigation–precipitation feedback (1979–2015) in Nebraska, USA. *Sustain. Water Resour. Manag., **6**, 1.*

Unidata, 2020a: MetPy: Upper air sounding tutorial. Github, accessed 14 July 2020, https://unidata.github.io/MetPy/latest/tutorials/upperair_soundings.html

Unidata, 2020b: MetPy: calc. Github accessed 14 July 2020, https://unidata.github.io/MetPy/latest/api/generated/metpy.calc.html#soundings

van Meijl, H., P. Havlik, H. Lotze-Campen, E. Stehfest, P. Witzke, I. P. Domínguez, B. L. Bodirsky, M. van Dijk, J. Doelman, and T. Fellmann, 2018: Comparing impacts of climate change and mitigation on global agriculture by 2050. *Enviro. Res. Lett., **13**, 1-20.*

Wang, T., T. E. Franz, J. You, M. D. Shulski, and C. Ray, 2017: Evaluating controls of soil properties and climatic conditions on the use of an exponential filter for converting near surface to root zone soil moisture contents. *J. Hydrology, **548**, 683-696.*

Wetzel, P. J., S. Argentini, and A. Boone, 1996: Role of land surface in controlling daytime cloud amount: Two case studies in the GCIP-SW area, *J. Geophys. Res*., ***101***, 7359–7370.

Winchester, J., R. Mahmood, W. Rodgers, F. Hossain, E. Rappin, J. Durkee, and T. Chronis, 2017: A model-based assessment of potential impacts of man-made reservoirs on precipitation. *Earth Interact., **21**, 1-31.*

Wreford, A., D. Moran, and N. Adger, 2010: *Climate change and agriculture: Impacts, adaptation and mitigation.* OECD Publishing, 135 pp.

Younger, K., R. Mahmood, G. Goodrich, R. A. Pielke Sr., and J. Durkee, 2018: Mesoscale surface equivalent temperature (Te) for East Central USA. *Theor. Appl. Climatol. **136**, 65-75.*

Zeng, N., R. E. Dickinson, and X. Zeng, 1996: Climatic Impacts of Amazon Deforestation – A Mechanistic Model Study. *J. Climate, **9**, 859–883*.

Zhang, H., A. Henderson-Sellers, and K. McGuffie, 1996: Impacts of Tropical Deforestation I: Process Analysis of Local Climatic Change. J. Climate, **9**, 1497–1517.

APPENDIX

A)

B)

C)

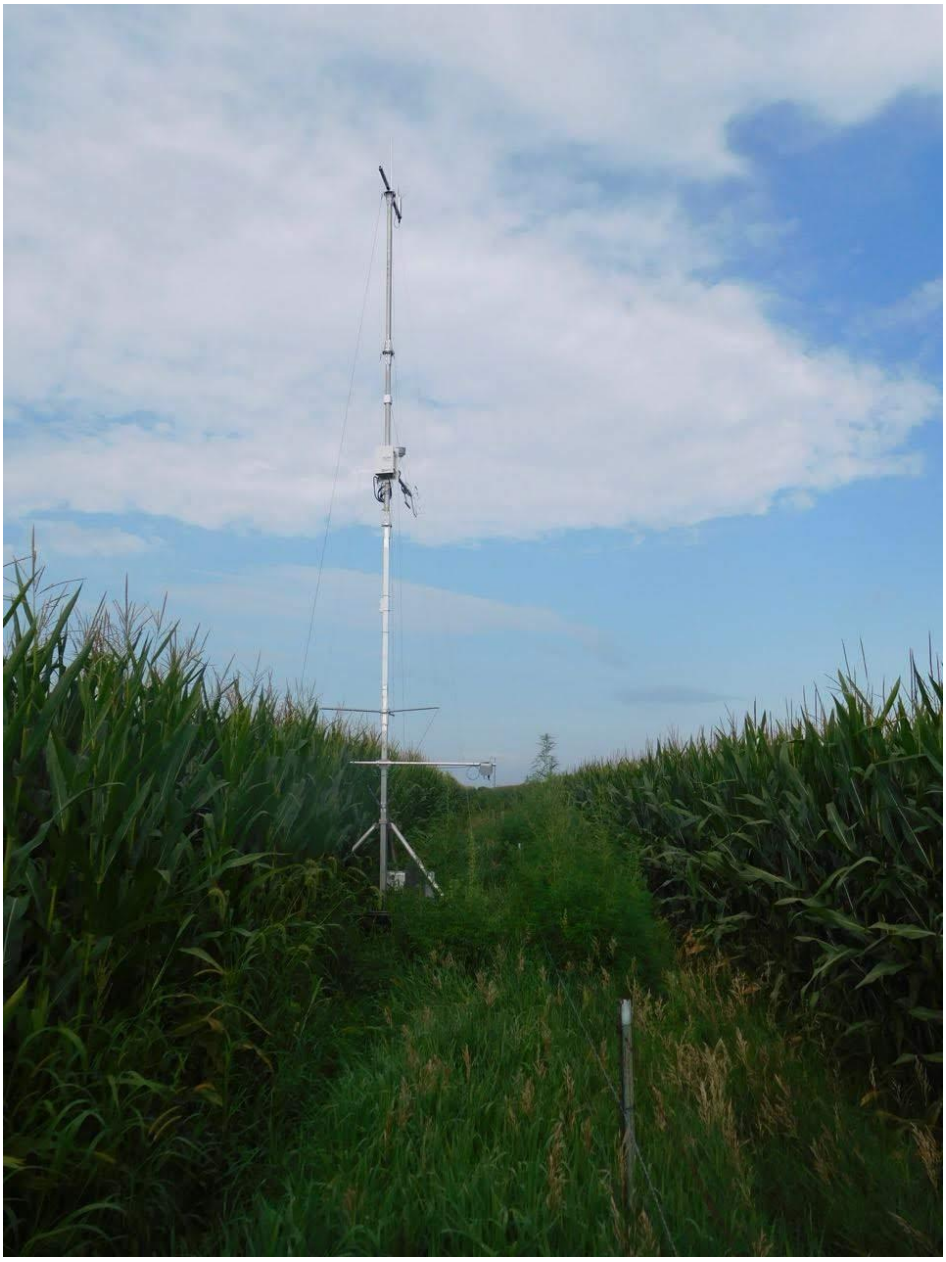

D)

E)

F)

G)

H)

Figure A.1a-h. a) An irrigated ISFS tower (site #1 in Fig. 1) at the beginning of the IPO2 with a center pivot irrigation system in the background; b) a tripod with net radiometer during IOP1, c) same ISFS tower during IOP2 (middle of the growing season; d) net radiometer during IOP2 (middle of the growing season); e) ISS Wind profiler; f) a launched radiosonde balloon; g) one of the three Doppler on Wheels (DOW) and h) an EMESH station next to an irrigated field.

Table 1.A. Locations of EMESH sites deployed during GRAINEX.

Site	Latitude	Longitude	Site	Latitude	Longitude	Site	Latitude	Longitude
0	40.9884	-97.4461	29	40.6692	-97.1115	57	40.6622	-97.4842
2	40.6399	-96.2634	30	41.3219	-97.1243	60	40.5103	-96.7102
5	40.9264	-96.2457	31	41.3378	-97.2742	64	40.3452	-96.4166
6	40.5231	-95.8769	32	40.4805	-97.5579	65	40.5504	-97.0499
7	40.8448	-96.3032	33	40.6365	-97.5789	66	40.5961	-96.8869
8	40.6853	-96.0830	34	40.3974	-97.5016	67	40.7381	-97.5983
9	40.7557	-97.2872	35	40.4806	-96.9067	68	40.6429	-97.2838
10	40.5826	-96.3956	37	40.4670	-96.8565	69	40.4870	-97.4636
11	40.5355	-96.1313	38	41.0736	-96.9372	70	40.5094	-97.0833
12	40.5226	-96.8372	39	41.1756	-96.4006	71	40.6526	-96.9163
13	40.9479	-97.1238	40	41.1772	-96.5436	80	40.4689	-96.6111
14	41.0031	-97.2256	41	41.1033	-96.5164	81	40.4377	-97.3261
15	40.4514	-96.7608	42	41.3869	-96.8461	82	40.4529	-96.5239
16	40.8933	-97.1061	43	41.3799	-96.6213	83	40.4800	-97.0375
17	41.0073	-97.6014	44	41.1256	-97.2921	84	40.4745	-96.9695
18	40.6087	-96.6710	46	41.2527	-97.0042	85	40.6399	-96.9902
19	40.7198	-97.3526	47	41.2480	-96.4542	86	40.4506	-96.8839
20	40.5659	-96.9788	48	41.3073	-96.6536	87	40.3804	-96.7315
21	40.7704	-97.0754	49	41.3039	-96.9097	89	40.4844	-96.3497
22	40.4888	-96.2423	50	41.1991	-97.1568	94	40.7852	-97.8028
23	40.8810	-97.7514	51	41.1849	-97.3682	95	41.1627	-97.5976
24	41.1044	-97.0153	52	40.5379	-97.3070	96	41.1675	-97.5502
25	40.6202	-97.1786	53	41.1078	-96.7741	97	40.8704	-97.5595
26	40.8876	-97.3523	54	40.9450	-97.5980	98	41.0782	-97.6018
27	41.3875	-97.0736	55	40.8239	-96.3350	99	40.9135	-96.8714

Table A.2: Daytime (11 UTC to 1 UTC) average, minimum and maximum air temperature (T) and dew point temperature (T_d) for irrigated and non-irrigated sites during IOP 1. Values correspond to Figure 4.1.

IOP #1 – Irrigated vs. Non-Irrigated Full Day Average Air Temperature (T) and Dew point Temperature (T_d)			
	Date	T (°C)	T_d (°C)
Irrigated	5/30/2018	24.03 (15.34 to 29.25)	17.37 (14.35 to 18.83)
	5/31/2018	27.31 (16.28 to 33.03)	18.02 (14.55 to 19.61)
	6/1/2018	29.39 (16.75 to 34.58)	19.57 (15.20 to 21.43)
	6/2/2018	21.64 (15.39 to 24.94)	13.90 (11.61 to 17.37)
	6/3/2018	23.17 (11.46 to 27.42)	11.94 (8.79 to 14.26)
	6/4/2018	21.83 (16.51 to 27.08)	14.16 (9.94 to 17.07)
	6/5/2018	27.42 (14.13 to 33.42)	18.77 (13.01 to 21.26)
	6/6/2018	29.27 (18.25 to 35.12)	21.50 (17.44 to 23.38)
	6/7/2018	24.72 (19.42 to 28.80)	17.35 (14.23 to 19.49)
	6/8/2018	27.65 (16.67 to 32.43)	19.68 (15.97 to 21.10)
	6/9/2018	27.25 (17.73 to 33.01)	20.56 (15.56 to 23.60)
	6/10/2018	29.35 (21.01 to 36.46)	22.00 (19.29 to 25.37)
	6/11/2018	28.16 (23.42 to 34.88)	21.98 (18.59 to 23.99)
	6/12/2018	25.16 (16.52 to 30.48)	18.79 (16.03 to 21.09)
	6/13/2018	23.37 (11.99 to 27.52)	15.21 (10.60 to 17.24)
	Full IOP	25.98 (11.46 to 36.46)	18.05 (8.79 to 25.37)
	Avg. Min/Max	16.72 / 31.23	14.34 / 20.34
Non-Irrigated	5/30/2018	24.41 (15.88 to 30.19)	17.54 (14.77 to 19.16)
	5/31/2018	28.53 (18.04 to 33.60)	18.52 (14.47 to 20.49)
	6/1/2018	30.12 (18.30 to 35.64)	19.54 (16.01 to 21.71)
	6/2/2018	22.07 (14.97 to 25.79)	14.86 (11.18 to 18.67)
	6/3/2018	23.59 (12.43 to 28.12)	12.02 (8.00 to 14.22)
	6/4/2018	21.74 (14.86 to 26.04)	13.00 (8.96 to 15.71)
	6/5/2018	27.41 (15.14 to 33.34)	18.88 (13.20 to 21.08)
	6/6/2018	29.80 (20.28 to 34.84)	21.61 (18.91 to 23.68)
	6/7/2018	24.34 (18.99 to 28.42)	17.74 (14.15 to 20.31)
	6/8/2018	27.97 (18.56 to 32.57)	20.53 (17.37 to 22.76)
	6/9/2018	28.05 (18.90 to 32.95)	20.13 (14.67 to 24.85)
	6/10/2018	27.89 (20.86 to 32.58)	21.49 (18.76 to 23.91)
	6/11/2018	27.94 (18.65 to 34.71)	20.94 (15.64 to 25.38)
	6/12/2018	24.86 (17.82 to 28.91)	20.45 (15.87 to 22.71)
	6/13/2018	23.22 (14.97 to 26.40)	14.91 (11.95 to 17.14)
	Full IOP	26.13 (12.43 to 35.64)	18.14 (8.00 to 25.38)
	Avg. Min/Max	17.24 / 30.94	14.26 / 20.79

Table A.3: Daytime (11 UTC to 1 UTC) average, minimum and maximum air temperature (T) and dew point temperature (T_d) for irrigated and non-irrigated sites during IOP 2. Values correspond to Figure 4.2.

IOP #1 – Irrigated vs. Non-Irrigated Full Day Average Air Temperature (T) and Dew point Temperature (T_d)			
	Date	T (°C)	T_d (°C)
Irrigated	7/16/2018	25.49 (18.02 to 31.15)	22.33 (17.72 to 25.85)
	7/17/2018	22.38 (19.03 to 26.69)	21.19 (17.75 to 23.12)
	7/18/2018	24.57 (18.70 to 28.58)	21.91 (18.89 to 24.30)
	7/19/2018	26.69 (18.09 to 31.70)	22.15 (18.12 to 25.01)
	7/20/2018	23.86 (15.69 to 28.79)	19.98 (15.46 to 23.36)
	7/21/2018	25.11 (15.61 to 29.43)	20.52 (15.72 to 23.50)
	7/22/2018	24.52 (17.16 to 29.33)	20.22 (16.97 to 22.42)
	7/23/2018	25.08 (18.75 to 29.87)	21.59 (18.21 to 24.33)
	7/24/2018	23.90 (11.95 to 29.25)	18.47 (11.91 to 22.26)
	7/25/2018	21.98 (15.02 to 27.29)	19.57 (15.08 to 23.09)
	7/26/2018	23.02 (14.10 to 27.93)	18.16 (14.14 to 20.90)
	7/27/2018	21.32 (13.13 to 26.29)	17.41 (13.30 to 20.12)
	7/28/2018	22.26 (15.80 to 27.25)	18.63 (15.80 to 21.15)
	7/29/2018	21.80 (16.31 to 26.79)	18.23 (16.44 to 20.66)
	7/30/2018	20.71 (14.98 to 26.92)	17.46 (13.49 to 20.00)
	Full IOP	23.51 (11.95 to 31.70)	19.85 (11.91 to 25.85)
	Avg. Min/Max	16.16 / 28.49	15.93 / 22.67
Non-Irrigated	7/16/2018	26.64 (19.63 to 31.46)	22.61 (19.02 to 24.47)
	7/17/2018	21.35 (18.39 to 25.23)	19.97 (18.08 to 21.91)
	7/18/2018	24.36 (17.86 to 37.50)	21.19 (18.22 to 25.40)
	7/19/2018	27.56 (19.79 to 31.99)	22.11 (18.71 to 24.58)
	7/20/2018	24.63 (16.72 to 28.73)	18.98 (13.74 to 21.98)
	7/21/2018	25.44 (17.49 to 29.46)	19.51 (17.19 to 21.48)
	7/22/2018	24.75 (16.37 to 29.40)	19.01 (16.65 to 20.73)
	7/23/2018	25.21 (19.58 to 29.45)	20.54 (17.80 to 22.80)
	7/24/2018	24.72 (14.19 to 29.61)	17.61 (13.80 to 19.86)
	7/25/2018	22.90 (14.61 to 28.65)	18.57 (14.61 to 21.82)
	7/26/2018	23.82 (15.52 to 28.70)	17.31 (14.71 to 19.80)
	7/27/2018	22.22 (12.28 to 27.65)	15.82 (12.20 to 19.04)
	7/28/2018	21.74 (16.44 to 25.58)	18.13 (16.46 to 20.03)
	7/29/2018	21.97 (15.71 to 26.93)	17.87 (15.65 to 19.79)
	7/30/2018	21.63 (0.00 to 26.06)	16.93 (0.00 to 19.81)
	Full IOP	23.93 (0.00 to 37.50)	19.08 (0.00 to 25.40)
	Avg. Min/Max	15.64 / 29.09	15.12 / 21.57

Table A.4: Daytime (11 UTC to 1 UTC) average, minimum and maximum specific humidity (q) using calculation method 1 (Equation 4) and 2 (Equation 5) for irrigated and non-irrigated sites during IOP 1. Values correspond to Figure 4.3. Note: specific humidity is unitless.

IOP #1 – Irrigated vs. Non-Irrigated Full Day Average Specific Humidity (q)			
	Date	Method #1	Method #2
Irrigated	5/30/2018	0.013 (0.011 to 0.014)	0.013 (0.011 to 0.014)
	5/31/2018	0.012 (0.009 to 0.015)	0.014 (0.011 to 0.015)
	6/1/2018	0.013 (0.010 to 0.016)	0.015 (0.011 to 0.017)
	6/2/2018	0.010 (0.008 to 0.013)	0.010 (0.009 to 0.013)
	6/3/2018	0.008 (0.006 to 0.009)	0.009 (0.007 to 0.010)
	6/4/2018	0.011 (0.008 to 0.013)	0.011 (0.008 to 0.013)
	6/5/2018	0.013 (0.010 to 0.016)	0.014 (0.010 to 0.017)
	6/6/2018	0.016 (0.012 to 0.019)	0.017 (0.013 to 0.019)
	6/7/2018	0.013 (0.011 to 0.015)	0.013 (0.011 to 0.015)
	6/8/2018	0.014 (0.012 to 0.016)	0.015 (0.012 to 0.016)
	6/9/2018	0.016 (0.012 to 0.019)	0.016 (0.012 to 0.019)
	6/10/2018	0.017 (0.013 to 0.021)	0.018 (0.015 to 0.021)
	6/11/2018	0.017 (0.015 to 0.019)	0.017 (0.014 to 0.020)
	6/12/2018	0.014 (0.011 to 0.017)	0.014 (0.012 to 0.016)
	6/13/2018	0.011 (0.009 to 0.013)	0.011 (0.008 to 0.013)
	Full IOP	0.013 (0.006 to 0.021)	0.014 (0.007 to 0.021)
Non-Irrigated	5/30/2018	0.013 (0.011 to 0.015)	0.013 (0.011 to 0.014)
	5/31/2018	0.012 (0.009 to 0.015)	0.014 (0.011 to 0.016)
	6/1/2018	0.013 (0.009 to 0.016)	0.015 (0.012 to 0.017)
	6/2/2018	0.011 (0.000 to 0.014)	0.011 (0.000 to 0.014)
	6/3/2018	0.008 (0.000 to 0.009)	0.009 (0.000 to 0.010)
	6/4/2018	0.010 (0.007 to 0.012)	0.010 (0.007 to 0.012)
	6/5/2018	0.013 (0.010 to 0.015)	0.014 (0.010 to 0.016)
	6/6/2018	0.016 (0.013 to 0.019)	0.017 (0.014 to 0.019)
	6/7/2018	0.013 (0.011 to 0.016)	0.013 (0.010 to 0.015)
	6/8/2018	0.015 (0.013 to 0.018)	0.016 (0.013 to 0.018)
	6/9/2018	0.015 (0.010 to 0.021)	0.016 (0.011 to 0.020)
	6/10/2018	0.017 (0.015 to 0.019)	0.017 (0.014 to 0.019)
	6/11/2018	0.016 (0.012 to 0.020)	0.016 (0.012 to 0.021)
	6/12/2018	0.016 (0.012 to 0.018)	0.016 (0.012 to 0.018)
	6/13/2018	0.011 (0.008 to 0.013)	0.011 (0.009 to 0.013)
	Full IOP	0.013 (0.000 to 0.021)	0.014 (0.000 to 0.021)

Table A.5: Daytime (11 UTC to 1 UTC) average, minimum and maximum specific humidity (q) using calculation method 1 (Equation 4) and 2 (Equation 5) for irrigated and non-irrigated sites during IOP 2. Values correspond to Figure 4.3. Note: specific humidity is unitless.

IOP #2 – Irrigated vs. Non-Irrigated Full Day Average Specific Humidity (q)			
	Date	Method #1	Method #2
Irrigated	7/16/2018	0.018 (0.013 to 0.022)	0.018 (0.013 to 0.022)
	7/17/2018	0.017 (0.014 to 0.019)	0.016 (0.013 to 0.019)
	7/18/2018	0.018 (0.014 to 0.020)	0.017 (0.014 to 0.020)
	7/19/2018	0.018 (0.014 to 0.021)	0.018 (0.014 to 0.021)
	7/20/2018	0.016 (0.011 to 0.019)	0.015 (0.011 to 0.019)
	7/21/2018	0.016 (0.012 to 0.019)	0.016 (0.012 to 0.019)
	7/22/2018	0.016 (0.013 to 0.018)	0.016 (0.013 to 0.018)
	7/23/2018	0.017 (0.014 to 0.020)	0.017 (0.014 to 0.020)
	7/24/2018	0.014 (0.009 to 0.018)	0.014 (0.009 to 0.017)
	7/25/2018	0.015 (0.011 to 0.019)	0.015 (0.011 to 0.019)
	7/26/2018	0.014 (0.010 to 0.022)	0.014 (0.010 to 0.022)
	7/27/2018	0.013 (0.010 to 0.016)	0.013 (0.010 to 0.015)
	7/28/2018	0.014 (0.012 to 0.017)	0.014 (0.012 to 0.016)
	7/29/2018	0.014 (0.012 to 0.016)	0.014 (0.012 to 0.016)
	7/30/2018	0.013 (0.010 to 0.016)	0.013 (0.010 to 0.015)
	Full IOP	0.015 (0.009 to 0.022)	0.015 (0.009 to 0.022)
Non-Irrigated	7/16/2018	0.018 (0.015 to 0.020)	0.018 (0.014 to 0.020)
	7/17/2018	0.015 (0.014 to 0.017)	0.015 (0.014 to 0.017)
	7/18/2018	0.017 (0.013 to 0.019)	0.016 (0.013 to 0.021)
	7/19/2018	0.017 (0.012 to 0.020)	0.017 (0.014 to 0.020)
	7/20/2018	0.015 (0.011 to 0.018)	0.014 (0.010 to 0.017)
	7/21/2018	0.015 (0.013 to 0.017)	0.015 (0.013 to 0.016)
	7/22/2018	0.014 (0.012 to 0.016)	0.014 (0.012 to 0.016)
	7/23/2018	0.016 (0.013 to 0.018)	0.016 (0.013 to 0.018)
	7/24/2018	0.013 (0.010 to 0.015)	0.013 (0.010 to 0.015)
	7/25/2018	0.014 (0.011 to 0.017)	0.014 (0.011 to 0.017)
	7/26/2018	0.013 (0.010 to 0.015)	0.013 (0.011 to 0.015)
	7/27/2018	0.012 (0.009 to 0.014)	0.012 (0.009 to 0.014)
	7/28/2018	0.014 (0.012 to 0.015)	0.013 (0.012 to 0.015)
	7/29/2018	0.013 (0.011 to 0.015)	0.013 (0.011 to 0.015)
	7/30/2018	0.013 (0.000 to 0.015)	0.012 (0.000 to 0.015)
	Full IOP	0.014 (0.000 to 0.020)	0.014 (0.000 to 0.021)

Table A.6. Average PBL Heights for DOW 6, 7, 8, Rogers Farm and the York Airport during IOP 1. Values correspond to Figure 4.12.

	DOW 6	DOW 7	DOW 8	DOW Average	Rogers Farm	York Airport
1100 UTC		597				553.5
1300 UTC	580.67	608.33	609.5	590.7	513	638.36
1500 UTC	872.43	918.36	891.6	885.55	740.1	936.73
1700 UTC	1386.73	1441.08	1497.58	1389.94	1302.92	1349.08
1900 UTC	1747.08	1738.27	1737.78	1738.8	1580.5	1331.2
2100 UTC	1772.18	1858.7	2177.38	1947.27	1414.44	1474.09
2300 UTC	1712.64	1754.86	1790.63	1725.32	1314.43	1827
0100 UTC	558.5	933.13	1159.8	966.44		904.56

Table A.7. Average PBL Heights for DOW 6, 7, 8, Rogers Farm and the York Airport during IOP 1. Values correspond to Figure 4.12.

	DOW 6	DOW 7	DOW 8	DOW Average	Rogers Farm	York Airport
1100 UTC	507	591	546	549	417	
1300 UTC	582.17	617.86	546	586.13	432.55	636.43
1500 UTC	804.55	840.22	684	765.68	720	901.25
1700 UTC	1209.43	1212.91	1209	1119.83	1043.93	1143.64
1900 UTC	1289.55	1467.9	1317.58	1347.71	1183.64	1170.67
2100 UTC	1290.23	1239.89	1365.2	1344.3	1207	1132
2300 UTC	1321.73	1402.62	1248.36	1269.67	980.62	1210.33
0100 UTC	742.25	855	726.11	814.33	502	640.5